

論文 / 著書情報
Article / Book Information

題目(和文)	スピンスプレー反応制御と90 以下の後処理により作製した機能性酸化物膜のフレキシブルセンサ応用
Title(English)	Flexible Sensors Utilizing Functionalized Oxide Films Fabricated by Controlling Spin-spray Reactions and Post-treatment below 90
著者(和文)	新田亮介
Author(English)	Ryosuke Nitta
出典(和文)	学位:博士(工学), 学位授与機関:東京工業大学, 報告番号:甲第11784号, 授与年月日:2022年3月26日, 学位の種別:課程博士, 審査員:松下 伸広,矢野 哲司,中島 章,生駒 俊之,宮内 雅浩
Citation(English)	Degree:Doctor (Engineering), Conferring organization: Tokyo Institute of Technology, Report number:甲第11784号, Conferred date:2022/3/26, Degree Type:Course doctor, Examiner:,,,,,
学位種別(和文)	博士論文
Type(English)	Doctoral Thesis

**Flexible Sensors Utilizing
Functionalized Oxide Films Fabricated by
Controlling Spin-spray Reactions and
Post-treatment below 90°C**

Thesis Submitted to
Tokyo Institute of Technology

By
Ryosuke Nitta

*In Partial Fulfillment of the Requirements
for the Degree of*
Doctor of Engineering

Main Supervisor: Prof. Nobuhiro Matsushita

**Department of Materials Science and Engineering
Tokyo Institute of Technology
Japan
March 2022**

Contents

Chapter 1	General Introduction	1
1.1	Background of This Thesis	1
1.2	Solution Processes for Fabrication Metal Oxide Films.....	2
1.2.1	Spin-spray Method	3
1.2.2	Mist Spin Spray Method	4
1.2.3	Spin Spray Reaction.....	6
1.3	Zinc Oxide (ZnO)	7
1.3.1	Properties of ZnO	7
1.3.2	Potential Applications of ZnO	8
1.4	Cuprous Oxide (Cu ₂ O).....	8
1.4.1	Properties of Cu ₂ O.....	8
1.4.2	Potential Applications of Cu ₂ O	9
1.5	Cupric Oxide (CuO)	10
1.5.1	Properties of CuO	10
1.5.2	Potential Applications of CuO.....	10
1.6	Thesis Objective and Overview	12
	References	15
Chapter 2	Phase-pure Cu ₂ O Films Fabricated by Spin-spray Method	19
2.1	Introduction	19
2.2	Experiments.....	20
2.2.1	Substrate and Chemicals	20
2.2.2	Fabrication of Cu ₂ O films via spin-spray method	20
2.2.3	Characterization	21
2.3	Results	22
2.3.1	Structural and material characterizations of Cu ₂ O Films	22
2.3.2	Morphology Observation of Cu ₂ O films	23
2.3.3	Optical properties of Cu ₂ O films.....	25
2.4	Discussion.....	27
2.4.1	Formation Mechanism of Cu ₂ O Films via Spin-spray method.....	27
2.4.2	Effect of NaOH on Sample Morphology and Growth Orientation	30
2.4.3	Effect of NH ₃ on Sample Morphology and Growth Orientation	31
2.4.4	Electrical properties of Cu ₂ O Films via Spin-spray method	32

Conclusion.....	33
References	34
Chapter 3 CuO Nanostructures Fabricated by Spin-spray Method	35
3.1 Introduction	35
3.2 Experiment	36
3.2.1 Substrate and chemicals	36
3.2.2 Fabrication of CuO nanostructures by spin-spray method.....	36
3.2.3 Characterization	37
3.3 Results	38
3.3.1 Characteristics of Nanostructured CuO Films.....	38
3.3.1 Morphology of Nanostructured CuO Films	40
3.3.2 Optical Properties of Nanostructured CuO Films.....	41
3.4 Discussion.....	42
3.4.1 Formation Mechanism of CuO dense film and nanosheet array	42
3.4.2 Surface properties of CuO dense film	46
3.4.3 Optical band gaps of CuO dense film and nanosheet array	46
Conclusion.....	47
References	48
Chapter 4 CuO Thin Film Fabricated by Mist Spin Spray Method	50
4.1 Introduction	50
4.2 Experiments.....	51
4.2.1 Fabrication of CuO films via the MSS method.....	51
4.2.2 Characterization and performance	52
4.3 Results	53
4.3.1 Structural and Material Characterizations of CuO Thin Films	53
4.3.2 Morphological Characterization of CuO Thin Films	56
4.3.3 Optical Characterization of CuO Thin Films.....	58
4.4 Discussion.....	58
4.4.1 Film Formation Mechanism	58
1.4.1.1 Thin Film Fabrication at Low Temperatures.....	58
4.4.2 Optical band gap evaluation	64
Conclusion.....	66
References	67

Chapter 5	Conductive ZnO Films Fabricated by Spin-spray Method	69
5.1	Introduction	69
5.2	Experiments.....	70
5.2.1	Fabrication of ZnO films via spin-spray method.....	70
5.2.2	Characterization	70
5.3	Results	71
5.3.1	Morphology and XRD Analysis of ZnO Film.....	71
5.3.2	Electrical and optical properties of ZnO Film	72
5.3.3	Elemental analysis of ZnO Film.....	73
5.4	Discussion.....	74
5.4.1	Donor Formation in ZnO Film by UV Treatment	74
5.4.2	Identification of Donor Species by Elemental Analysis.....	75
5.4.3	Hydrogen Donor Formation by UV Light Irradiation	77
	Conclusion.....	79
	References	80
Chapter 6	Flexible Applications of Metal Oxide Films Fabricated by Controlling Spin Spray Reaction.....	82
6.1	Introduction	82
6.2	Flexible Bending Sensor based on Cu ₂ O Films.....	83
6.2.1	Experiment	83
6.2.2	Result and Discussion.....	84
6.2.3	Applications of Cu ₂ O Bending Sensor.....	92
6.3	Flexible Photodetector based on Cu ₂ O/ZnO Films.....	97
6.3.1	Experiment	97
6.3.2	Results and Discussion	98
6.4	Flexible humidity sensor based on CuO nanostructures.....	101
6.4.1	Experiment	101
6.4.2	Results and Discussion	103
6.5	Flexible glucose sensor based on CuO Thin Film	112
6.5.1	Experiment	112
6.5.2	Results and Discussion	112
6.6	Conclusion.....	115
	References	118

Chapter 7 General Conclusions	120
Acknowledgments	124
List of Publications and Presentations.....	126

Chapter 1 General Introduction

1.1 Background of This Thesis

Sensors have played a key role in the development of human civilization. They have been used for different sectors like gas sensing,^{1,2} environmental monitoring,^{3,4} monitoring constituents in food products,^{5,6} and so on. As shown in **Figure 1.1**, sensors can be broadly classified into two categories, flexible⁷ and non-flexible⁸. Non-flexible sensors hindered by their rigidity from capturing analytes and therefore, were generally used in place. On the other hands, flexible sensors can capture target analytes more efficiently, indicating the high portability.⁹ There has been a recent increase in demand for flexible sensors because of the widespread use of wearable and healthcare device.¹⁰⁻¹³ Typically, they are composed of a flexible polymer substrate and sensing materials. Various types of sensing materials, including metal materials, conductive polymers, and functional metal oxide, have been used to fabricate flexible sensors.¹⁴⁻¹⁶ Among them, conducting polymers constructed as flexible sensors have been extensively explored due to their soft nature, high flexibility, stretchability, and skin affinity, which is able to sustain the mechanical deformation as wearable electronics.¹⁷ However, they are generally expensive, have low long-term stability, and require the complex and high-cost fabrication methods. On the other hands, the advantages of functional metal oxides, including their non-toxicity, low cost, and long-term durability, are of great significance in the development of flexible sensors for wearable electronics.¹⁸

Metal oxide films have been synthesized using many physical and chemical processes, such as radio frequency magnetron sputtering, pulsed laser deposition, chemical spray pyrolysis, and electrodeposition.¹⁹⁻²⁹ However, these methods may require

a vacuum system and high fabrication temperatures in addition to heat-resistant and/or conductive substrates, leading to certain disadvantages, such as high environmental impacts, significant expense or limited substrate ranges. Therefore, it is difficult to fabricate metal oxide films on flexible polymer substrates with low heat and chemical durability due to their high fabrication temperature and complex processes, resulting in few reports on metal oxide-based flexible sensors. Production of them requires novel approaches in fabrication processes for metal oxide films to reduce the damage to the substrates.

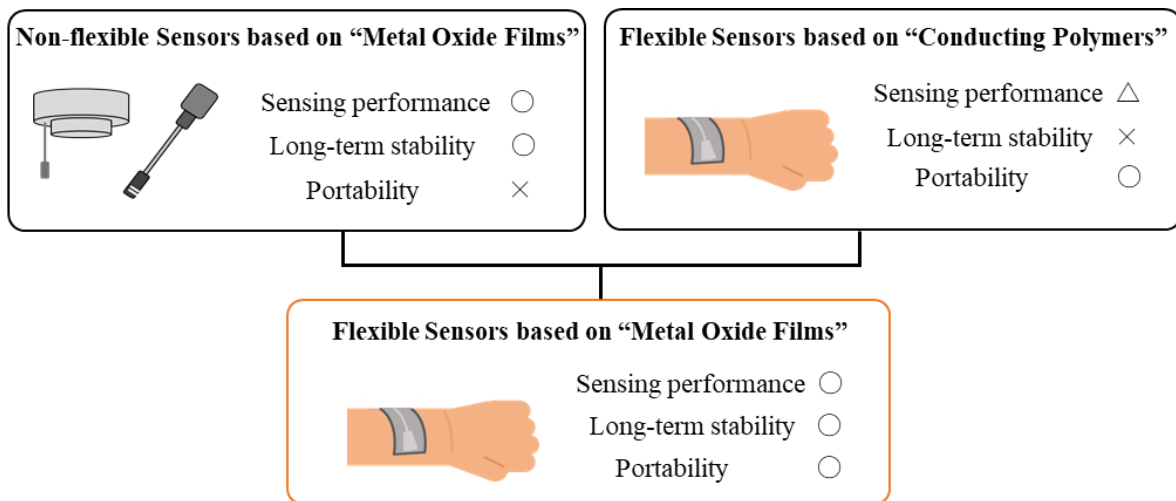


Figure 1.1 Schematic illustrations of flexible and non-flexible sensors.

1.2 Solution Processes for Fabrication Metal Oxide Films

To obtain flexible sensors for industrial and commercial needs, metal oxide films can be fabricated on polymer substrates such as polyimide and polyethylene terephthalate (PET) with good adhesion. Since the PET substrates have poor thermal durability, the metal oxide films should be fabricated at 150°C or less are. Solution processes, including chemical bath deposition (CBD), hydrothermal and successive ionic adsorption and

reaction (SILAR), have significant advantages over other techniques by allowing film fabrication at temperatures below 100 °C under atmospheric pressure. However, there were few reports of metal oxide films directly fabricated on polymer substrates because these methods damage the substrate as a result of their extended immersion in hot alkaline solution (several hours to a few days). To overcome the problems of conventional solution processes, “spin-spray method” and “mist spin spray method” have been applied to fabricate metal oxide films on polymer substrates. They do not adversely affect the substrate because of the low fabrication temperature and high deposition rate (which allows a short deposition time).

1.2.1 Spin-spray Method

Spin-spray method is one of the solution processes for metal oxide films. This method was initially developed for ferrite film fabrication, and we also achieved direct fabrication of Mn_3O_4 and ZnO films on substrates using this method.³⁶⁻³⁹ The spin-spray method is characterized by its low deposition temperature (< 100 °C), simple equipment, high deposition rate and low cost. **Figure 1.2** shows a schematic illustration of the spin-spray technique, where **(a)** is the side view and **(b)** is the top view. In this method, the two solutions are sprayed on the substrate placed on a rotating disk heated to a temperature below 100 °C. One is an aqueous solution of metal ions, referred to as the source solution. The other is an aqueous solution of alkaline chemicals, referred to as the reaction solution. The spin-spray method is utilizing chemical reaction, it is similar to that of CBD method and SILAR method. However, these two methods are completely different from the spin-spray method. In the CBD method, the film is fabricated in a stationary solution, and there is no temperature gradient or pH gradient in the reaction

field. On the other hand, in the spin spray method, there are temperature gradients and pH gradients in the reaction field since the two solutions with different pH values are separately sprayed onto heated substrates fixed on the rotating disk table, as shown in **Figure 1.2**. The SILAR method is similar to the spin-spray method in that the film is fabricated using two solutions. However, the chemical reaction for film fabrication is carried out statically and the substrate is once cleaned with pure water before being applied to the other solution. In the spin-spray method, the fresh solution is supplied continuously and the unreacted solution is removed via the centrifugal force.⁴⁰ Therefore, the spin-spray method has many advantages for films fabrication, such as one step fabrication and a high fabrication rate, compared to these fabrication methods.

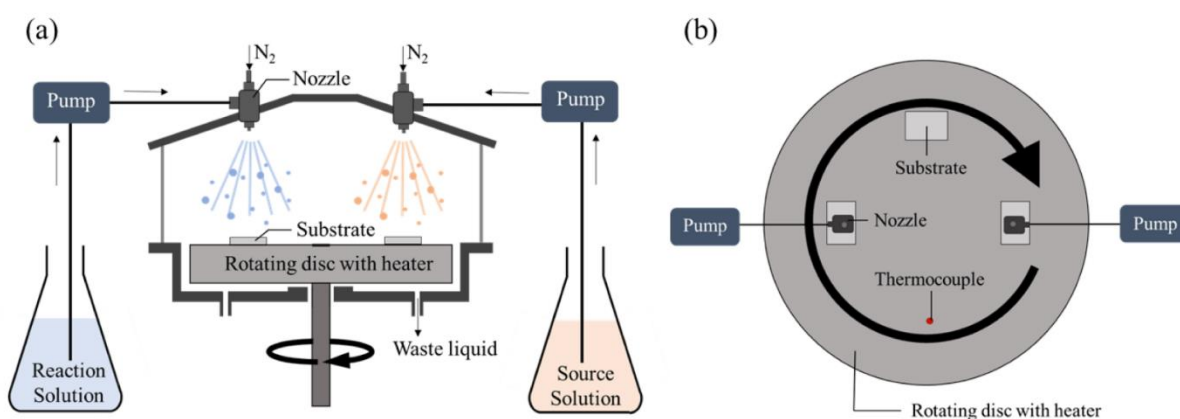


Figure 1.2 Schematic illustrations of the spin spray technique; (a) side view and (b) top view.

1.2.2 Mist Spin Spray Method

Mist spin spray (MSS) method was developed and used to fabricate metal oxide films. **Figure 1.3** shows the schematic illustration of the MSS apparatus. This method can be described as a kind of spin-spray method based on the use of so-called mist droplets

generated by the ultrasonication of a precursor solution. An ultrasonic transducer operating at a frequency of 2.4 MHz can provide droplets as small as 0.1–3 μm in diameter that are subsequently transported to the substrate via a carrier gas. In this method, two precursor solutions, referred to as the source and reaction solutions, respectively, are prepared as the same as the case for a standard spin-spray process. In contrast to the standard spin-spray method, the mist droplets are formed by ultrasonication of the two solutions and then sprayed onto the substrate, which is fixed on a rotating table. In this manner, dense and crack-free metal oxide thin films with nanoscale thicknesses can be fabricated within a short time span (30 min) at a relatively low temperature of 90°C through the effective utilization of chemical reactions. Therefore, it is an energy-saving and environment-friendly method compared with conventional physical and chemical processes. In addition, it is generally difficult to fabricate crystalline metal oxide thin films on polymer substrate with good adhesion by conventional solution processes since there is no epitaxial effect between the film and the substrate. The films fabricated by the MSS method strongly adhere to the substrate.

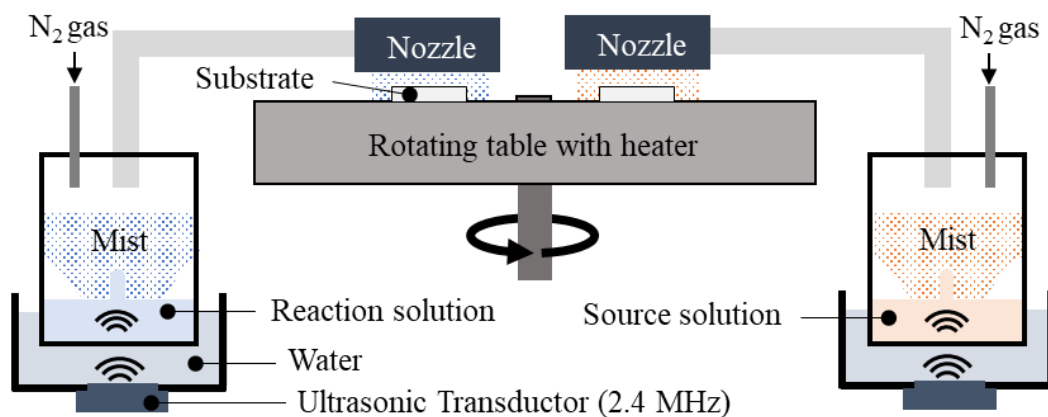


Figure 1.3 A schematic illustration of the mist spin spray apparatus.

1.2.3 Spin Spray Reaction

The spin-spray method and Mist spin spray (MSS) method enable to the low temperature fabrication of metal oxide films at low temperature below 100°C with high deposition rate through the effective utilization of “spin spray reactions”. **Figure 1.4** shows the illustration of the spin spray reaction. In the spin-spray method and MSS method, the source and reaction solution were sprayed onto the heated substrate and the liquid film was fabricated on the substrate surface. It is important for the fabrication of metal oxide films by these methods to increase the hydrophilicity of the substrate surface by the plasma treatment before the film fabrication. There were a large number of polar functional groups such as hydroxyl groups, on the substrate surface due to the hydrophilicity caused by plasma treatment (**Figure 1.4 (a)**). In the liquid film of the source solution, metal ions selectively absorb to the hydroxyl groups on the substrate surface (**Figure 1.4 (b)**). The metal ions and/or metal hydroxides are forced to hydrolyze when spraying the reaction solution to the substrate, resulting in the formation of metal oxides on the substrate (**Figure 1.4 (c)**). Since the hydroxyl groups supply in excess re-adhere on the oxide layer, the processes of adsorption, oxidation and crystallization is repeated, and the film grows in thickness with time (**Figure 1.4 (d)**).

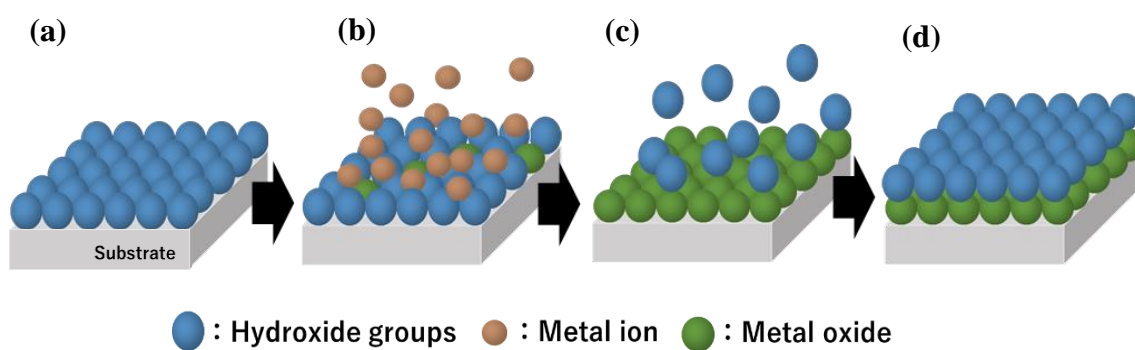


Figure 1.3 A schematic illustration of the spin spray reaction.

1.3 Zinc Oxide (ZnO)

1.3.1 Properties of ZnO

Zinc oxide (ZnO) has several desirable properties, including a wide energy band gap (3.37 eV), a large free exciton binding energy (60 meV) and good optical transparency in the visible light.⁴²⁻⁴³ ZnO has a hexagonal crystal system and a wurtzite crystal structure at ambient conditions, and belong to a space group of $P6_3mc$.⁴⁴ In this structure, one atom is located at the center of a tetrahedron formed by four atoms on one side. The distance between the atom at the apex of the tetrahedron and the atom at the center is 1.992 Å, which is almost equal to the ionic radius of 0.74 Å for tetraordinated Zn^{2+} and 1.24 Å for tetraordinated O^{2-} , indicating that both ions are in contact. Since the length of the tetrahedral ridge is 3.21 Å, which is much larger than the radii of both ions, the interaction between the ions located between the tetrahedral vertices can be neglected. **Table 1.1** show the basic properties of ZnO at 300 K. Since the wurtzite crystal structure does not have inversion symmetry and belongs to a polar space group, ZnO crystal exhibits crystallographic polarity along c-axis. This polarity provides an anisotropic growth along c-axis, a spontaneous polarization, and piezoelectricity.

Table 1.1 Basic properties of ZnO single crystal and bulk.

Properties	
a	0.32494 nm
b	0.32494 nm
c	0.52038 nm
α	90 deg.
β	90 deg.
γ	120 deg.
Density (g/cm ³)	5.6806
Stable phase at 300 K	Wurtzite

1.3.2 Potential Applications of ZnO

ZnO is ranked as a prominent third-generation semiconductor due to its various advantages of nontoxicity, chemical stability, rich defect properties, and easy to grow in a rich variety of nanostructures. ZnO is widely used in catalysis, electrical devices, optoelectronics, biological imaging, and energy harvesting & storage.⁴⁵ Those properties are relevant for cost-effective fabrication of next generation multiple functional devices on a single given substrate. In addition, the large exciton binding energy of ZnO (60 meV) paves the way for an intense near-band-edge excitonic emission at room and higher temperatures, because this value is 2.4 times that of the room-temperature (RT) thermal energy ($kBT=25\text{meV}$).⁴⁶ There have also been a number of reports on laser emission from ZnO-based structures at RT and beyond. However, it is difficult to fabricate a p-type ZnO semiconductor due to a strong self-compensation effect arising from the presence of native defects or hydrogen impurities. Kawasaki et al. developed the preparation of p-i-n junction only consisting ZnO and achieved violet electroluminescence.

1.4 Cuprous Oxide (Cu₂O)

1.4.1 Properties of Cu₂O

Cuprous oxide (Cu₂O) is a p-type semiconductor with a direct band gap of ~2.17 eV and has a cubic cuprite structure.⁴⁷ In this structure, each O ion is surrounded by four Cu ions and each Cu ion is surrounded by two O ions.

In the past, the conductivity of Cu₂O was investigated under various oxygen partial pressures to determine the defect species, and it was found that the defect species were vacancies in the copper sites or oxygen in the interstitial positions. Subsequent measurements of diffusion coefficients revealed that the mobility of vacancies in copper

sites is more than 10 times faster than that of oxygen in interstitial sites.^{48,49} It is now believed that the holes are generated by defect formation in the vacancies at the copper sites.

1.4.2 Potential Applications of Cu₂O

Cu₂O has been one of the most intensively investigated binary transition metal oxide crystals in the past decades. Besides the well-known merits including low-cost, nontoxicity, abundance and easy synthesis, the tailored architectures of Cu₂O crystals have attracted great research interests because of their physicochemical properties for achieving various functions. Cu₂O has generated significant interest for applications, including (1) optoelectronics^{50,51} (2) catalytic chemistry^{52,53} and (3) biosensors⁵⁴⁻⁵⁶, as described below.

(1) Optoelectronics^{50,51}

Cu₂O has been attracting attention as a light-absorbing layer in solar cells because of its ability to absorb light in the visible region. In order to further improve the power generation efficiency, not only the fabrication of high-purity Cu₂O film but also the control of its film structure is important. There are some reports that power generation efficiency was improved by increasing the particle size of Cu₂O and the texture structure of the interface where light is diffusely reflected.

(2) Catalytic chemistry^{52,53}

Cu₂O is expected to be a visible light responsive photocatalyst because it can absorb light in the visible range. In particular, there have been many reports on its application as a photoelectrode for water splitting. As a photoelectrode, it is important to

increase the surface area that can be in contact with water and therefore, there are many reports on the control of Cu₂O surface structure.

(3) Biosensors⁵⁴⁻⁵⁶

Cu₂O, which is non-toxic, has been reported to have many applications in the biomedical field. In recent years, there have been many reports on glucose sensors without using enzymes. It is important to increase the surface area that can be in contact with glucose and therefore, there are many reports on the control of Cu₂O surface structure.

1.5 Cupric Oxide (CuO)

1.5.1 Properties of CuO

Cupric oxide (CuO) is abundant, non-toxic and has a high visible light absorption coefficient.⁵⁷ CuO is a p-type semiconductor with an energy band gap of 1.2 eV and belongs to the monoclinic crystal system.⁵⁸ The copper atom is coordinated by 4 oxygen atoms in an approximately square planar configuration. In addition, CuO nanostructures with large surface areas and potential size effects possess superior physical and chemical properties that remarkably differ from those of their micro or bulk counterparts.⁵⁹⁻⁶¹ These nanostructures have been extensively investigated because of their promising applications in various fields.^{62,63}

1.5.2 Potential Applications of CuO

CuO is also promising materials for the fabrication of solar cells because of their high solar absorbance, low thermal emittance, relatively good electrical properties, and high carrier concentration.⁶⁴ CuO nanostructures are also considered as electrode materials for the next-generation rechargeable lithium-ion batteries (LIBs) because of their high theoretical capacity, safety, and environmental friendliness.⁶⁵⁻⁶⁷ Furthermore,

CuO nanostructures are extensively used in various other applications, including (1) gas sensors⁶⁸⁻⁷⁰ (2) biosensors⁷¹⁻⁷³ and (3) photocatalysis^{78,79} as described below.

(1) Gas sensors⁶⁸⁻⁷⁰

It is surface conductivity that makes CuO an ideal material for semiconductor resistive gas sensor applications and in fact CuO nanomaterials were used for detection of many different compounds such as CO, hydrogen cyanide and humidity. As sensing properties closely relate to the chemical reaction on the surface of sensor, the specific area is a key factor to achieve high sensitivity sensor.

(2) Biosensors⁷¹⁻⁷³

CuO, which is non-toxic, has been reported to have many applications in the biomedical field. In recent years, there have been many reports on high-performance glucose sensors without using enzymes. The better efficiency of the oxidized reaction in CuO based sensor resulted from high surface area, surface energy which enhanced electron transfer ability of CuO nanomaterials.

(3) Photocatalysis^{78,79}

CuO is expected to be a visible light responsive photocatalyst because it can absorb light in the visible range. However, some groups reported that CuO shows almost no or very little photocatalyst properties under visible light. Adding some amount of H₂O₂ could help to greatly improve the photocatalyst efficiency under visible light.

1.6 Thesis Objective and Overview

The main focuses of this thesis are shown as follows:

- (1) To fabricate Cu_2O , CuO and ZnO films by novel solution processes, including spin-spray method and mist spin spray method, at temperatures below 100°C .
- (2) To investigate the properties of the obtained Cu_2O , CuO and ZnO films, which include the material, optical, electrical characteristics.
- (3) To find out the potential flexible sensor applications for the Cu_2O , CuO and ZnO films fabricated on flexible polymer substrates by spin-spray method and mist spin spray method.

This thesis consists of 7 chapters. The chapter construction, which draft the relationship among each chapter is illustrate in **Figure 1.5**. The descriptions in each chapter is shown as follows:

Chapter 1 contains the background and objective of this study. The potential flexible sensor applications based on metal oxide films are introduced in this chapter. The schematics and general procedure of spin-spray method and mist spin spray method for fabrication of metal oxide based-flexible sensors are demonstrated. It suggested that all of these processes using utilizing spin spray reaction do not deteriorate the substrate duet to their low fabrication temperature and short deposition time. Besides, basic properties and potential applications of the Cu_2O , CuO and ZnO films are described.

Chapter 2 presents the fabrication of phase-pure Cu_2O films on glass substrates by the spin-spray method. The formation mechanism of Cu_2O films is proposed by using XRD and FESEM analysis. Control of the grain size, the crystalline orientation of the

films, the surface morphology, and the optical band gap by adjusting the precursor solution condition is discussed.

Chapter 3 describes the effect of irradiated UV light on the optical and electrical properties of the spin-sprayed ZnO films. UV-vis analysis shows the increase of carrier concentration indicating the generation of new donors in the ZnO film by UV treatment. The conductive improvement mechanism of the ZnO film by UV light irradiation is discussed.

Chapter 4 shows the fabrication of CuO nanostructures on glass substrates by the spin-spray method. The formation mechanism of CuO nanostructures is proposed by using FESEM analysis. The morphology-controlled synthesis of CuO nanostructures by using different complexing agents in the precursor solution is discussed.

Chapter 5 focuses on the fabrication of CuO thin films by the mist spin spray method. The formation mechanism of CuO thin films is proposed by using FESEM analysis. This method allows precise control of the film grain size, surface morphology and optical band gap by adjusting the compositions of the initial solutions.

In *Chapter 6*, the spin-spray method and MSS method are applied to fabricate metal oxide films on PET substrates for flexible sensor applications, including bending sensors, flexible photodetector, flexible humidity sensors and flexible glucose sensors. Their sensitivity, resolution, stability and mechanical fatigue durability are evaluated. Optimization of the particle size, film thickness, and film morphology by controlling the spin spray reactions is discussed to fabricate metal oxide film-based flexible sensors with high sensing performance and mechanical fatigue durability,

Chapter 7 summarize and generally conclude the thesis.

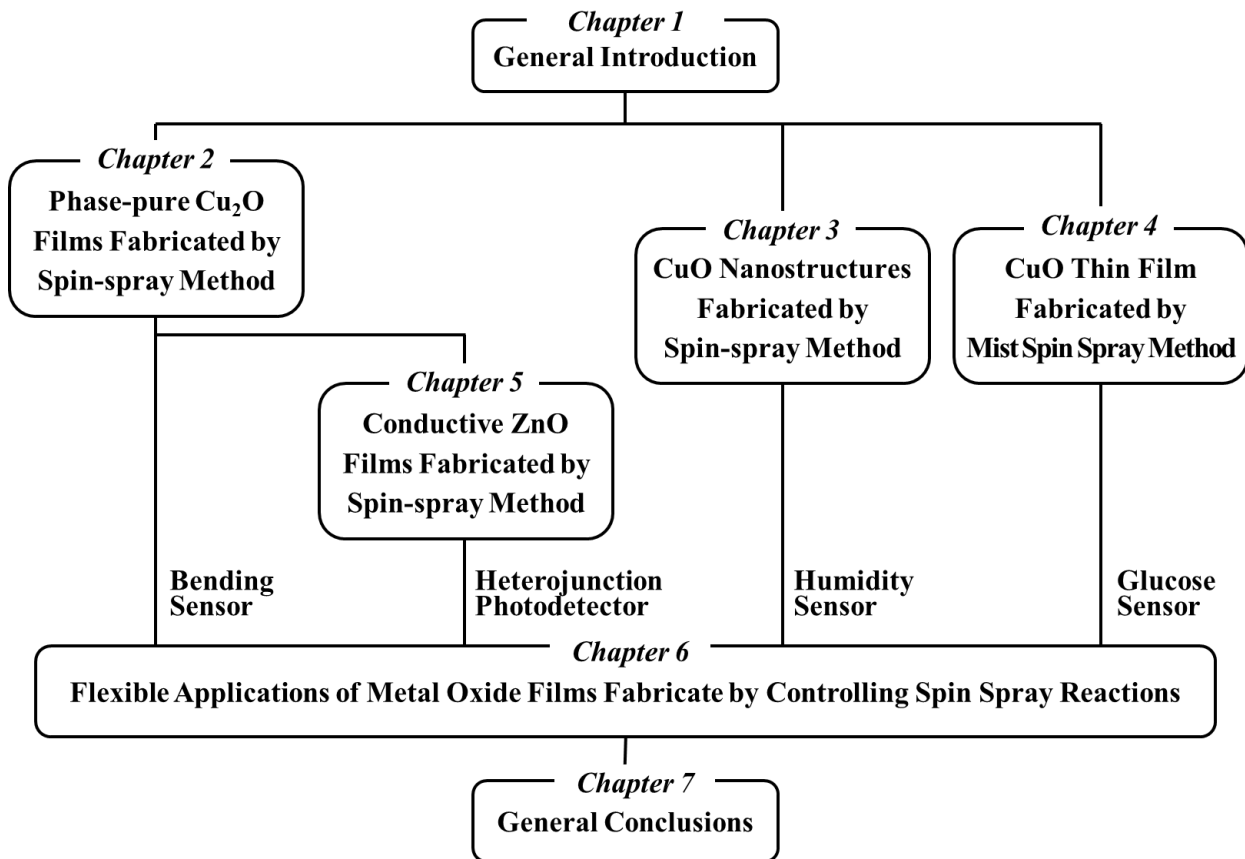


Figure 1.5 Flow chart of this thesis.

References

- [1] A. Nag, A. I. Zia, X. Li, S. C. Mukhopadhyay, J. Kosel, *IEEE Sensors J.*, 164 (2016) 996–1003
- [2] A. Nag, A. I. Zia, X. Li, S. C. Mukhopadhyay, J. Kosel, *IEEE Sensors J.*, 164 (2016) 1088–1094, Feb. 2016
- [3] N. Suryadevara, S. C. Mukhopadhyay, R. K. Rayudu, and Y. M. Huang, *IEEE Int. Instrum. Meas. Technol. Conf. (IMTC)*, May 2012, pp. 947–952.
- [4] M. A. M. Yunus and S. C. Mukhopadhyay, *Meas. Sci. Technol.*, 22-2 (2011) 025107.
- [5] S. C. Mukhopadhyay and C. P. Gooneratne, *IEEE Sensors J.*, 7-9 (2007) 1340–1346.
- [6] A. I. Zia, S. C. Mukhopadhyay, I. H. Al-Bahadly, P. L. Yu, C. P. Gooneratne, and J. Kosel, in *Proc. IEEE Int. Instrum. Meas. Technol. Conf. (IMTC)*, May 2014, pp. 838–843.
- [7] L. Duan, D.R. D’hooge, L. Cardon, *Prog. Mater. Sci.* 114 (2020) 100617.
- [8] L. Wiik-Fuchs, L. Diehl, R. Mori, M. Hauser, K. Jakobs, S. Kühn, U. Parzefall, A.A. Affolder, V. Fadeyev, C. García, C. Lacasta, D. Madaffari, U. Soldevila, Y. Unno, *Nucl. Instruments Methods Phys. Res. Sect. A Accel. Spectrometers, Detect. Assoc. Equip.* 924 (2019) 128–132.
- [9] S.T. Han, H. Peng, Q. Sun, S. Venkatesh, K.S. Chung, S.C. Lau, Y. Zhou, V.A.L. Roy, *Adv. Mater.* 29 (2017) 1–22.
- [10] Y. Wei, S. Chen, F. Li, Y. Lin, Y. Zhang, L. Liu, *ACS Appl. Mater. Interfaces.* 7 (2015) 14182–14191.
- [11] S. Kim, M. Amjadi, T.-I. Lee, Y. Jeong, D. Kwon, M.S. Kim, K. Kim, T.-S. Kim, Y.S. Oh, I. Park, *ACS Appl. Mater. Interfaces.* 11 (2019) 55.
- [12] A.Z. Liao, W.D. Zhu, J.B. Chen, X.Q. Zhang, C.W. Wang, *J. Alloys Compd.* 609 (2014) 253–261.
- [13] G. Gerboni, A. Diodato, G. Ciuti, M. Cianchetti, A. Menciassi, *IEEE/ASME Trans. Mechatronics.* 22 (2017) 1881–1888.
- [14] B. Sun, Y.Z. Long, S.L. Liu, Y.Y. Huang, J. Ma, H. Di Zhang, G. Shen, S. Xu, *Nanoscale.* 5 (2013) 7041–7045.
- [15] V.K. Samoei, A.H. Jayatissa, *Sensors Actuators, A Phys.* 303 (2020) 111816.
- [16] C. Dong, Y. Fu, W. Zang, H. He, L. Xing, X. Xue, *Appl. Surf. Sci.* 416 (2017) 424–431.
- [17] S. Xu, X.L. Shi, M. Dargusch, C. Di, J. Zou, Z.G. Chen, *Prog. Mater. Sci.* 121 (2021) 100840.

- [18] W. Deng, T. Yang, L. Jin, C. Yan, H. Huang, X. Chu, Z. Wang, D. Xiong, G. Tian, Y. Gao, H. Zhang, W. Yang, *Nano Energy*. 55 (2019) 516–525.
- [19] M. Hari Prasad Reddy, P. Narayana Reddy, S. Uthanna, *Indian J. Pure Appl. Phys.* 48 (2010) 420–424.
- [20] S. Ishizuka, T. Maruyama, K. Akimoto, *Jpn. J. Appl. Phys.* 39 (2000) 2–8A.
- [21] A. Chen, H. Long, X. Li, Y. Li, G. Yang, P. Lu, *Vacuum* 83 (2009) 927–930.
- [22] X. Liu, M. Xu, J. Ma, X. Zhang, C. Luan, X. Feng, *Ceram. Int.* 43 (2017) 15500–15504.
- [23] M.F. Al-Kuhaii, *Vacuum*. 82 (2008) 623–629..
- [24] A. E. Kasmi, Z. Tian, H. Vieker, A. Beyer, T. Chafik, *Applied Catalysis B: Environmental*. 186 (2016) 10–18.
- [25] T. Kosugi, S. Kaneko, *J. Am. Ceram. Soc.* 81 (1998) 3117–3124.
- [26] B. Balamurugan, B. R. Mehta, *Thin Solid Films* 396 (2001) 90–96.
- [27] S. Bijani, L. Martinez, M. Gabás, E.A. Dalchiele, J. R. Ramos-Barrado, *J. Phys. Chem. C*. 113 (2009) 19482–19487.
- [28] M.J. Siegfried, K.-S. Choi, *Chem. Int. Ed.* 44 (2005) 3218–3223.
- [29] J. Cui, U. J. Gibson, *J. Phys. Chem. C*. 114 (2010) 6408–6412.
- [30] H.Y. Xu, C. Chen, L. Xu, J.K. Dong, *Thin Solid Film* 527 (2013) 76–80.
- [31] H. Xu, J.K. Dong, C. Chen, *Mater. Chem. Phys.* 143 (2014) 713–719.
- [32] T. Terasako, K. Ohnishi, H. Okada, S. Obara, M. Yagi, *Thin Solid Films* 644 (2017) 146–155.
- [33] T. Jiang, Y. Wang, D. Meng, X. Wu, J. Wang, J. Chen, *Appl. Surf. Sci.* 311 (2014) 602–608.
- [34] Z. Li, J. Wang, N. Wang, S. Yan, W. Liu, Y.Q. Fu, Z. Wang, *J. Alloys Compd.* 727 (2017) 1136–1143.
- [35] A. Ray, I. Maukhopadhyay, R. Pati, Y. Hattori, U. Prakash, Y. Ishii, S. Kawasaki, *J. Alloys Compd.* 695 (2017) 3655–3665.
- [36] Y. Shimada, N. Matsushita, M. Abe, K. Kondo, T. Chiba, S. Yoshida, *J. Magn. Magn. Mater.* 278 (2004) 256–262.
- [37] H. Wagata, N. Ohashi, K. Katsumata, H. Segawa, Y. Wada, H. Yoshikawa, S. Ueda, K. Okada, N. Matsushita, *J. Mater. Chem.* 22 (2012) 20706.
- [38] H. Lin, Y. Katayanagi, T. Kishi, T. Yano, N. Matsushita, *RSC Adv.* 8 (2018) 30310–30319.

- [39] R. Nitta, Y. Kubota, T. Kishi, T. Yano, N. Matsushita, *Mater. Chem. Phys.* 243 (2020) 122442
- [40] H. Wagata, N. Ohashi, T. Taniguchi, A. K. Subramani, K. katsumata, K. Okada, N. Matsushita, *Cryst. Growth Des.* 10 (2010) 3502–3507.
- [41] H. Nishinaka, Y. Kamada, N. Kameyama, S. Fujita, *Phys. Status Solidi Basic Res.* 247 (2010) 1460–1463.
- [42] D.B. Potter, M.J. Powell, I.P. Parkin, C.J. Carmalt, *J. Mater. Chem. C.* 6 (2018) 588–597.
- [43] T. Coman, D. Timpu, V. Nica, C. Vitelaru, A.P. Rambu, G. Stoian, M. Olaru, C. Ursu, *Appl. Surf. Sci.* 418 (2017) 456–462.
- [44] A. Mallick, D. Basak, *Prog. Mater. Sci.* 96 (2018) 86–110.
- [45] E. Fortunato, A. Gonçalves, A. Pimentel, P. Barquinha, G. Gonçalves, L. Pereira, I. Ferreira, R. Martins, *Appl. Phys. A Mater. Sci. Process.* 96 (2009) 197–205.
- [46] A. Mallick, D. Basak, *Prog. Mater. Sci.* 96 (2018) 86–110.
- [47] Y. Yu, F.P. Du, J.C. Yu, Y.Y. Zhuang, P.K. Wong, *J. Solid State Chem.* 177 (2004) 4640.
- [48] N. L. Peterson, C. L. Wiley, *J. Phys. Chem. Solids*, 45 (1984) 281
- [49] P. Ochinnikov, C. Petot, G. Petot-Ervias, *Solid State Ionics*, 12 (1984) 135.
- [50] Z. Zang, *Appl. Phys. Lett.* 112 (2018) 042106
- [51] M. Berginski, J. Hupkes, M. Schulte, G. Schope, B. Rech, M. Wutting, *J. Appl. Phys.* 101 (2007) 7-4903
- [52] J. Luo, L. Steier, M. Son, M. Schreier, T. Mayer, M. Gratzel, *Nano Lett.* 16 (2016) 1848-1857
- [53] Foo ML, Matsuda R, Kitagawa. *Chem Mater*, 26 (2014) 310–22.
- [54] Lu N, Shao CL, Li XH, Shen T, Zhang MY, Miao FJ, *RSC Adv* 4 (2014) 31056–61.
- [55] Devadoss A, Sudhagar P, Ravidhas C, Hishinuma R, Terashima C, Nakata K. *Phys Chem* 16 (2014) 21237–42.
- [56] Yang Q, Long M, Tan L, Zhang Y, Ouyang J, Liu P *ACS Appl Mater Interfaces* 7 (2015) 29–30.
- [57] A. Inyang, G. Kibambo, M. Palmer, F. Cummings, M. Masikini, C. Sunday, M. Chowdhury, *Thin Solid Films.* 709 (2020) 138244.
- [58] B. Balamurugan, B.R. Mehta, *Thin Solid Films* 396 (2001) 90-96.
- [59] F. Mumm, P. Sikorski, *Nanotechnology* 22 (2011) 105605.

- [60] F. Li, X. Liu, Q. Zhang, T. Kong, H. Jin, , Cryst. Res. Technol. 47 (2012) 1140-1147.
- [61] M. Outokesh, M. Hosseinpour, S.J. Ahmadi, T. Mousavand, S. Sadjadi, W. Soltanian, Ind. Eng. Chem. Res. 50 (2011) 3540-3554.
- [62] T. Jiang, Y. Wang, D. Meng, X. Wu, J. Wang, J. Chen, Appl. Surf. Sci. 311 (2014) 602-608.
- [63] Z. Li, J. Wang, N. Wang, S. Yan, W. Liu, Y.Q. Fu, Z. Wang, J. Alloys Compd. 727 (2017) 1136-1143.
- [64] Q. Zhang, K. Zhang, D. Xu, G. Yang, H. Huang, F. Nie, C. Liu, S. Yang, Prog. Mater. Sci. 60 (2014) 208–337.
- [65] Dar Ma, Nam SH, Kim YS, Kim WB. J Solid State Electrochem 14(2010)1719–26.
- [66] Xiang JY, Tu JP, Yuan YF, Wang XL, Huang XH, Zeng ZY. Electrochim Acta 54(2009)1160–5.
- [67] Gao X, Bao J, Pan G, Zhu H, Huang P, Wu F, et al. J Phys Chem B 108(2004)5547–51.
- [68] Can, N. Electrospun Mater. et al. Chem. Phys. 213(2018) 6–13
- [69] Hou, L.; Zhang, C.; Li, L.; Du, C.; Li, X.; Kang, X.-F.; Chen,W. Talanta 188(2018)41–49.
- [70] Oosthuizen, D.N.; Motaung, D.E.; Swart, H.C. Actuators B Chem. 266,(2018)761–772.
- [71] Liu S, Tian J, Wang L, Qin X, Zhang Y, Luo Y, et al. Catal Sci Technol 2(2012)813–7.
- [72] Wang M-F, Huang Q-A, Li X-Z, Wei Y. Anal Methods 4(2012)3174.
- [77] HussainIbupoto Z, Khun K, BeniV, Liu X, Willander M. Sensors 13(2013)7926–38.
- [78] H. Xu, G. Zhu, D. Zheng, C. Xi, X. Xu, X. Shen, J. Colloid Interface Sci. 383 (2012) 75–81.
- [79] S. Liu, J. Tian, L. Wang, Y. Luo, X. Sun, Catal. Sci. Technol. 2 (2012) 339–344.

Chapter 2 Phase-pure Cu₂O Films Fabricated by Spin-spray Method

2.1 Introduction

Cu₂O films have generated significant interest for a wide range of applications including catalysts, gas sensors, biosensors, and solar cells owing to their p-type conductivity, natural abundance, non-toxicity, and a high visible light absorption coefficient.¹ Over the past decades, various physical and chemical methods have been proposed to fabricate Cu₂O films.²⁻⁵ However, they have disadvantages such as a high environmental load, high cost, and limited substrate choice because they require a high vacuum, high fabrication temperature, a heat-resistant substrate, and/or a conductive substrate. In addition, most of these techniques result in Cu₂O films that have impurities such as Cu, CuO, and Cu(OH)₂. These impurities have a negative impact on optical and electrical properties, and therefore, the fabrication process of the phase-pure Cu₂O films have to be investigated and developed for the Cu₂O-based device applications. Besides, it is also important to control the morphology and exposed crystal planes appropriately since these properties have serious impact to the device performances.¹

In this chapter, the spin-spray method was applied for fabricating phase-pure Cu₂O films on the seed-free glass substrates. It is generally difficult to fabricate crystalline Cu₂O films on amorphous glass substrates with good adhesion by conventional solution processes since there is no epitaxial effect between the film and the substrate. The Cu₂O films fabricated by the spin-spray method strongly adhere to the glass substrate. This method also allowed precise control of the film grain size, surface morphology and optical band gap by adjusting the compositions of the initial solutions.

2.2 Experiments

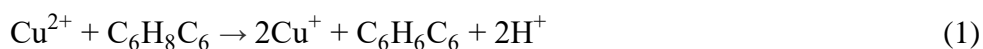
2.2.1 Substrate and Chemicals

Borosilicate glass substrates were purchased from MATUSNAMI GLASS Ind., Ltd., Japan. Copper (II) sulfate pentahydrate ($\text{CuSO}_4 \cdot 5\text{H}_2\text{O}$, 99.0 %), ascorbic acid ($\text{C}_6\text{H}_8\text{O}_6$, 99.0 %), sodium hydroxide (NaOH, 99.0 %), and ammonia (NH_3 aq. 28 w%) were all purchased from FUJIFILM Wako Pure Chemical Corporation, Ltd., Japan. All the chemicals were used as received without further purification. Deionized water was used for all the experiments.

2.2.2 Fabrication of Cu_2O films via spin-spray method

Cu_2O films were fabricated on borosilicate glass ($30 \times 40 \times 0.20$ mm) via the spin-spray method. Before fabrication, the substrates were ultrasonically cleaned in deionized water for 10 min, and were then treated using a ultraviolet-ozone cleaner (BioForce Nanosciences, Inc., USA, UV Ozone Cleaner ProCleaner™ Plus) for 10 min to increase the surface hydrophilicity.

The source and reaction solutions were sprayed on to the substrate placed on the rotating disk table heated to 70°C , and the rotation rate of the table was 150 rpm. The source solution was prepared by dissolving 0.04 M of $\text{CuSO}_4 \cdot 5\text{H}_2\text{O}$ and L-Ascorbic Acid in 0.7 L of deionized water at pH 2.3. Here, L-Ascorbic Acid was used as a kind of reducing agent. Their reduction reaction in the source solution is given below.



Three kinds of reaction solution were prepared using the different concentrations of NH_3 aq. solution (0.2, 0.6, 1.2 M), the different concentrations of NaOH solutions (0.2, 0.4, 0.6 M), and their mixture. The concentration of NaOH and NH_3 in the mixed solution was

changed in the range from 0.2–0.6 M and from 0.2–1.2 M, respectively. The supply rate for each solution was 50 mL/min, and the duration of the film deposition was 10 min. After the deposition, the Cu₂O films were ultrasonically cleaned in deionized water for 10 min. The sample fabricated using a mixed solution with different NaOH and NH₃ aq. concentrations, is expressed as the sample name of S_x-A_y. Here, x and y are the concentrations of NaOH (Sodium hydroxides) and NH₃ aq. (aqueous Ammonia), respectively.

2.2.3 Characterization

The crystallinity and microstructure of the samples were analyzed using X-ray diffraction (XRD; BRUKER Co., USA, D8 FOCUS/TXS) at a scan angle (2θ) in the range of 20–80°. X-ray at a wavelength of 0.15418 nm was generated using a Cu-K α source applying at 35 kV and 50 mA. The surface morphologies of the samples were examined using field-emission scanning electron microscopy (FESEM, HITACHI, Japan, S-4700) in secondary electron mode at a working voltage of 8 kV. After drying the samples at 60 °C for 24 h, X-ray photoelectron spectroscopy (XPS; Physical Electronics, Inc., USA, PHI 5000) was used to investigate the chemical states. All the XPS spectra were fitted using a numerical simulation program (XPSPEAK 41) with a Shirley background and a Lorentzian/Gaussian line shape. The presence of impurities in the samples was confirmed using attenuated total reflection Fourier-transform infrared (ATR-FTIR) spectroscopy (FT-IR IRPrestige-21, Shimadzu Corp., Japan).

2.3 Results

2.3.1 Structural and material characterizations of Cu₂O Films

The formed Cu₂O powders were just stuck on the surface of the substrate when only NaOH solution was used as the reaction solution. These Cu₂O powders did not adhere strongly to the substrate, and they were all dislodged from the substrate after ultrasonic cleaning in deionized water. On the other hand, neither Cu₂O film formation nor Cu₂O powder precipitation occurred when solutions of only NH₃ were used as the reaction solution. In contrast, for the case of the mixed NaOH and NH₃ solutions, Cu₂O films could be fabricated on the substrates at all the investigated NaOH and NH₃ aq. concentrations. **Figure 2.1** shows photos of the Cu₂O films fabricated on glass substrates using the various mixed solutions. As shown in **Figure 2.1**, the spin-spray method enabled to the one-step fabrication of dense Cu₂O films on the seed-free glass substrates at low temperature of 70°C and in a short time of 10 min. In addition, the films did not peel off from the substrates even after ultrasonic cleaning for 10 min, indicating good adhesion between the films and the substrates.

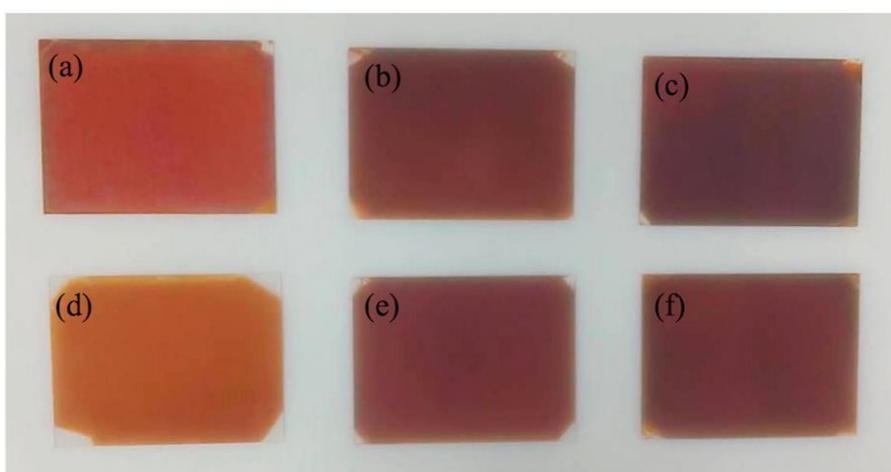


Figure 2.1 Photos of Cu₂O films fabricated on glass substrates using NaOH and NH₃ mixed solution with the different concentrations as the reaction solution; (a) S_{0.2}-A_{0.8}, (b) S_{0.3}-A_{0.8}, (c) S_{0.4}-A_{0.8}, (d) S_{0.4}-A_{0.2}, (e) S_{0.4}-A_{0.4}, (f) S_{0.4}-A_{1.2}.

Figure 2.2 (a) shows the XRD patterns for the Cu₂O films fabricated from the mixed solutions with different NaOH and NH₃ concentrations. All the peaks were in good agreement with the standard JCPDS card for cubic Cu₂O. As shown in **Figure 2.2 (a)**, S_{0.2}-A_{0.8} was strongly oriented in the [100], and the relative intensity of (111) to (200) continuously increased with increasing NaOH concentration from 0.2 to 0.4 M. In addition, S_{0.4}-A_{1.2} was strongly oriented in the [100], and the relative intensity of (111) to (200) continuously increased with decreasing NH₃ concentration from 0.2 to 0.4 M.

Figure 2.2 (b) shows the ATR-FTIR spectra of S_{0.2}-A_{0.8} and S_{0.4}-A_{1.2}. The band at around 600 cm⁻¹ is attributed to the vibrational mode of Cu-O in Cu₂O.⁶ On the other hand, there were no bands between 3000–3500 cm⁻¹, which corresponds to O-H and N-H stretch band.^{7,8} Also, the ascorbic acid band was not detected from the ATR-FTIR spectra. Therefore, the Cu₂O films fabricated by spin-spray method contain no impurities, such as OH, amines, and ascorbic acid. **Figure 2.2 (c)** shows the XPS spectra of the Cu2p_{3/2} peaks for S_{0.4}-A_{0.2}, S_{0.2}-A_{0.8} and S_{0.4}-A_{1.2}. The fitting of the peaks indicates a binding energy of 932.6 eV, corresponding to that of Cu⁺ in Cu₂O.⁹ In addition, no other diffraction peaks arising from possible impurities such as Cu, CuO and Cu(OH)₂ were detected, indicating that phase-pure Cu₂O was successfully fabricated.

2.3.2 Morphology Observation of Cu₂O films

Figure 2.3 (a)-(f) shows the surface and the cross-sectional SEM images of S_{0.2}-A_{0.8}, S_{0.3}-A_{0.8}, and S_{0.4}-A_{0.8}. S_{0.2}-A_{0.8} had a very flat surface with low light scattering and higher transparency than other samples. Most of the exposed grains of S_{0.2}-A_{0.8} have flat planes. On the other hand, for S_{0.3}-A_{0.8} and S_{0.4}-A_{0.8}, four-sided pyramidal grains appeared on the surface. **Figure 2.3** shows that the thickness of the films increased in tandem with

the increasing NaOH concentration and was 1.95, 2.79, and 3.18 NaOH concentrations of 0.2, 0.3, and 0.4 M, respectively. **Figure 2.4 (a)-(f)** shows the surface and the cross-sectional SEM images of $S_{0.4}-A_{0.2}$, $S_{0.4}-A_{0.4}$, and $S_{0.4}-A_{1.2}$. It shows that $S_{0.4}-A_{1.2}$ is a continuous uniform film composed of submicron sized grains, while $S_{0.4}-A_{0.2}$ and $S_{0.4}-A_{0.4}$ are films composed of octahedral nanoparticles. The grain size and film thickness of $S_{0.4}-A_{0.2}$ and $S_{0.4}-A_{0.4}$ were smaller than those of $S_{0.4}-A_{1.2}$, indicating that the higher ammonia concentration tended to cause a higher fabrication rate for the film.

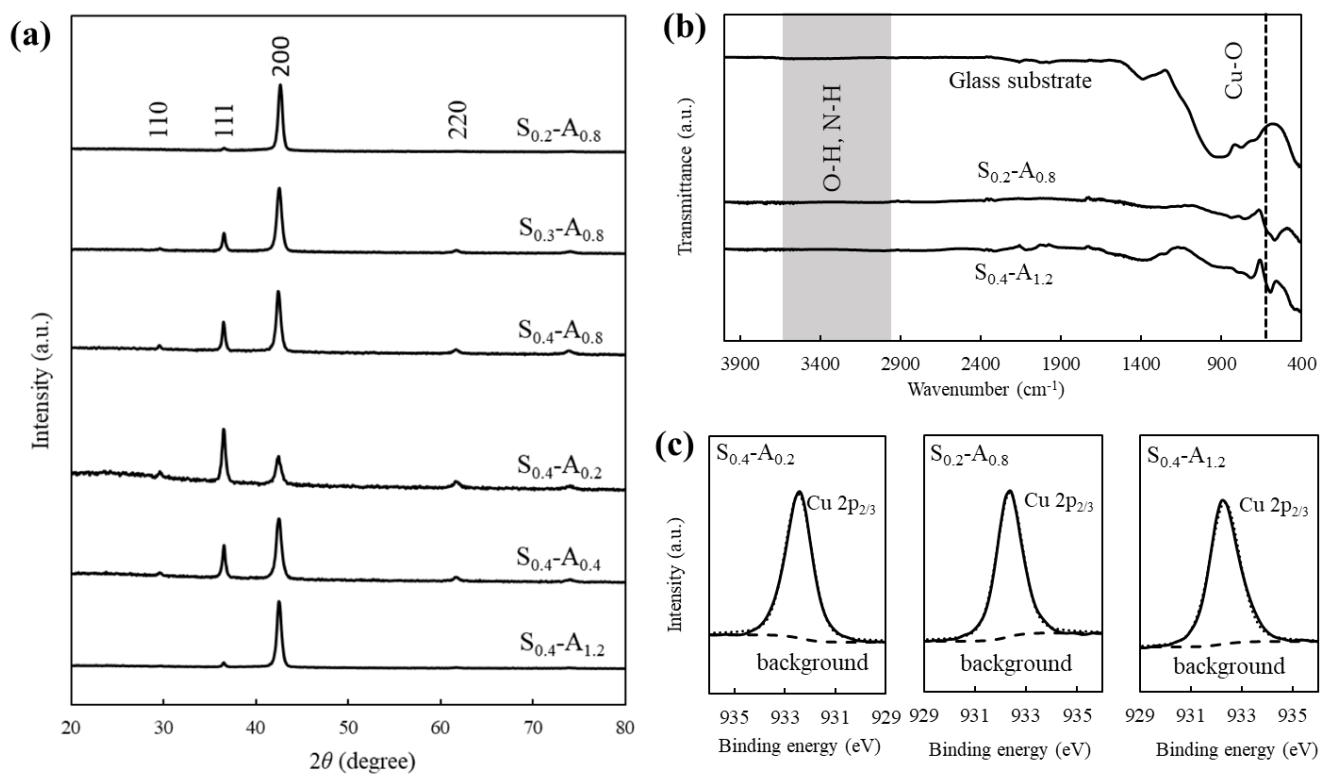


Figure 2.2 (a) XRD patterns, (b) ATR-FTIR spectra and (c) XPS spectra of Cu_2O film fabricated using NaOH and NH_3 mixed solution with the different concentrations.

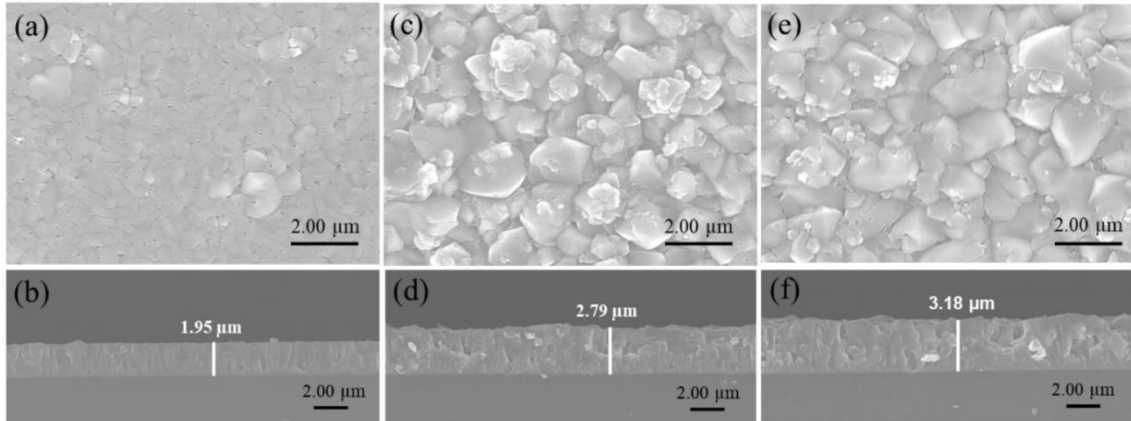


Figure 2.3 Surface and cross-sectional SEM images of (a)(b) $S_{0.2}-A_{0.8}$, (c)(d) $S_{0.3}-A_{0.8}$, (e)(f) $S_{0.4}-A_{0.8}$.

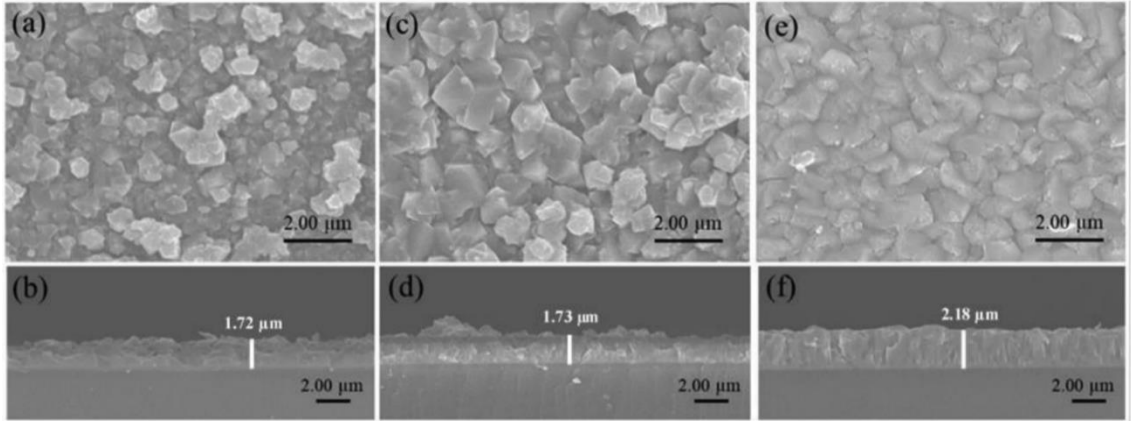


Figure 2.4 Surface and cross-sectional SEM images of (a)(b) $S_{0.4}-A_{0.2}$, (c)(d) $S_{0.4}-A_{0.4}$, (e)(f) $S_{0.4}-A_{1.2}$.

2.3.3 Optical properties of Cu_2O films

The optical band gap of Cu_2O films should be designed for applications such as photocatalysis and solar cell electrodes. The estimated optical band gap was obtained using the following equation for a semiconductor.

$$Ah\nu = K(h\nu - E_g)^{m/2} \quad (6)$$

Where A is the absorption coefficient, $h\nu$ is the photon energy, E_g is the optical band gap, K is a constant, and m is equal to 1 for band gaps with a direct transition and 2 for indirect

transitions. The absorption coefficient A was obtained using the equation $Ah\nu = -(\ln T)/d$, where d is the film thickness (nm) and T is the transmittance.

Figure 2.5 shows the plots of $(Ah\nu)^2 - hv$ for $S_{0.2}-A_{0.8}$, $S_{0.3}-A_{0.8}$, $S_{0.4}-A_{0.8}$, $S_{0.4}-A_{0.2}$, $S_{0.2}-A_{0.4}$, and $S_{0.4}-A_{1.2}$ in a direct transition. The intercept of the $(Ah\nu)^2 - hv$ plot along the $h\nu$ axis determines the band gap E_g . The band gaps of $S_{0.2}-A_{0.8}$, $S_{0.3}-A_{0.8}$, $S_{0.4}-A_{0.8}$, $S_{0.4}-A_{0.2}$, $S_{0.2}-A_{0.4}$, and $S_{0.4}-A_{1.2}$ were 2.20, 2.13, 2.14, 2.31, 2.13, and 2.05 eV, respectively. From **Figure 2.3** and **2.4**, the films with small particle sizes, i.e., $S_{0.4}-A_{0.2}$ and $S_{0.4}-A_{0.8}$, had large band gap values and the films with large particle sizes, i.e., $S_{0.4}-A_{1.2}$ and $S_{0.2}-A_{0.8}$, had low band gap values. Since the grain size of $S_{0.4}-A_{0.2}$ and $S_{0.4}-A_{0.8}$ were between 100–600 nm, the large band gap values can be attributed to quantum confinement effects.^{18,19}

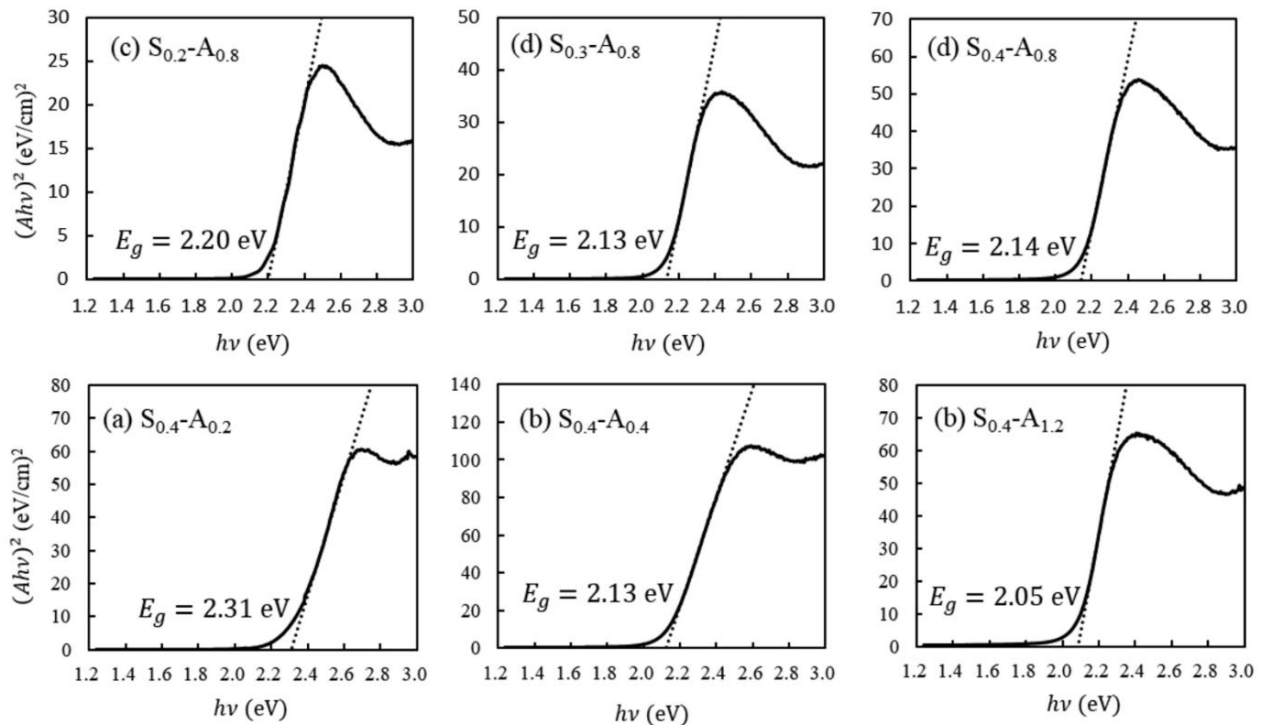


Figure 2.5 Tauc plots of (a) $S_{0.2}-A_{0.8}$, (b) $S_{0.3}-A_{0.8}$, (c) $S_{0.4}-A_{0.8}$, (d) $S_{0.4}-A_{0.2}$, (e) $S_{0.4}-A_{0.4}$ and (f) $S_{0.4}-A_{1.2}$.

2.4 Discussion

2.4.1 Formation Mechanism of Cu_2O Films via Spin-spray method

For the spin-spray method, the source and the reaction solution were sprayed onto the substrate and the unreacted solutions that had not contributed to film formation cleared out by the centrifugal force. In this situation, there was a reaction field of the “liquid film” on the rotating disk and the substrate was placed in this liquid film, as shown in **Figure 2.6 (a)**. In addition, there is a large temperature difference between the liquid film surface, on to which the room temperature solutions were sprayed continuously, and the substrate surface heated to $\geq 70^\circ\text{C}$ on the rotating table, as shown in **Figure 2.6 (b)**. The liquid film played an important role on the Cu_2O film formation on the substrate.

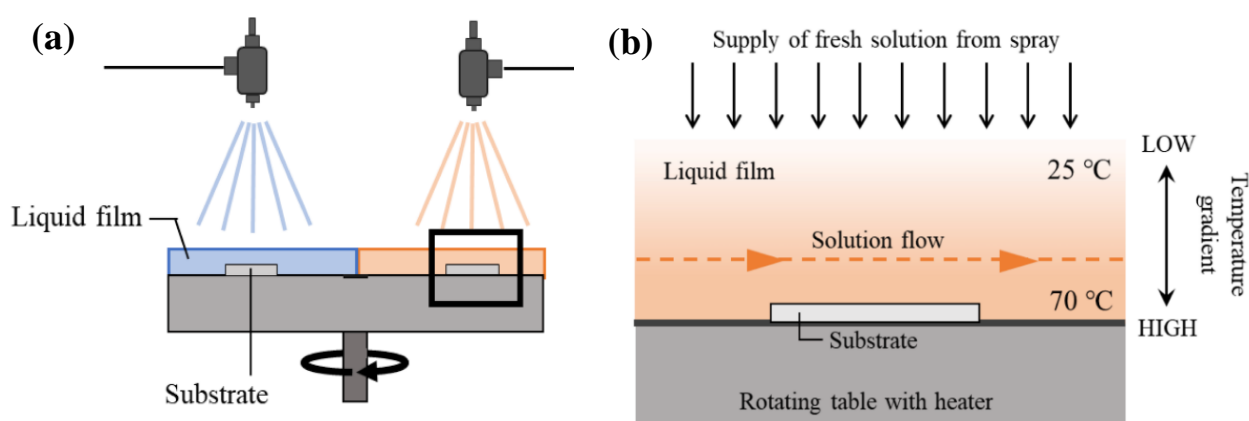
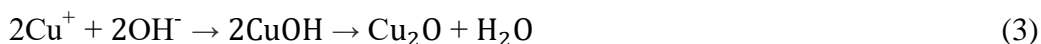


Figure 2.6 (a) Schematic illustrations of liquid film formed during film fabrication and **(b)** temperature gradient around placed in the liquid film.

In this chapter, three kinds of reaction solution were prepared using the NaOH solution, the NH_3 aq. solution, and their mixture. In the case of the NaOH solution, the formed Cu_2O powders in the reaction were just stuck on the substrate surface, but did not

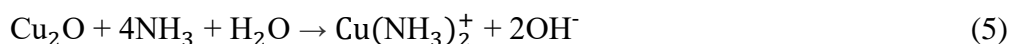
adhere strongly to the substrate. The Cu^+ ions in the source solution reacted with OH^- ions in the reaction solution to form Cu_2O powder by the following chemical reactions.



Under these conditions, the reaction in eq. (3) was too fast that the sprayed Cu^+ ions mostly precipitated as Cu_2O powders in the liquid film before reaching the substrate surface. Therefore, heterogeneous nucleation on the substrate was not achieved and the Cu_2O powders did not strongly adhere to the substrate. On the other hand, neither Cu_2O film formation nor Cu_2O powder precipitation occurred when solutions of only NH_3 were used as the reaction solution. NH_3 aq. provides NH_4^+ and OH^- as shown in eq. (4).



The sprayed Cu^+ ions from the source solution reacted with OH^- to form Cu_2O , as shown in eq. (3). However, Cu_2O easily dissolved through the formation of an ammine complex via the chemical reaction shown in eq. (5).



As a result, the Cu_2O films did not remain on the substrates.

In contrast, for the case of the mixed NaOH and NH_3 solutions, phase-pure Cu_2O films which contained no impurities, such as OH^- , amines, and ascorbic acid, could be fabricated on the substrates with good adhesion, as shown in **Figure 2.2**. **Figure 2.6 (b)** shows there is a large temperature difference between the liquid film surface and the substrate surface. Homogeneous nucleation was suppressed in the liquid film because the copper ions reacted with ammonia to form ammine complexes, as shown in eq. (5). On the other hands, the ammine complex is only decomposed near the substrate surface, and

therefore, the Cu^+ ions react with OH^- ions leading to the formation of the Cu_2O film, as shown in eq. (3).

For the fabrication of a phase-pure Cu_2O film via solution processing, it is important to precipitate it from a solution that contains only Cu^+ ions, which is free of Cu^{2+} ions. Therefore, a reducing agent is required to fabricate phase-pure Cu_2O via solution processing. Furthermore, it is necessary to prevent Cu^+ from being re-oxidized to Cu^{2+} by dissolved oxygen in the solution. The reducing agent, L-ascorbic acid, reacts with dissolved oxygen and acts as an oxidation inhibitor. The reduction potential of L-ascorbic acid depends on the pH of the solution, and the reduction rate of copper is markedly decreased at a pH value higher than 5.0. According to M. Emadi et al., an acidic environment is required for the efficient reduction of Cu^{2+} by L-ascorbic acid and the optimal pH is 2.38.¹⁰ Although an alkaline environment is required to deposit Cu_2O from the solution as shown in eq. (3), the reduction of Cu ions is insufficient and CuO and $\text{Cu}(\text{OH})_2$ impurities are easily incorporated in the growing film. Cu_2O films were fabricated by spraying the source solution at pH 2.3 and the reaction solution at pH 13 or more on the substrates fixed to the rotating table. Hence, there were two regions on the rotating table where the pH values were completely different as shown in **Figure 2.7** since the nozzle for the source and reaction solution were placed separately. In other words, the substrates were alternately immersed in the liquid film in alkaline and acidic environments. The formation of Cu_2O films were promoted in the alkaline liquid film, but the reduction rate of copper by L-ascorbic acid was significantly decreased at high pH. However, ascorbic acid can recover its reduction ability and the oxidation of Cu^+ was suppressed by rotating the table and immersing the substrate in the acidic liquid film.

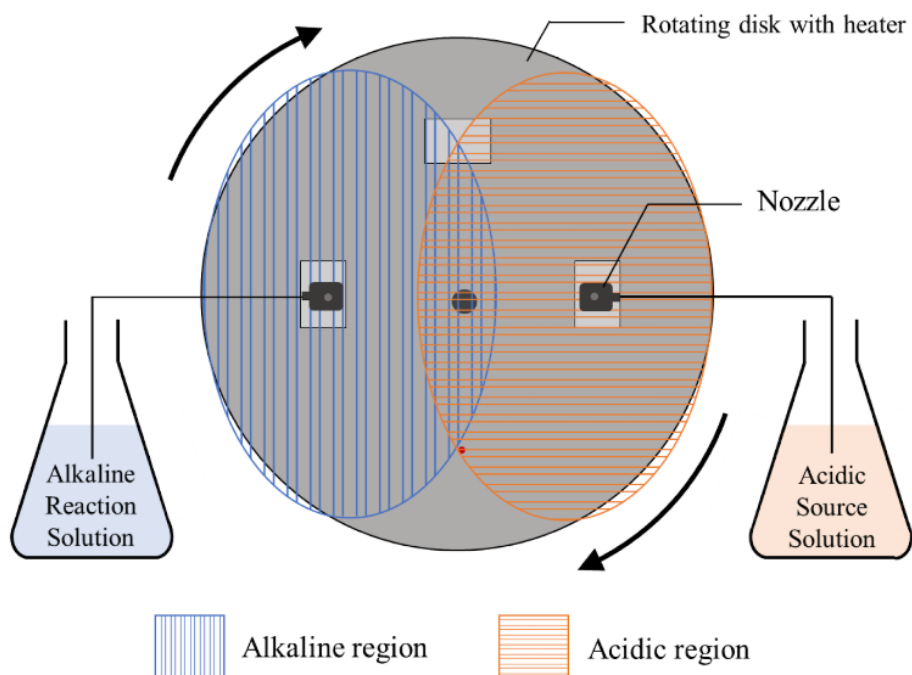


Figure 2.7 Schematic illustrations of two regions with different pH on rotating disc (top view).

2.4.2 Effect of NaOH on Sample Morphology and Growth Orientation

The concentration of the mixed NaOH solution was changed from 0.2 to 0.4 M with 0.8 M NH_3 aq. to investigate the role of NaOH on film formation. The shapes of the exposed surface grains were closely related to the orientation of the films, as shown in **Figure 2.2 (a)** and **Figure 2.3**. For $S_{0.2}\text{-}A_{0.8}$ which is the [100]-oriented film, most of the exposed grains have flat planes correspond to the {100}.¹¹ On the other hand, for $S_{0.3}\text{-}A_{0.8}$ and $S_{0.4}\text{-}A_{0.8}$, four-sided pyramidal grains appeared on the surface. Their side faces could be attributed to the (111), indicating that the grains grow in the [100].¹² As shown in eq (3), the formation rate of CuOH, which is a precursor to Cu_2O , depended on the concentrations of Cu^+ ions and OH^- ions. However, it depended only on the OH^- ions concentration because the Cu^+ ions concentration was constant under our experimental conditions. Therefore, it can be concluded that the fabrication rate of Cu_2O increases

alongside the NaOH concentration, which is in good agreement with film thickness shown in **Figure 2.3**. As shown in **Figure 2.2 (a)**, $S_{0.2-A_{0.8}}$ was strongly oriented in the [100], and the relative intensity of (111) to (200) continuously increased with increasing NaOH concentration from 0.2 to 0.4 M. T. Shinagawa et al. reported that the trend for the preferred growth orientation between the $\langle 100 \rangle$ and $\langle 111 \rangle$ can be explained qualitatively by considering the fabrication rate.¹³ In the cubic cuprite structure, the polar (100) had a higher surface energy than the nonpolar (111).^{14,15} Therefore, a lower deposition rate favors the $\langle 100 \rangle$ based on a thermodynamic equilibrium control, while a higher deposition rate is under a nonequilibrium control and results in the $\langle 111 \rangle$. Since $S_{0.2-A_{0.8}}$ with a lower deposition rate was grown under conditions closest to the thermodynamic equilibrium, the growth rate along the [100] was the fastest. On the other hand, $S_{0.3-A_{0.8}}$ and $S_{0.4-A_{0.8}}$ with relatively high deposition rates were likely to expose the more energetically stable {111} at the surface, resulting in the formation of four-sided pyramidal grains.

2.4.3 Effect of NH_3 on Sample Morphology and Growth Orientation

The NH_3 aq. concentration in the mixed solution was then varied from 0.2 to 1.2 M with 0.4 M NaOH to investigate the role of NH_3 on the film formation. The surface morphology of $S_{0.4-A_{0.2}}$ and $S_{0.4-A_{0.4}}$ contained both plane-triangular grains which grow in the [111] and four-sided pyramidal grains which grew in the [100].¹³ On the other hand, $S_{0.4-A_{1.2}}$ was composed of relatively corner-less and rounded grains, and it did not contain triangular grains that are relevant to the (111). NH_3 aq. dissolves Cu_2O as shown in eq. (5), so it stands to reason that the growth rate increases as the NH_3 concentration is decreased. Therefore, as we have indicated above, the differences in the orientation of the films can be explained by the differences in the growth rate. However, the grain size and

the film thickness decreased with lower NH_3 aq. concentrations, as shown in **Figure 2.4**. As previously described, for the mixed NaOH and NH_3 aq. solutions, the copper ions form an ammine complex with ammonia. This prevented copper ions from precipitating as Cu_2O particles in the liquid film before reaching the substrate surface. However, for the case of $\text{S}_{0.4}\text{-A}_{0.2}$ and $\text{S}_{0.4}\text{-A}_{0.4}$, because the NH_3 aq. concentration was too low to completely suppress the precipitation of Cu_2O particles, a part of the copper ions that should originally have been used for film fabrication precipitated as Cu_2O particles, and these particles flowed out of the liquid film via the centrifugal force. Therefore, the grain size and film thickness of $\text{S}_{0.4}\text{-A}_{0.2}$ and $\text{S}_{0.4}\text{-A}_{0.4}$ were smaller than those of $\text{S}_{0.4}\text{-A}_{1.2}$, although the lower ammonia concentration tended to cause a higher fabrication rate for the film. The films prepared with a high NH_3 aq. concentration had fewer nucleation sites but larger submicron grain sizes. NH_3 dissolves Cu_2O as shown in eq. (5), and dissolution and reprecipitation occur more actively on the film surface when the Cu_2O films were fabricated from a reaction solution at a higher NH_3 aq. concentration. Therefore, the increase in particle size was due to Ostwald ripening, where small crystals are dissolved and then reprecipitated on large crystals.¹⁶

2.4.4 Electrical properties of Cu_2O Films via Spin-spray method

The electrical resistivity of the all samples was in the range of $10^2 \Omega\cdot\text{cm}$ with 4-point probe method. It was too high to measure the carrier density and the mobility of samples by hole effect measurement. In general, the films with few impurities consisting of large particles exhibit high electrical conductivity due to their low grain boundary resistance. Although $\text{S}_{0.4}\text{-A}_{1.2}$ was a phase-pure Cu_2O film composed of large particles compared to other reports,¹⁷⁻¹⁹ it showed high electrical resistivity of $2.43 \times 10^2 \Omega\cdot\text{cm}$.

Cu₂O is widely known to be a native p-type semiconductor and its p-type conductivity originates from a thermodynamic preference for Cu vacancies in the lattice, which in turn generate robust electron acceptors at the valence-band top.²⁰ Therefore, the high electrical resistivity of Cu₂O films via spin-spray method indicated the small amount of Cu vacancies in the films. These results showed that the spin-spray method enable to fabricate highly crystalline Cu₂O films with few defects.

Conclusion

Phase-pure Cu₂O films, 2-3 μm in thickness, were fabricated on glass substrates in a very short time of 10 min at low temperature of 70 °C via the spin-spray technique using a mixed NaOH and NH₃ aq. solution as the reaction solution. NaOH played the role to increase the nucleation density and higher pH in the reaction site faster deposition rate. On the other hand, NH₃ aq. contributed to homogeneous nucleation and grain growth via Ostwald ripening accompanied by dissolution and precipitation. Their concentration ratios changed the orientation and size of the grains in the films. Cu₂O films fabricated from the reaction solution with an NaOH concentration higher than that of the NH₃ aq. was strongly oriented in the [111]. On the other hand, films fabricated from solutions with a higher concentration of NH₃ aq. than of NaOH was preferentially oriented in the [100]. The film prepared from the reaction solution of 0.4 M NaOH and 0.2 M NH₃ aq., S_{0.4}-A_{0.2}, was composed of nanoparticles with a size of ~100-600 nm. The Cu₂O film had a rough surface with a high specific surface area and a considerably large band gap of 2.31 eV. The film prepared from the reaction solution with 0.2 M NaOH and 0.8 M NH₃ aq., S_{0.2}-A_{0.8}, had a planar surface with relatively low light scattering and higher transparency than other samples.

References

- [1] S. Sun, X. Zhang, Q. Yang, S. Liang, X. Zhang, Z. Yang, *Prog. Mater. Sci.* 96 (2018) 111–173.
- [2] T. Minami, Y. Nishi, T. Miyata, J.I. Nomoto, *Appl. Phys. Express* 4 (2011) 062301.
- [3] M. Hari Prasad Reddy, P. Narayana Reddy, S. Uthanna, *Indian J. Pure Appl. Phys.* 48 (2010) 420–424.
- [4] J. Cui, U. J. Gibson, *J. Phys. Chem. C.* 114 (2010) 6408–6412.
- [5] H. Xu, J.K. Dong, C. Chen, *Mater. Chem. Phys.* 143 (2014) 713–719.
- [6] R.K. Swarnkar, S.C. Singh, R. Gopal, *Bull. Mater. Sci.* 34 (2011) 1363–1369.
- [7] J.Y. Chen, P.J. Zhou, J.L. Li, S.Q. Li, *Carbohydr. Polym.* 67 (2007) 623–629.
- [8] A.H.B. Dourado, A.G.M. da Silva, F.A.C. Pastroián, R.L. Munhos, A.P. de Lima Batista, A.G.S. de Oliveira-Filho, J. Quiroz, D.C. de Oliveira, P.H.C. Camargo, S.I. Córdoba de Torresi, *J. Catal.* 375 (2019) 95–103.
- [9] S. Poulston, P.M. Parlett, P. Stone, M. Bowker, *Surface and Interface Analysis.* 24 (1996) 811.
- [10] M. Emadi, M. A. Zare, O. Moradlou, M. Iranpour, *J. Phys. Chem. Electrochem.* 22 (2014) 87–92.
- [11] W. Wu, K. Feng, B. Shan, N. Zhang, *Electrochim. Acta* 176 (2015) 59–64.
- [12] L.C. Wang, N.R. de Tacconi, C.R. Chenthamarakshan, K. Rajeshwar, M. Tao, *Thin Solid Films.* 515 (2007) 3090–3095.
- [13] T. Shinagawa, Y. Ida, K. Mizuno, S. Watase, M. Watanabe, M. Inaba, A. Tasaka, M. Izaki, *Cryst. Growth Des.* 13 (2013) 52–58.
- [14] P.M. Jones, J.A. May, J.B. Reitz, E. I. Solomon, *J. Am. Chem. Soc.* 120 (1998) 1506–1516.
- [15] A. Soon, M. Todorova, B. Delley, C. Stampfl, *Phys. Rev. B* 75 (2007) 125420.
- [16] O. Reyes-Vallejo, J. Escorcia-García, P.J. Sebastian, *Mater. Sci. Semicond. Process.* 138 (2022) 106242.
- [17] S. Bijani, L. Martinez, M. Gabás, E.A. Dalchiele, J.R. Ramos-Barrado. *Phys. Chem. C.* 113 (2009) 19482–19487.
- [18] M.J. Siegfried, K.-S. Choi, *Chem. Int. Ed.* 44 (2005) 3218–3223.
- [19] A. E. Kasmi, Z. Tian, H. Vieker, A. Beyer, T. Chafik, *Applied Catalysis B: Environmental.* 186 (2016) 10–18.
- [20] A. Gloystein, N. Nilius, *Phys. Status Solidi Basic Res.* 258 (2021).

Chapter 3 CuO Nanostructures Fabricated by Spin-spray Method

3.1 Introduction

Nanostructured CuO films are often used in gas-sensing devices because of its high surface activity and oxygen adsorption capability.^{1,2} In the past decades, various physical and chemical methods have been used to fabricate CuO nanostructures such as nanowires, nanosheets and nanoparticles.³⁻⁵ However, these methods may require a vacuum system and high fabrication temperatures in addition to heat-resistant and/or conductive substrates, leading to certain disadvantages, such as high environmental impacts, significant expense or limited substrate ranges. On the other hands, solution-based processes, including chemical bath deposition, successive ionic adsorption and reaction (SILAR) and chemical bath deposition (CBD) have significant advantages over other techniques by allowing film fabrication at temperatures below 100°C under atmospheric pressure.^{6,7} However, it is difficult to fabricate the CuO nanostructures on the seed-free glass substrates with good adhesion by the conventional solution-based processes.

To overcome the problems of these solution processes and to obtain good adhesion between the film and substrate, the spin-spray method has been applied to fabricate CuO nanostructures on the seed-free glass substrate in this chapter. In addition, two types of the CuO nanostructures were fabricated by using the appropriate complexing agent in the source solution. We discuss the formation mechanism of the CuO nanostructure via spin-spray reactions in terms of the complexing agents and the reaction field with pH gradient.

3.2 Experiment

3.2.1 Substrate and chemicals

Borosilicate glass substrates were purchased from MATUSNAMI GLASS Ind., Ltd., Japan. Copper(II) sulfate pentahydrate ($\text{CuSO}_4 \cdot 5\text{H}_2\text{O}$, 99.0%), ethylenediamine ($\text{C}_2\text{H}_8\text{N}_2$, 99.0%), trisodium citrate ($\text{C}_6\text{H}_5\text{Na}_3\text{O}_7$, 99.0%), sodium hydroxide (NaOH , 99.0%), and ammonia (NH_3 aq. 28 w%) were all purchased from FUJIFILM Wako Pure Chemical Corporation, Ltd., Japan. All of the chemicals were used as received without further purification. Deionized water was used for all of the experiments.

3.2.2 Fabrication of CuO nanostructures by spin-spray method

CuO films were fabricated on borosilicate glass ($30 \times 40 \times 0.20$ mm) and via the spin-spray method. Before fabrication, the substrates were ultrasonically cleaned in deionized water for 10 min, and were then treated using a ultraviolet-ozone cleaner (BioForce Nanosciences, Inc., USA, UV Ozone Cleaner ProCleaner™ Plus) for 10 min to increase the surface hydrophilicity. The reaction and source solutions were prepared by dissolving the precursor materials in 0.7 L of deionized water. The reaction solution was prepared using NaOH solution at pH 11 or 13. Two source solutions were prepared by dissolving 1.2 M NH_3 aq., 0.06 M $\text{C}_2\text{H}_8\text{N}_2$ or 0.06 M $\text{C}_6\text{H}_5\text{Na}_3\text{O}_7$ in 0.04 M $\text{CuSO}_4 \cdot 5\text{H}_2\text{O}$ solution. The reaction and source solutions were pumped to their respective nozzles at a flow rate of 0.05 L/min and sprayed onto the substrate on the rotating table (150 rpm) with N_2 carrier gas. The rotating table was heated at 90 °C during fabrication and the deposition time was 10 min. Samples fabricated on Glass substrate using $\text{C}_2\text{H}_8\text{N}_2$ (EDA) and $\text{C}_6\text{H}_5\text{Na}_3\text{O}_7$ (Cit) are referred to as CuO-Glass-EDA and CuO-Glass-

Cit, respectively. After fabrication, all samples were ultrasonically cleaned in deionized water to remove any surface contaminants.

3.2.3 Characterization

The crystallinity and microstructure of the samples were analyzed by X-ray diffraction (XRD, BRUKER Co., USA, D8 FOCUS/TXS) at a scan angle (2θ) range of 20–80°. X-rays were generated using a Cu- K_{α} source at 35 kV and 50 mA at a wavelength of 0.15418 nm. The surface morphologies of the samples were observed by field emission scanning electron microscopy (FESEM, HITACHI, Japan, S-4700) in secondary electron mode at a working voltage of 8 kV. After drying the samples at 60 °C for 12 h, X-ray photoelectron spectroscopy (XPS, PhysicalElectronics, Inc., USA, PHI 5000) was used to investigate the chemical states. All XPS spectra were fitted using a numerical simulation program (XPSPEAK 41) with a Shirley background and a Lorentzian/Gaussian line shape.

3.3 Results

3.3.1 Characteristics of Nanostructured CuO Films

The spin-spray method enabled the one-step fabrication of CuO films using $C_2H_8N_2$ (EDA) and $C_6H_5Na_3O_7$ (Cit) on the glass substrates at low temperature ($90^\circ C$) and short time (10 min). The two samples were referred as CuO-Glass-EDA and CuO-Glass-Cit, respectively. **Figure 3.1 (a) and (b)** shows that CuO-Glass-EDA and CuO-Glass-Cit were deposited uniformly on the glass substrates and appeared blacks and dark gray in colors, respectively. These films exhibited strong adhesion to the substrate without peeling off, even after ultrasonication at 45 kHz of 200 W in deionized water for 10 min, as shown in **Figure 3.1 (a) and (b)**. XRD patterns of the samples showed peaks characteristic of the monoclinic phase of CuO with good accordance to the ICDD data (JCPDS 48-1548), as shown in **Figure 3.1 (c)**. No impurity peaks from $Cu(OH)_2$, Cu_2O , ethylenediamine or trisodium citrate were observed.

Figure 3.2 shows the ATR-FTIR spectra of CuO-Glass-EDA, CuO-Glass-Cit and the glass substrate. The band at around 600 cm^{-1} in the sample spectra is attributed to the vibrational mode of Cu-O in CuO.⁸ In the spectra of CuO-Glass-Cit, two intense bands are observed at 3500 cm^{-1} and at 1635 cm^{-1} , were attributed to the O-H stretching and O-H-O scissors-bending.⁹ The band at $2600\text{--}3600\text{ cm}^{-1}$ is very broad because of hydrogen-bridging between the water molecules.¹⁰ These results indicated that adsorbed water was present on the surface of CuO-Glass-Cit.

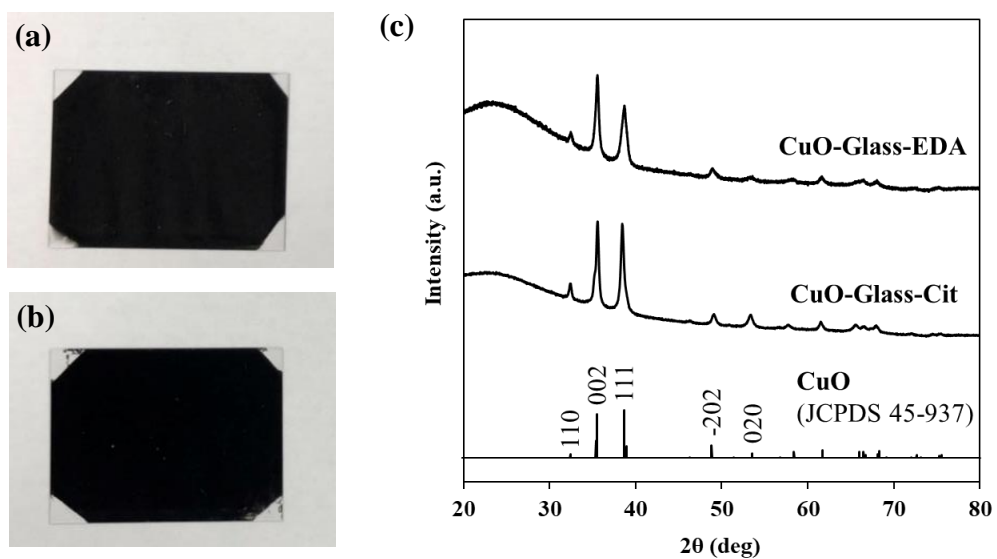


Figure 3.1 Digital photos of (a) CuO-Glass-EDA and (b) CuO-Glass-Cit (c) XRD patterns of CuO-Glass-NH, CuO-Glass-EDA and CuO-Glass-Cit

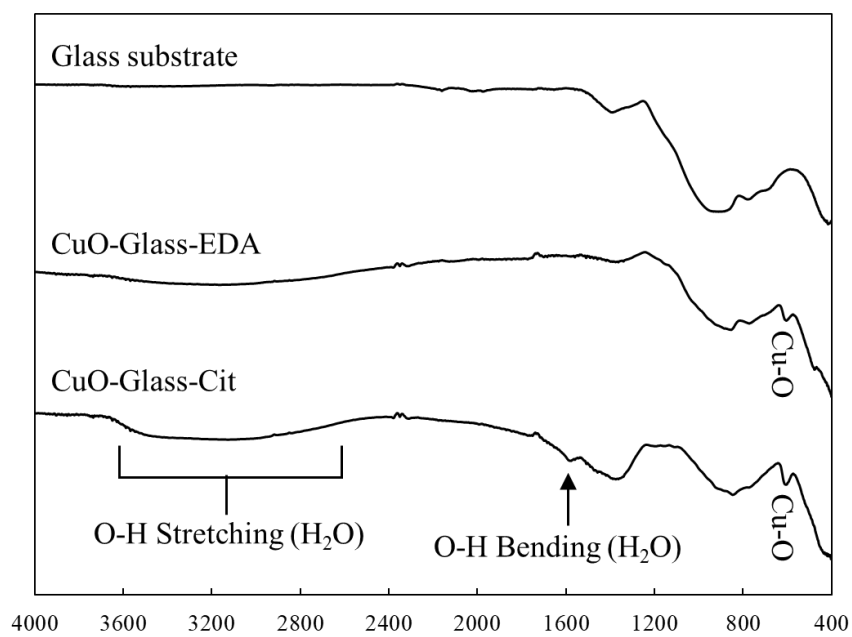


Figure 3.2 ATR-FTIR spectra of the CuO-Glass-EDA, CuO-Glass-Cit and glass substrate.

3.3.1 Morphology of Nanostructured CuO Films

Figure 3.3 shows surface and cross-sectional FESEM images of CuO-Glass-EDA and CuO-Glass-Cit. **Figure 3.3 (a) and (b)** show that the surface of CuO-Glass-EDA was composed of nanosheets having a high aspect ratio, i.e. 2.23 μm in the lateral direction and 20 nm in thickness. These nanosheets, not aggregated but sparsely located, grew vertically on the substrate forming a grass-like nanosheet array, as shown in **Figure 3.3 (c)**. CuO-Glass-Cit was composed of nanosheet clusters and the substrate surface was fully covered with these clusters to forming a carpet-like morphology, as shown in **Figure 3.3 (d)**. The magnified image in **Figure 3.3 (e)** shows that tiny multilayered nanosheets, 135 nm in lateral direction and 23 nm in thickness, accumulated with their sheet surfaces orientated parallel to the substrate. These nanosheet clusters aggregated to each other to form a dense film structure of 1.05 μm in the thickness, as shown in **Figure 3.3 (f)**.

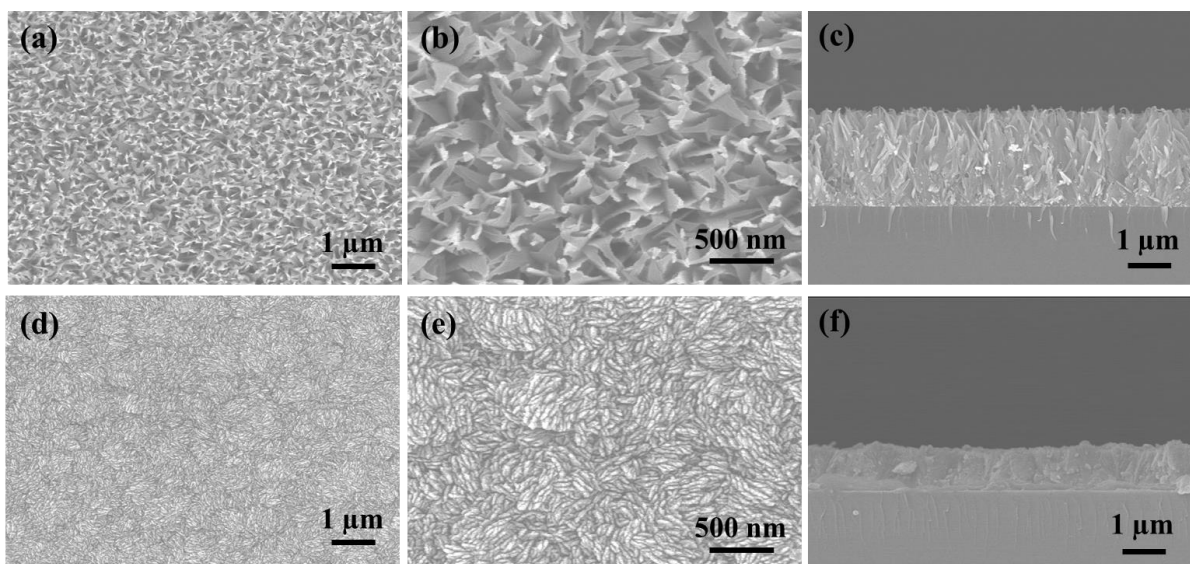


Figure 3.3 Surface and cross-sectional FESEM images of (a, b) CuO-Glass-EDA and (c, d) CuO-Glass-Cit.

3.3.2 Optical Properties of Nanostructured CuO Films

The optical band gaps of the CuO-Glass-EDA and CuO-Glass-Cit specimens were calculated from optical diffuse reflectance data. These band gaps were determined on the basis of the relationship between the absorption coefficient (α) calculated by K-M transform and the photon energy ($h\nu$), written as

$$\alpha h\nu = A(E_g - h\nu)^n, \quad (1)$$

where E_g is the band gap energy, A is a constant and n has a value of $1/2$ or 2 for allowed direct and indirect transitions, respectively. **Figure 3.4 (a)** and **(b)** presents plots of $(\alpha h\nu)^2$ versus $h\nu$ for the CuO-Glass-EDA and CuO-Glass-Cit, from which the optical band gaps were obtained from the intercepts of extrapolated straight lines with the photon energy axis. On this basis, CuO-Glass-EDA and CuO-Glass-Cit specimens were found to possess direct band gaps of 1.61 and 1.52 eV, respectively.

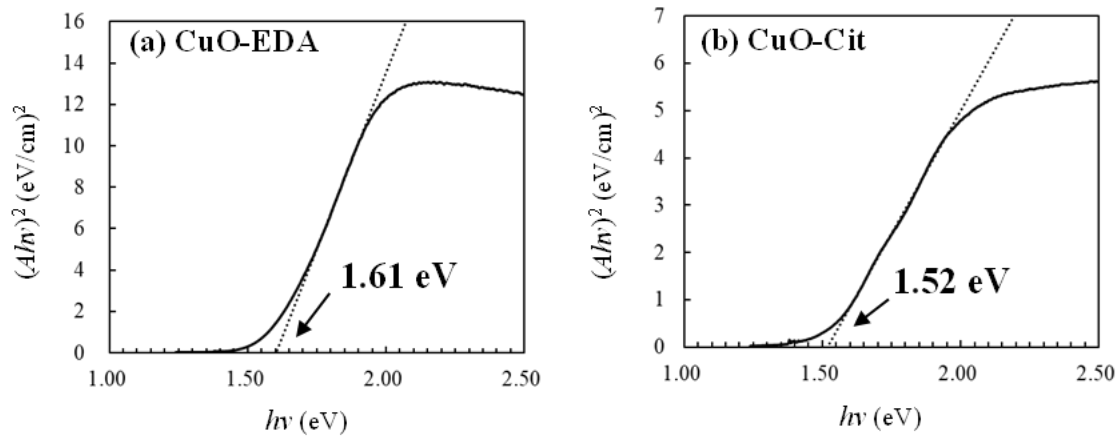
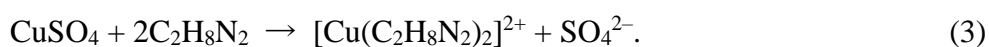


Figure 3.4 Tauc plots for the (a) CuO-Glass-EDA and (b) CuO-Glass- Cit.

3.4 Discussion

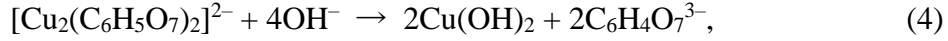
3.4.1 Formation Mechanism of CuO dense film and nanosheet array

Figure 3.3 shows that sheet-like CuO nanostructures were fabricated on glass substrates with good adhesion via the spin-spray method. The formation of the CuO nanosheets by the spin-spray method can be explained as follows. When the source solution was prepared by dissolving the only $\text{CuSO}_4 \cdot 5\text{H}_2\text{O}$ in deionized water without organic compounds, no films were formed on the substrate by the spin-spray method. Therefore, the organic compounds such as ethylenediamine and trisodium citrate were important to fabricate CuO films. Cu^{2+} in the source solutions for CuO-Cit and CuO-EDA formed complexes according to:



The source solutions for CuO-Glass-Cit and CuO-Glass-EDA were weakly acidic with pH values of 4.56 and 6.06, respectively, while the reaction solution was strongly alkaline NaOH with a pH of 13. In the spin-spray method, the sprayed reaction and source solutions mixed and reacted to form functional oxide films.¹¹ The sprayed weakly acidic and strongly alkaline solutions were distributed on the rotating stage in areas (i) and (iii), forming the weakly alkaline areas (ii-a) and (ii-b) between (i) and (iii), as shown in **Figure 3.5**. This means there was a pH difference between areas (i) and (iii) which served as the reaction field for the film, as shown in **Figure 3.5**. The rotating substrate started from area (i) and arrived at area (iii) after passing through area (ii-a) which had a large pH gradient. In area (ii-a), copper complexes such as $[\text{Cu}_2(\text{C}_6\text{H}_5\text{O}_7)_2]^{2-}$ and $[\text{Cu}(\text{C}_2\text{H}_8\text{N}_2)_2]^{2+}$

transformed to $\text{Cu}(\text{OH})_2$ nuclei on the substrate because of the large amount of OH^- present, according to:^{12,13}



$\text{Cu}(\text{OH})_2$ nuclei formed on the substrate in area (ii-a) and transformed to $\text{Cu}(\text{OH})_4^{2-}$ because of the excess OH^- in area (iii), as expressed by:¹⁴



Cudennec and Lecerf reported that $\text{Cu}(\text{OH})_4^{2-}$ rapidly transformed into CuO even at temperatures below 100 °C with the loss of two OH^- and one water molecule, according to:¹⁵



Excessive alkalinity promoted the reaction in equation (6) but suppressed the transformation from $\text{Cu}(\text{OH})_4^{2-}$ to CuO resulting in the formation of $\text{Cu}(\text{OH})_2$, as shown in equations (6) and (7).¹⁶ This is why it is difficult to rapidly deposit CuO by conventional solution hydrothermal and chemical bath deposition methods in which Cu^{2+} and OH^- coexist in the reaction field for a long time without a pH gradient. In the spin-spray method, the separated Cu^{2+} and OH^- were mixed on the rotating table to create a reaction field with a pH gradient, as shown in **Figure 3.5**. The substrate arrived back at the weakly acidic area (i) after passing through area (ii-b). CuO was rapidly formed on the substrate by the condensation reaction of $\text{Cu}(\text{OH})_4^{2-}$ complex anions linked by hydrogen bonds, according to:



The spin-spray method enabled the reactions in equations (6) and (8) to occur efficiently in areas (iii) and (i), respectively. Unreacted species and/or unnecessary nucleated nano hydroxides were continuously removed from the reaction field, and fresh reaction and source solutions were constantly supplied to the reaction field. Pure CuO films containing no impurities such as $\text{Cu}(\text{OH})_2$ were therefore obtained.

The reaction in equation (6) suggested that the CuO morphology depended on the manner of the linkage of hydrogen bonds between $\text{Cu}(\text{OH})_4^{2-}$ complex anions. $\text{Cu}(\text{OH})_4^{2-}$ is a square planer complex anion. Liao et al. reported that a high molar ratio of NaOH to a complexing agent such as $\text{C}_2\text{H}_8\text{N}_2$ or $\text{C}_6\text{H}_8\text{O}_7$ in area (ii-b) led to hydrogen bonding along the [010], resulting in tiny two dimensional CuO nanoflakes.¹⁷ The high alkalinity environment in area (iii) promoted the reaction in equation (6) and also promoted the back transformation of CuO to $\text{Cu}(\text{OH})_4^{2-}$, as shown in equation (7).¹⁶ Therefore, CuO repeatedly dissolved and precipitated on the substrate fixed on the rotating table. Finally, the formed tiny nanoflakes served as seeds to deposit the aggregated and non-aggregated CuO nanosheets through Ostwald ripening.¹⁷ The CuO nanosheet obtained by the above process was reported to grow in the [010] with its top surface being the (001).¹⁶ **Figure 3.3** shows that CuO-Glass-Cit was a dense film in which CuO nanosheet clusters accumulated with their (001) surfaces orientated parallel to each other and perpendicular to the substrate plane, and a large number of (111) were exposed on the CuO-Glass-Cit surface. This perpendicular alignment of nanosheets was one of the reasons that CuO-Glass-Cit showed a high 111 peak intensity in the XRD pattern in **Figure 3.1 (c)**.

Figure 3.3 shows that the surface morphology of the samples depended on the complexing agent that was added. Dubal et al. reported that negatively charged OH^- or OH groups selectively adsorbed to the CuO nanosheet surface, and that this caused nanosheet aggregation by the electrostatic attraction between OH^- and Cu^{2+} of adjacent nanosheets.¹⁸ CuO-Glass-Cit was a dense film composed of nanosheets because the OH groups of the added citric acid promoted aggregation. The functional groups of the added ethylenediamine were amino groups, so CuO-Glass-EDA had no OH groups. In addition, CuO nanosheets formed in the weakly acid area (i). There were almost no OH^- or OH groups to promote aggregation between the nanosheets in CuO-Glass-EDA. This led to the sparsely located nanosheets grown vertically on the substrate, as shown in **Figure 3.3**.

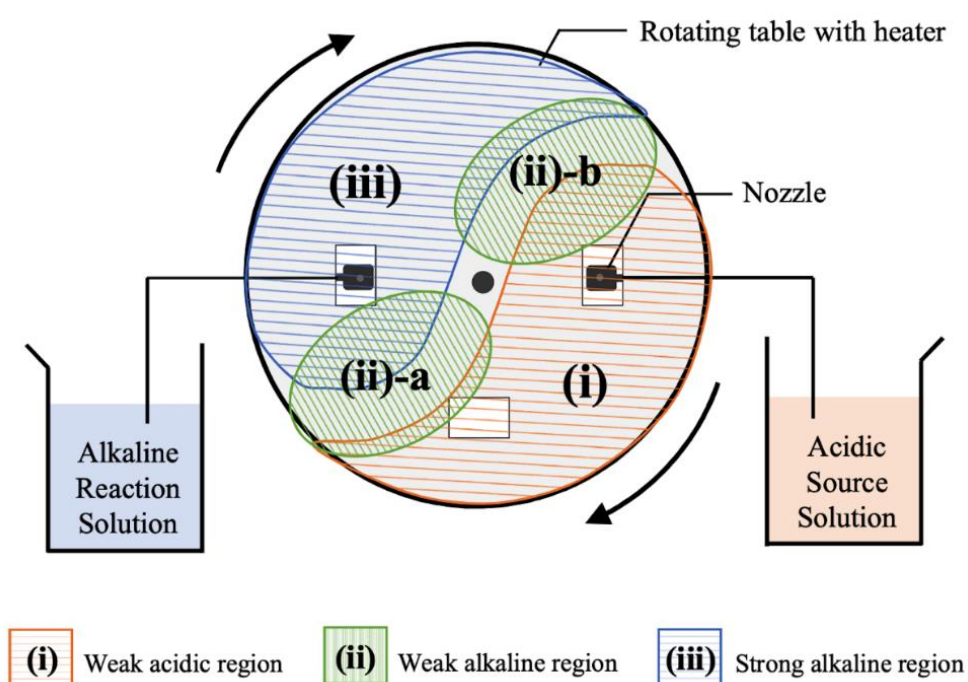


Figure 3.5 Schematic illustrations of three areas with different pH values on the rotating table.

3.4.2 Surface properties of CuO dense film

The result in **Figure 3.2** indicated that adsorbed water was present on the surface of CuO-Glass-Cit. Water molecules were strongly adsorbed on the CuO-Cit surface, despite the sample having been dried at 60 °C for 12 h before ATR-FTIR measurement. A large number of (111) were exposed on the CuO-Glass-Cit surface, as described in **section 3.4.1**. Yu et al. reported that water molecules adsorbed on the CuO (111) dissociated into H and OH species and that the surface was covered with OH groups. Water molecules were chemisorbed by OH groups on the CuO (111) and could not desorb even at high temperature under vacuum conditions, indicating that the CuO-Glass-Cit surface was in hydrated form.^{18,19}

3.4.3 Optical band gaps of CuO dense film and nanosheet array

The data in **Figure 3.4** also indicated a blue shift in the optical band gaps between the CuO dense film and non-aggregated CuO nanosheet. Such a blue shift in nanostructured CuO films has been reported in many studies, where it has been argued that the observed shift was due to the quantum confinement effects. If the grain size is smaller than the exciton Bohr radius (up to 28.7 nm for CuO), the quantum confinement effect will play an important role in the blue shift of the band gap.²⁰ As shown in **Figure 3.3 (b) and (c)**, the nanosheet thickness of CuO-Glass-EDA is 20 nm, which was smaller than the Bohr radius of CuO. **Figure 3.3 (e) and (f)** indicated that the nanosheets composing CuO-Glass-Cit aggregated to each other to form a dense film structure of 1.05 μm in the thickness, which was larger than the Bohr radius of CuO.^{21,22} Therefore, the blue shift in band gaps of the CuO-Glass-EDA and CuO-Glass-Cit was due to the quantum confinement effect.^{23,24}

Conclusion

Sheet-like CuO nanostructures were fabricated on glass substrates at low temperature of 90 °C in a short time of 10 min via the spin-spray method using the appropriate complexing agent. These CuO nanostructures exhibited the good adhesion with glass substrates. The sample fabricated using citric acid as the complexing agent was composed of nanosheet clusters and the substrate surface was fully covered with these clusters to forming a carpet-like morphology. These nanosheet clusters aggregated to each other to form a dense film structure in the thickness direction. On the other hands, the sample prepared using EDA as the complexing agent was composed of nanosheets having a high aspect ratio, i.e. 2 μm in the lateral direction and 20 nm in thickness. These nanosheets, not aggregated but sparsely located, grew vertically on the substrate forming a grass-like nanosheet array.

References

- [1] B. Balamurugan, B.R. Mehta, *Thin Solid Films* 396 (2001) 90-96.
- [2] B.J. Hansen, N. Kouklin, G.H. Lu, I.K. Lin, J.H. Chen, X. Zhang, *Phys. Chem. C*, 114 (2010) 2440-2447.
- [3] F. Mumm, P. Sikorski, *Nanotechnology* 22 (2011) 105605.
- [4] F. Li, X. Liu, Q. Zhang, T. Kong, H. Jin, *Cryst. Res. Technol.* 47 (2012) 1140-1147.
- [5] M. Outokesh, M. Hosseinpour, S.J. Ahmadi, T. Mousavand, S. Sadjadi, W. Soltanian, *Ind. Eng. Chem. Res.* 50 (2011) 3540-3554.
- [6] J. Sultana, S. Paul, A. Karmakar, R. Yi, G.K. Dalapati, S. Chattopadhyay, *Appl. Surf. Sci.* 418 (2017) 380–387.
- [7] Y. Akaltun, *Thin Solid Films*. 594 (2015) 30–34.
- [8] C. Yang, X. Su, J. Wang, X. Cao, S. Wang, L. Zhang, *Sens. Act. B* 185(2013)159-165
- [9] A. Umar, A.A. Alshahrani, H. Algarni, R.Kumar, *Sens. Act. B* 250(2017)24-31
- [10] L. Chen, L. Li, G. Li, *J. Alloy Comp.* 464(2008)532-536
- [11] R. Nitta, Y. Kubota, T. Kishi, T. Yano, N. Matsushita, *Mater. Chem. Phys.* 243 (2020) 122442.
- [12] H. Xiao, S. Fu, L. Zhu, Y. Li, G. Yang, *Eur. J. Inorg. Chem.* (2007) 1996-1976
- [13] N.F.A. Neto, P.M. Oliveira, R.M. Nascimento, C.A. Paskocimas, M.R.D.Bomio, F.V. Motta, *Ceram. Int.* 45 (2019) 651-658.
- [14] C. Yang, F. Xiao, J. Wang, X. Su, *Sens. Actuators B Chem.* 207 (2015) 177-185.
- [15] Y. Cudennec, A. Lecerf, *Solid State Sci.* 5 (2003) 1471-1474.
- [16] Y. Zhao, J. Zhao, Y. Li, D. Ma, S. Hou, L. Li, X. Hao, Z. Wang, *Nanotechnology* 22 (2011) 115604.
- [17] A.Z. Liao, W. Zhu, J. Chen, X. Zhang, C. Wang, *J. Alloys Compd.* 609 (2014) 253-261.
- [18] D.P. Dubal, G.S. Gund, R. Holze, H.S. Jadhav, C.D. Lokhande, C. Park, *Dalton Trans.* 42 (2013) 6459.
- [19] X. Yu, X. Zhang, H. Wang, G. Feng, *Appl. Surf. Sci.* 425 (2017) 803-810.
- [20] J. Yang, W. Yin, B. Zhou, A. Cui, L. Xu, D. Zhang, W. Li, Z. Hu, J. Chu, *J. Phys. Chem. C*. 123 (2019) 27165–27171.
- [21] J. Yang, W. Yin, B. Zhou, A. Cui, L. Xu, D. Zhang, W. Li, Z. Hu, J. Chu, *J. Phys. Chem. C*. 123 (2019) 27165–27171.

- [22] Q. Zhang, K. Zhang, D. Xu, G. Yang, H. Huang, F. Nie, C. Liu, S. Yang, *Prog. Mater. Sci.* 60 (2014) 208–337.
- [23] S. Rehman, A. Mumtaz, S.K. Hasanain, *J. Nanoparticle Res.* 13 (2011) 2497–2507.
- [24] P. Mallick, S. Sahu, Structure, Microstructure and Optical Absorption Analysis of CuO Nanoparticles Synthesized by Sol-Gel Route, *Nanosci. Nanotechnol.* 2 (2012) 71–74.

Chapter 4 CuO Thin Film Fabricated by Mist Spin Spray Method

4.1 Introduction

CuO thin films have been synthesized using many physical and chemical processes, such as radio frequency magnetron sputtering, pulsed laser deposition, chemical spray pyrolysis, and electrodeposition.¹ However, these methods may require a vacuum system and high fabrication temperatures in addition to heat-resistant and/or conductive substrates, leading to certain disadvantages, such as high environmental impacts, significant expense or limited substrate ranges. Solution-based processes, including chemical bath deposition, successive ionic adsorption and reaction, and spin-spray methods, have significant advantages over other techniques by allowing film fabrication at temperatures below 100 °C under atmospheric pressure.²⁻⁴ However, it is difficult to produce dense, crack-free films with nanoscale thicknesses by these conventional solution techniques.

A unique solution-based process known as mist chemical vapor deposition (mist-CVD) has recently attracted attention. This technology does not require a vacuum, is highly scalable but inexpensive and can provide dense metal oxide films with nanoscale thicknesses.^{5,6} This method can be described as a CVD process based on the use of so-called mist droplets generated by the ultrasonication of a precursor solution. An ultrasonic transducer operating at a frequency of 2.4 MHz can provide droplets as small as 0.1–3 μm in diameter that are subsequently transported to the substrate via a carrier gas.⁷ However, the mist-CVD technique requires a relative high deposition temperature (over 200 °C) due to the need for thermal decomposition of the precursor.

In this chapter, a solution process termed the mist spin spray (MSS) method was developed and used to fabricate nanostructured CuO thin films with high purity. In this manner, dense and crack-free CuO thin films with nanoscale thicknesses can be fabricated on seed-free glass substrates within a short time span at a relatively low temperature through the effective utilization of chemical reactions. Therefore, it is an energy-saving and environment-friendly method compared with the mist-CVD and conventional physical and chemical processes. In addition, it is generally difficult to fabricate crystalline CuO thin films on amorphous glass substrates with good adhesion by conventional solution processes since there is no epitaxial effect between the film and the substrate. The CuO films fabricated by the MSS method strongly adhere to the glass substrate. The MSS method also allowed precise control of the film grain size, surface morphology and optical band gap by adjusting the compositions of the initial solutions.

4.2 Experiments

4.2.1 Fabrication of CuO films via the MSS method

All the chemical reagents used in this study were purchased from the FUJIFILM Wako Pure Chemical Corporation, Ltd., Japan. The borosilicate glass substrates (40×30×0.17 mm) were ultrasonically cleaned in deionized water and ethanol for 10 min and then treated using a UV-ozone apparatus (BIOFORCE Nanosciences, UV Ozone Cleaner Pro Cleaner Plus) for 10 min to increase the surface hydrophilicity. Each source solution comprised a 50 mL aqueous solution containing $\text{CuSO}_4 \cdot 5\text{H}_2\text{O}$ at a concentration of 0.04 M and NH_3 at a concentration of 1.5, 3.0 or 6.0 M. Each reaction solution was also a 50 mL aqueous solution containing NaOH at concentrations of 0.05, 0.10 or 0.50 M. The mist droplets produced from the source and reaction solutions were sprayed onto

the substrate using N₂ as the carrier gas at a flow rate of 4.0 L/min. The distance between the nozzles and the substrate was 2 mm, the film fabrication time was 30 min, the substrate was heated at 90 °C and the table was rotated at 150 rpm. The fabricated CuO films were ultrasonically cleaned in deionized water for 10 min after being prepared. Samples were fabricated using various NH₃ and NaOH levels in the source and reaction solutions, respectively, and are referred to herein using the nomenclature Ax-Sy, where x and y are the concentrations of NH₃ and NaOH, respectively.

4.2.2 Characterization and performance

The crystallinity and microstructure of each CuO film was analyzed using X-ray diffraction (XRD, BRUKER Co., D8 FOCUS/TXS) over the 2θ range of 20–80° with an X-ray wavelength of 0.15418 nm generated using a Cu-K α target operated at 45 kV and 40 mA. The surface morphologies of the films were observed via field emission scanning electron microscopy (FESEM, HITACHI, S-4700) in the secondary electron mode with a working voltage of 15 kV. The average grain size in each sample was determined statistically from the sizes of the grains observed in surface FESEM images acquired at several points on the same film. X-ray photoelectron spectroscopy (XPS, Physical Electronics, Inc., PHI 5000) using Mg-K α radiation ($h\nu = 1253.6$ eV) was used to investigate the chemical states of the specimens. The presence of impurities in each sample was assessed using attenuated total reflection Fourier transform infrared (ATR-FTIR) spectroscopy (IRPrestige-21, Shimadzu Corp., Japan). The absorbance of the films in the ultraviolet–visible (UV–vis) region was evaluated with a V-670 spectrophotometer (JASCO).

4.3 Results

4.3.1 Structural and Material Characterizations of CuO Thin Films

The MSS method enabled the one-step fabrication of CuO thin films at a low temperature of 90 °C. **Figure 4.1 (a)** presents photographic images of the as-deposited samples generated using starting solutions with various concentrations of NH₃ and NaOH. Each film was deposited uniformly on the seed-free glass substrate and was transparent with a light brown coloration. The films exhibited strong adhesion to the substrates and did not peel off even after ultrasonication in deionized water for 10 min at a frequency of 45 kHz and a power level of 200 W. The crystal structures and phase purities of the samples were investigated by XRD. The patterns obtained in **Figure 4.1 (b)** were in good agreement with the ICDD data (JCPDS 48-1548) for the monoclinic phase of CuO even though the peak intensities were not so strong for a high accelerating voltage of 45 kV and current 40 mA to X-ray tube. These results indicated that the MSS method enabled to fabricate crystalline CuO films were fabricated directly on the amorphous glass substrates without utilizing epitaxial effect even small thickness of 30 nm. No peaks related to the formation of Cu(OH)₂ or Cu₂O as impurities were observed, indicating that phase-pure CuO films were obtained using the MSS method.

The samples were further analyzed by XPS and ATR-FTIR to provide a more precise assessment of the presence of impurities. **Figure 4.2 (a)** and **(b)** show the XPS survey spectra and the XPS spectra of the Cu 2p region for A1.5-S0.1, A6.0-S0.1 and A1.5-S0.5. As shown in **Figure 4.2 (a)**, the Cu, O and C elements existed in the samples. In addition, no Na1s, N1s, and S2p peaks were identified, demonstrating that there were no impurities, such as Na, N and S ions, on the sample surfaces. **Figure 4.2 (b)** showed

that the main peaks at 933.6 and 953.4 eV were attributed to Cu₂p_{3/2} and Cu₂p_{1/2}, respectively, while the satellite peaks at 939–945 and 962.2 eV indicated the presence of Cu²⁺ ions.⁸ These results provided further evidence that the film samples comprised CuO and were in good agreement with the XRD patterns in **Figure 4.1 (b)** that did not indicate any other copper oxide and/or hydroxide phases. **Figure 4.3** shows the ATR-FTIR spectra produced by the A1.5-S0.1, A6.0-S0.1 and A1.5-S0.5 specimens. No bands were observed in the range from 3000 to 3600 cm⁻¹, which corresponds to O–H and N–H stretching region, suggesting that absorbed water, hydroxyl and amine groups were not present.^{9,10}

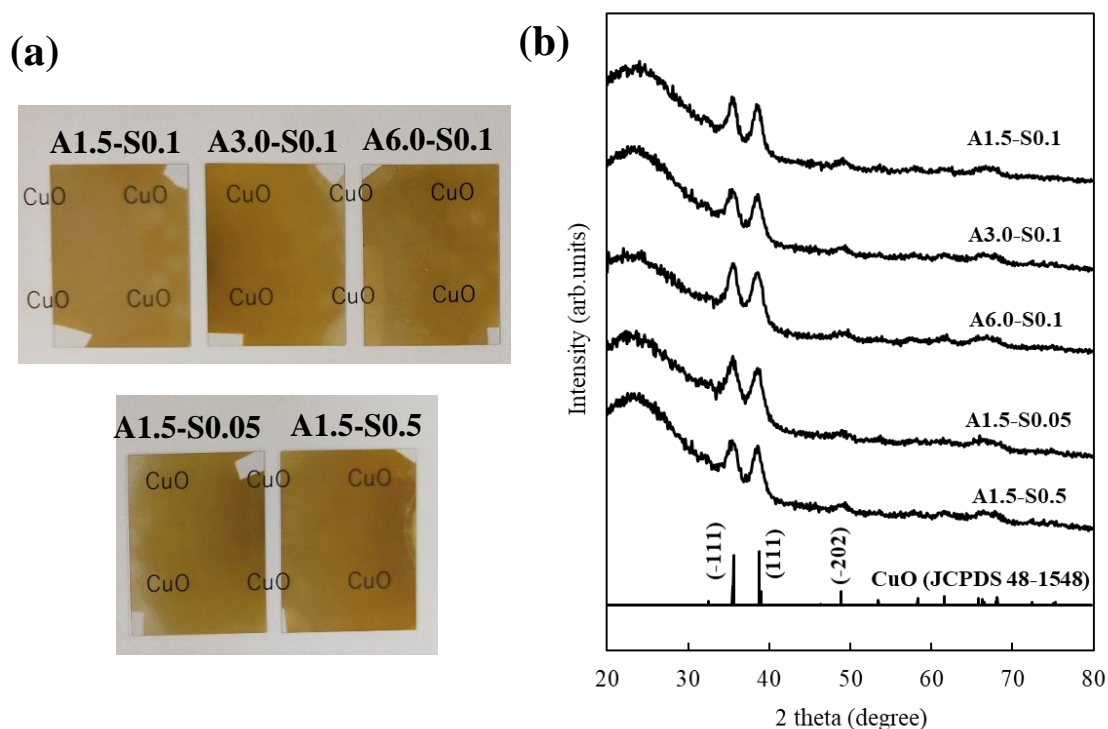


Figure 4.1 (a) Photographic images of CuO thin films fabricated on glass substrates using different concentrations of aqueous ammonia (A1.5-A6.0) in the source solution and of sodium hydroxide (S0.1-S0.5) in the reaction solution and **(b)** XRD patterns obtained from the A1.5-S0.1, A3.0-S0.1, A6.0-S0.1, A1.5-S0.05 and A1.5-S0.5 specimens.

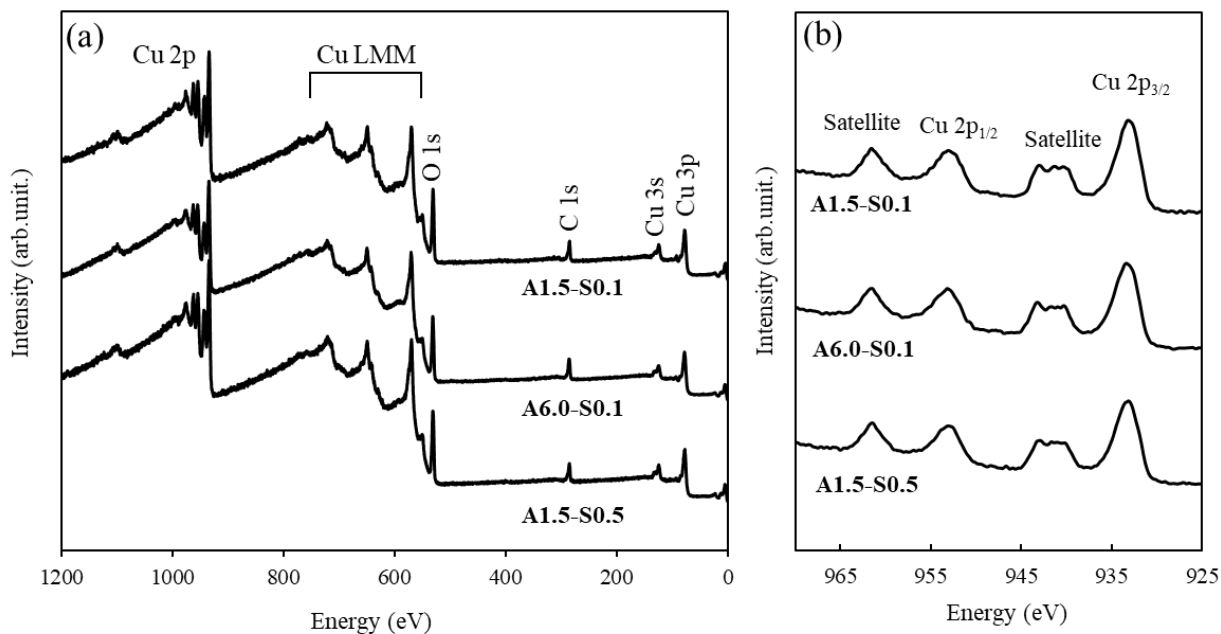


Figure 4.2 (a) XPS survey spectra and (b) XPS spectra of the Cu 2p regions for A1.5-S0.1, A6.0-S0.1 and A1.5-S0.5.

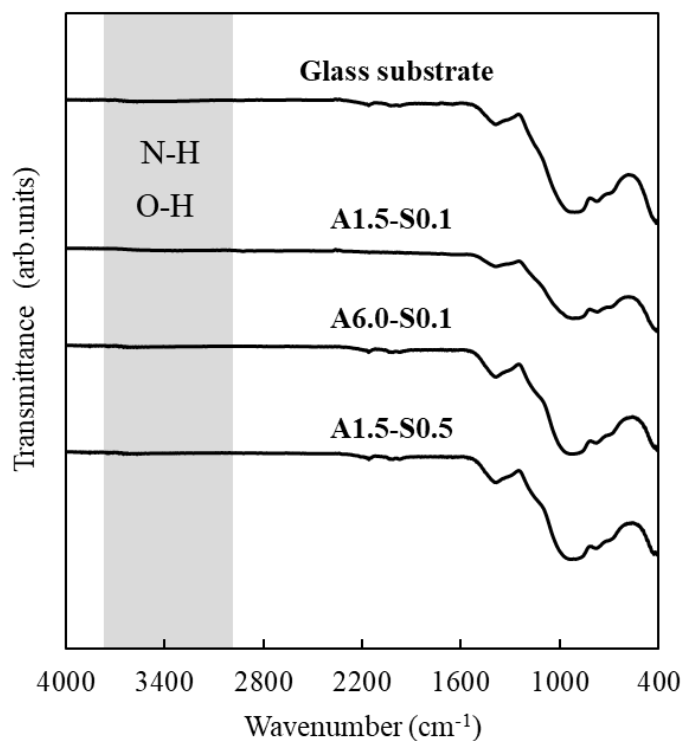


Figure 4.3 (a) ATR-FTIR spectra obtained from the glass substrate and from the A1.5-S0.1, A6.0-S0.1 and A1.5-S0.5 specimens.

4.3.2 Morphological Characterization of CuO Thin Films

The surface morphologies and film thicknesses of the samples were studied using FESEM, and representative images are shown in **Figure 4.4 (a)-(j)**. The outer surfaces of the samples were found to be uniform and it was evident that the films fully covered the glass substrates. **Figure 4.4 (a)** demonstrates that the A1.5-S0.1 sample was composed of nanoparticles with an average diameter of 22.4 nm. This film was also flat, continuous and uniform with a thickness of 33.2 nm, as shown in **Figure 4.4 (b)**.

The effects of the amount of NH_3 on the film morphology were examined by varying the NH_3 concentration in the source solution from 3.0 to 6.0 M while maintaining the NaOH concentration at 0.1 M NaOH. Nanoparticle clusters composed of grains from 10 to 30 nm in size were observed on the surface of the A3.0-S0.1 specimen, such that the surface was relatively rough (**Figure 4.4 (c)**). The cross-sectional FESEM image of this same material, having a film thickness of 43.4 nm, showed that there were no cracks in the film thickness direction (**Figure 4.4 (d)**). In contrast, the A6.0-A0.1 sample comprised more rounded grains with sizes between 60 and 150 nm, as shown in **Figure 4.4 (e)**. **Figure 4.4 (e)** and **(f)** indicate that this film was 46.4 nm thick and made of grains having an average size of 102.1 nm. These results confirm that the CuO thin films prepared with a higher NH_3 concentration had larger grain sizes.

The NaOH concentration in the reaction solution was changed from 0.05 to 0.5 M while using 1.5 M NH_3 to investigate the effect of the NaOH amount on the morphological properties of the films. **Figure 4.4 (g)** and **(h)** show that the A1.5-S0.5 specimen consisted of nanoparticles having sizes of 20 to 50 nm and relatively flat surfaces. The average grain size in the A1.5-S0.5 was 37.2 nm, even for a film thickness of 57.8 nm. Hence, the grain size and film thickness of the A1.5-S0.5 were larger than

those of the A1.5-S0.1, indicating that a more rapid thin film growth rate was obtained when using a high NaOH concentration. Conversely, the A1.5-S0.05 sample fabricated from a low NaOH concentration solution had an extremely rough surface, as shown in **Figure 4.4 (i) and (j)**, along with a porous structure **Figure 4.4 (i)**.

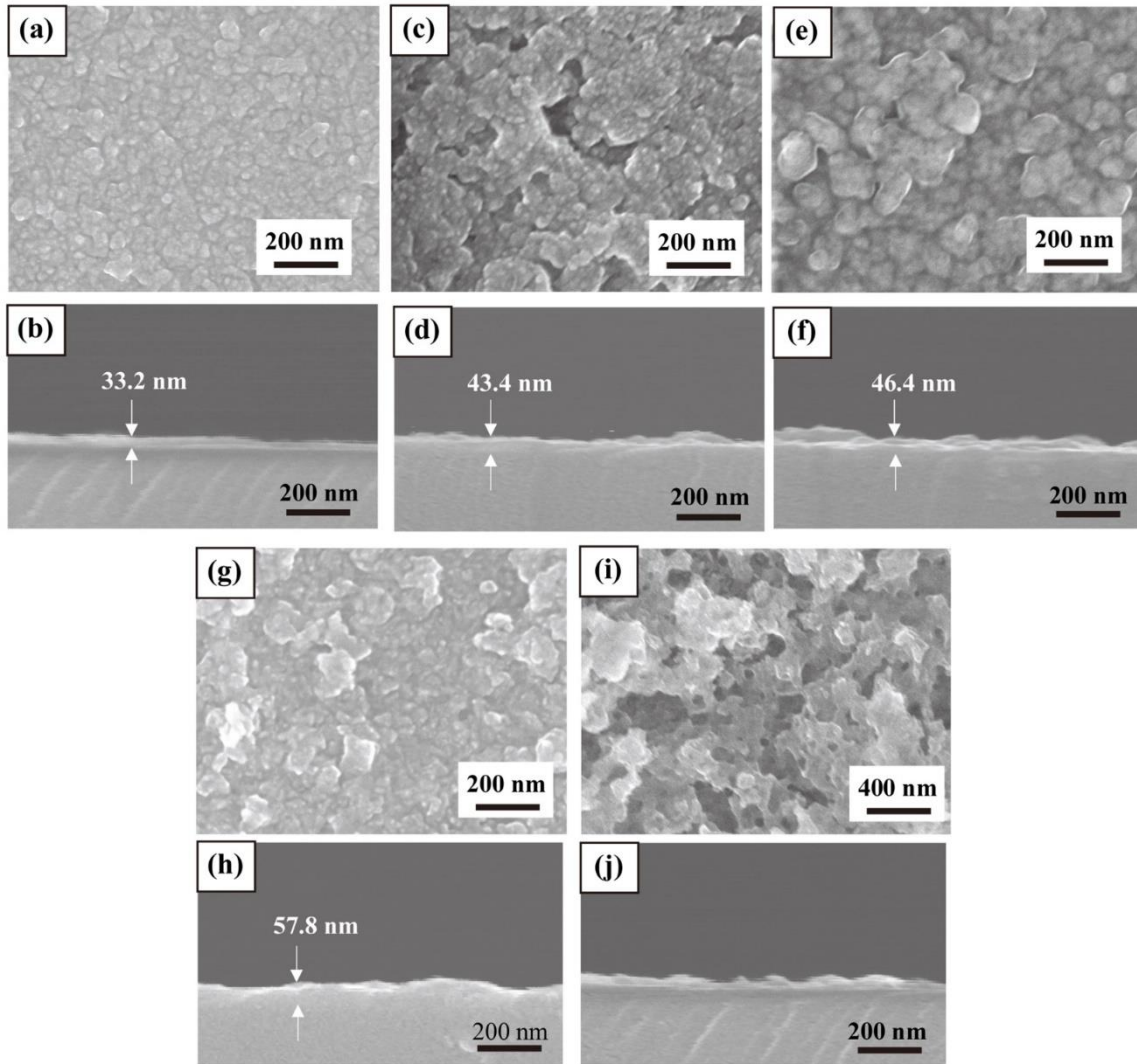


Figure 4.4 Surface and cross-sectional SEM images of the (a) (b) A1.5-S0.1, (c) (d) A3.0-S0.1, (e) (f) A6.0-S0.1, (g) (h) A1.5-S0.5 and (i) (j) A1.5-S0.05 specimens.

4.3.3 Optical Characterization of CuO Thin Films

Figure 4.5 (a) presents the UV-vis transmittance spectra of the nanostructured CuO thin films. The transmittance values of the A1.5-S0.1, A1.5-S0.5 and A6.0-S0.1 films ranged from 20% to 80% in the visible light region of the spectrum, indicating that these materials were semi-transparent. However, the A3.0-S0.1 and A1.5-A0.05 exhibited lower transparency at visible wavelengths as a consequence of the relatively rough surfaces of these films (**Figure 4.4 (c) and (i)**).

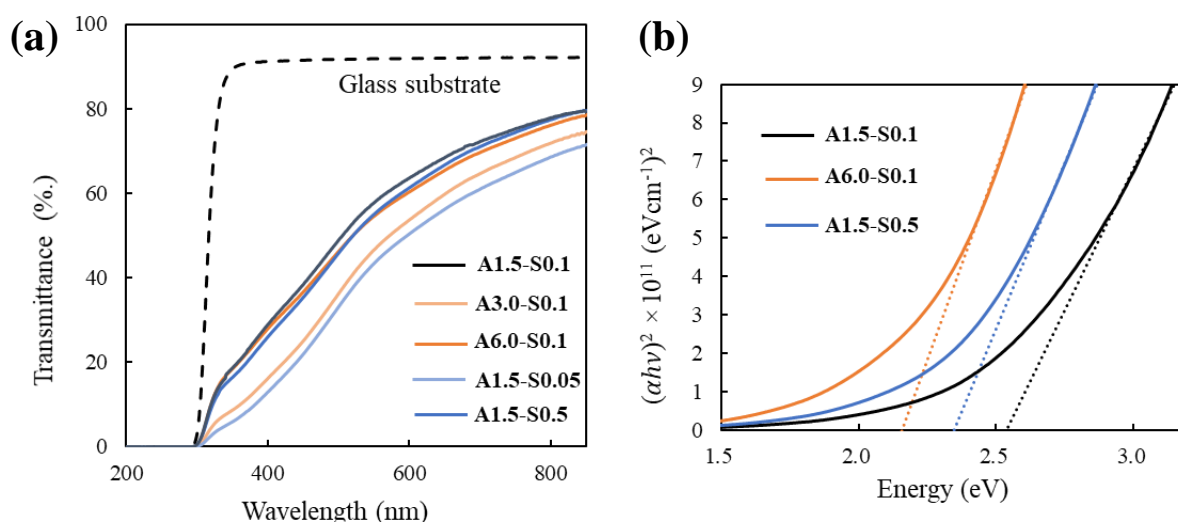


Figure 4.5 (a) UV-vis spectra of the A1.5-S0.1, A3.0-S0.1, A6.0-S0.1, A1.5-S0.5 and A1.5-S0.05 specimens and (b) Tauc plots for the A1.5-S0.1, A6.0-S0.1 and A1.5-S0.5 specimens.

4.4 Discussion

4.4.1 Film Formation Mechanism

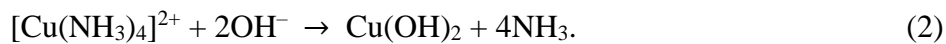
1.4.1.1 Thin Film Fabrication at Low Temperatures

In the MSS method, the source and reaction solutions are ultrasonically atomized and the resulting mists are sprayed onto the substrates using a flow of N_2 . In the present

work, the source mist contained the copper amine complex $[\text{Cu}(\text{NH}_3)_4]^{2+}$ that was generated in the source solution via the reaction



In addition, the NaOH in the reaction mist provides OH^- ions according to the reaction, so that the mist has a pH over 12. The CuO films were fabricated by spraying the source and reaction mists onto a substrate fixed on a rotating table, as shown in **Figure 4.6 (a)**. The nozzles dispensing the source and reaction mists were separate and the substrates were rotated so that each one was alternately exposed to the two mists. In other words, the two mists were supplied in an alternating manner to the substrates. This alternating supply system made it possible to provide a strongly alkaline environment in the region III shown in **Figure 4.6 (a)**, which was important for the fabrication of phase-pure CuO films at temperatures below 100 °C.¹¹ The rotating substrate started from the region I and arrived at the region III after passing through the region II-a, as shown in **Figure 4.6 (a)**. The copper amine complex in the source mist combined with OH^- ions in the reaction mist to form $\text{Cu}(\text{OH})_2$ nuclei on the substrate based on the reaction



In the region III, these $\text{Cu}(\text{OH})_2$ nuclei rapidly transformed to $\text{Cu}(\text{OH})_4^{2-}$ because of the excess of OH^- in the highly alkaline reaction mist, according to the reaction:¹²



Cudennec and Lecerf reported that $\text{Cu}(\text{OH})_4^{2-}$ rapidly generates CuO even at temperatures below 100 °C with the simultaneous loss of two OH^- and one water molecule via the reaction:¹³



Typically, the dehydration of $\text{Cu}(\text{OH})_2$ to form CuO occurs at relatively high temperatures in excess of $150\text{ }^\circ\text{C}$.^{13,14} However, during the MSS process, the reactions in eqs. (2)-(4) proceeded efficiently on the basis of the alternating supply of the source and reaction mists to the substrate surface, such that phase-pure CuO films could be produced at a lower temperature of $90\text{ }^\circ\text{C}$.

1.4.1.2 Fabrication of nanoscale thick, dense and high purity CuO films

In the present MSS method, the N_2 carrier gas continually transported the room temperature mist droplets to the $90\text{ }^\circ\text{C}$ substrate, after which these droplets adhered to the substrate surface as shown in **Figure 4.6 (a)** and **(b)**. The attached droplets were rapidly absorbed onto the substrate as a result of the high wettability of the ozone-treated glass such that a liquid film was formed (**Figure 4.6 (c)**). This film was thinner than $1.0\text{ }\mu\text{m}$ because the mist droplets had diameters in the range of $0.1\text{--}3\text{ }\mu\text{m}$.¹⁵ The distance between the nozzle and the substrate played an important role in the formation of the liquid film. When the distance was too small, the liquid film was blown out from the substrate surface by the carrier gas. On the other hands, when the distance was too long, the mist droplets were not able to reach the substrate surface, indicating that no liquid film was formed on the substrate. In this study, the distance of 2 mm was adjusted and it was the most appropriate to fabricate several tens nm thick CuO film.

The solid-liquid interface between the liquid film and the substrate surface was heated, while the gas-liquid interface between the liquid film and the atmosphere was cooled by the carrier gas and the room temperature droplets, creating a large temperature gradient between these two interfaces (**Figure 4.6 (d)**). As shown in **Figure 4.4**, the MSS method enabled the fabrication of crack-free, dense CuO films several tens of nm in

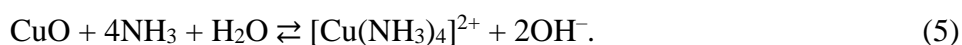
thickness, and the large temperature gradient played an important role in this process. In the region I, the mist droplets of the source solution were sprayed onto the rotating substrate and the liquid film was formed on the substrate surface. As a consequence of the temperature gradient in the liquid film, the copper amine complex was only decomposed near the substrate surface and Cu^{2+} ions adhered to the film surface. In the region II-a, the liquid film of source solution was eliminated from the substrate surface by the solution flow in the liquid film generated by the centrifugal force of the rotating table (**Figure 4.6 (c)**). As a result, any unreacted species and impurities such as amines and sulfates were removed and only Cu^{2+} ions remained on the film surface. When the rotating substrate arrived at the region III after passing the region II-a, the Cu^{2+} ions on the film surface reacted with OH^- ions to form CuO nuclei on the substrate via the reactions in eqs. (2)-(4). In the region II-b, any impurities including sodium ions were removed as the same way in the region II-a. Therefore, the high-purity CuO thin films were obtained by the MSS method.

In general, it is difficult to fabricate crack-free CuO thin films with nanoscale thickness by conventional solution processes. In solution processes, the formation of high-density nuclei on the substrates is required to prepare crack-free films. However, the crystal growth is promoted in the solution condition where nuclei are sufficiently formed, resulting in the fabrication of relatively thick films. In the MSS method, the strongly alkaline environment in the region III promoted the nuclei formation, resulting in the fabrication of dense film covering the entire substrate. On the other hands, the temperature gradient in the thin liquid film also confined the crystal growth to the thickness direction. Therefore, the MSS method enabled to fabricate crack-free CuO films having a thickness of approximately 30 nm. These films exhibited good adhesions to the substrates because

each CuO crystals in the films were grown only from the nuclei formed on the substrate surface.

1.4.1.2 Effect of NH₃ and NaOH on the film morphology

Figure 4.4 indicates that the surface morphology was changed when varying the NH₃ and NaOH concentrations. Specifically, films prepared with a higher NH₃ concentration had larger particle sizes. The NH₃ in the source solution reacted with dissolved CuO to form an amine via the reaction



The dissolution and reprecipitation of CuO crystals would have proceeded more rapidly on the film surface when using a higher NH₃ concentration. Consequently, the particle sizes in the film were increased as a result of Ostwald ripening associated with the dissolution of small crystals followed by the reprecipitation of larger crystals.¹⁶ The NaOH provided OH⁻ ions to the reaction field through the dissociation and promoted the growth of CuO crystals as shown in eqs. (2)–(4). The grain size and film thickness of the A1.5-S0.5 specimen were larger than those of the A1.5-S0.1 sample, as is evident in **Figure 4.4 (a) and (g)**, and the former material also exhibited a much rougher surface than the other films. The mist droplets generated by the ultrasonic atomizer had sizes of 0.1–3.0 μm and, when these droplets adhered to the liquid film on the substrate, a local gradient of the ratio of the NH₃ to NaOH concentrations was generated in the film. This gradient was especially large in the case of the A1.5-S0.05 sample because this film was prepared from the reaction solution having the lowest NaOH concentration. The reaction shown in eq. (5) by which CuO was dissolved would have proceeded more efficiently in regions within the liquid film having higher concentration ratios. However, the

dissolution and reprecipitation of CuO crystals (that is, Ostwald ripening) would have occurred locally at zones with lower NH_3 concentrations. Therefore, there were many pores on the surface of the A1.5-S0.05 film (**Figure 4.4 (i)**) because regions of high NH_3 to NaOH concentration ratios were present and CuO crystals at the edges of the pores were bonded via Ostwald ripening.

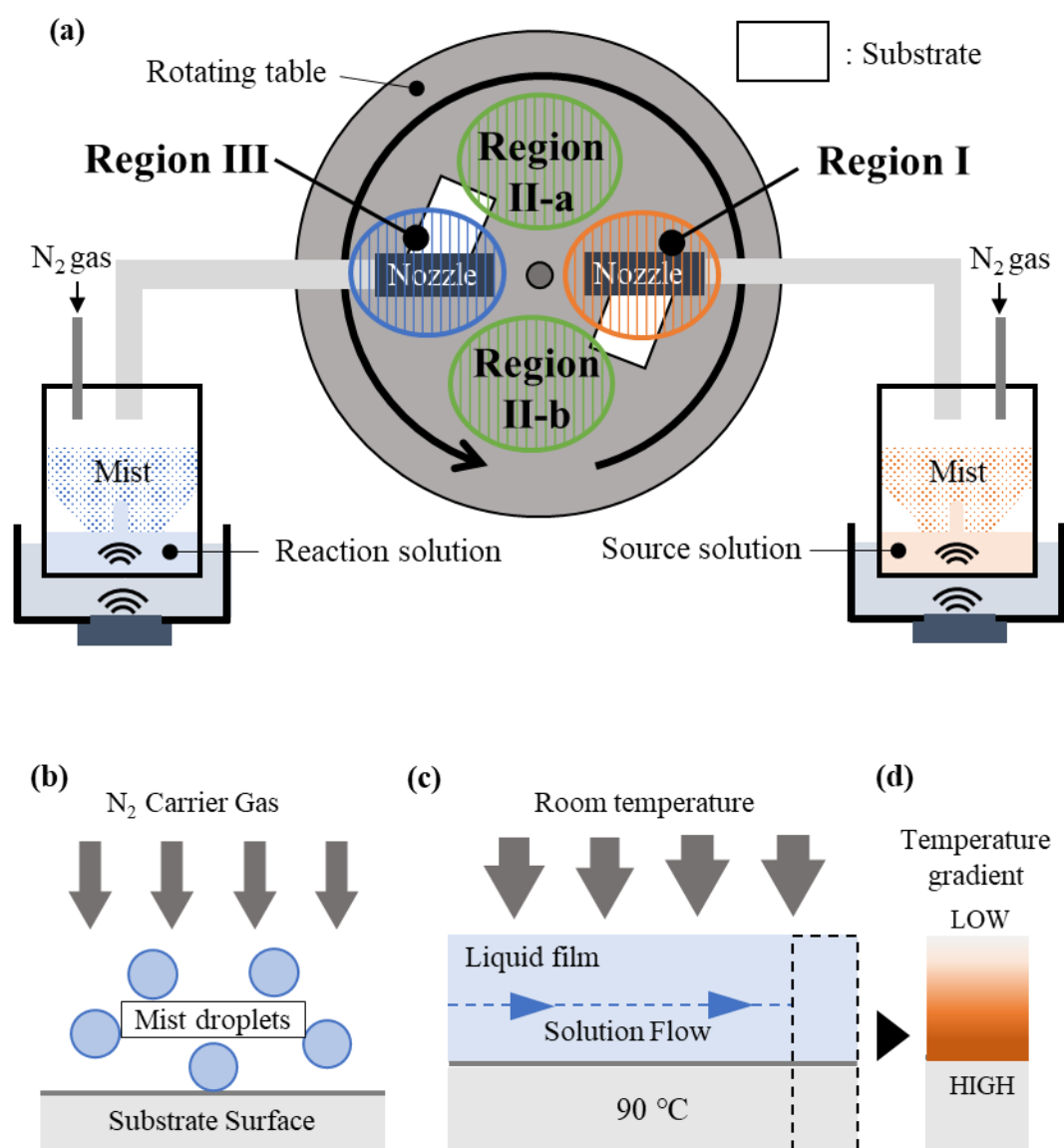


Figure 4.6 Schematic illustrations of (a) four regions on the rotating table, (b) mist droplets carried and adhered to the substrate surface, (c) the liquid film formed during film fabrication and (d) the temperature gradient around the liquid film.

4.4.2 Optical band gap evaluation

As shown in **Figure 4.5 (a)**, the UV-vis transmittance spectra of the samples showed the sharp absorption edge around the wavelength of 298 nm, which was attributed to the light absorption of the glass substrates. Besides, the relatively slow absorption was also observed in the wavelength range of 450 to 580 nm, assigned to the light absorption of the CuO film, as shown in the UV-vis spectra of the samples. The thickness of several tens nm was too small to absorb the light in the wavelength range of 450–580 nm efficiently and it was the reason why a direct band gap semiconductor CuO did not show the sharp variation.

The optical band gaps of the A1.5-S0.1, A1.5-S0.5 and A6.0-S0.1 specimens were calculated from optical transmittance data. These band gaps were determined on the basis of the relationship between the absorption coefficient of the material (α) and the photon energy ($h\nu$), written as

$$\alpha h\nu = A(E_g - h\nu)^n, \quad (7)$$

where E_g is the band gap energy, A is a constant and n has a value of 1/2 or 2 for allowed direct and indirect transitions, respectively. **Figure 4.6 (b)** presents plots of $(\alpha h\nu)^2$ versus $h\nu$ for the A1.5-S0.1, A1.5-S0.5 and A6.0-S0.1 films, from which the optical band gaps were obtained from the intercepts of extrapolated straight lines with the photon energy axis.¹⁷ On this basis, the A1.5-S0.1, A1.5-S0.5 and A6.0-S0.1 specimens, which had grain sizes varying from 10 to 100 nm, were found to possess direct band gaps of 2.54, 2.35 and 2.16 eV, respectively. The data in Fig. 6 also indicated that a blue shift in the optical band gaps with decreases in their grain size. Such a blue shift in CuO thin films with different grain sizes has been reported in many studies, where it has been

argued that the observed shift was due to the quantum confinement effects.¹⁸⁻²⁰ The quantum confinement in semiconductors originates from the geometric restraint of electrons and holes as independent wave-particles or as bound pairs known as excitons. If the grain size is smaller than the exciton Bohr radius (up to 28.7 nm for CuO), the quantum confinement effect will play an important role in the blue shift of the band gap.^{21,22} As shown in **Figure 4.4 (a)**, the average grain size of A1.5-S0.1 is 22.4 nm, which was smaller than the Bohr radius of CuO. **Figure 4.4 (e)** and **(g)** indicated that A1.5-S0.5 was mostly composed of grains smaller than 28.7 nm, while the grains of A6.0-S0.1 were larger than 28.7 nm. Therefore, the blue shift in band gaps of the A1.5-S0.1, A1.5-S0.5 and A6.0-S0.1 was due to the quantum confinement effect.

Conclusion

The MSS method was developed as a means of fabricating nanostructured CuO thin films on glass substrates without seed layers, and the resulting films showed good adhesion with the substrates. In this process, a copper amine complex source solution and a NaOH reaction solution are atomized using ultrasonic transducers to generate mists. These two mists are then sprayed onto heated substrates fixed on a rotating table, where they react to grow CuO thin films under atmospheric pressure. This method enables the fabrication of dense, crack-free CuO films having a thickness of approximately 30 nm at a relatively low temperature of 90 °C. Besides, it is possible to tune the grain size, surface morphology and optical band gap of the film by adjusting the concentrations of NH₃ and NaOH in the source and reaction solutions, respectively. Specifically, films prepared with higher NH₃ and NaOH concentrations show larger grain sizes and higher optical band gaps, while the use of a low NaOH concentration generates numerous pores on the film surface.

References

- [1] Q. Zhang, K. Zhang, D. Xu, G. Yang, H. Huang, F. Nie, C. Liu, S. Yang, *Prog. Mater. Sci.* 60 (2014) 208–337.
- [2] J. Sultana, S. Paul, A. Karmakar, R. Yi, G.K. Dalapati, S. Chattopadhyay, *Appl. Surf. Sci.* 418 (2017) 380–387.
- [3] Y. Akaltun, *Thin Solid Films.* 594 (2015) 30–34.
- [4] R. Nitta, Y. Kubota, T. Kishi, T. Yano, N. Matsushita, *Mater. Chem. Phys.* 243 (2020) 122442.
- [5] G.T. Dang, M.W. Allen, M. Furuta, T. Kawaharamura, *Jpn. J. Appl. Phys.* 58 (2019).
- [6] J. Park, K.T. Oh, D.H. Kim, H.J. Jeong, Y.C. Park, H.S. Kim, J.S. Park, *ACS Appl. Mater. Interfaces.* 9 (2017) 20656–20663.
- [7] H. Nishinaka, Y. Kamada, N. Kameyama, S. Fujita, *Phys. Status Solidi Basic Res.* 247 (2010) 1460–1463.
- [8] A.I. Stadnichenko, A.M. Sorokin, A.I. Boronin, *J. Struct. Chem.* 49 (2008) 341–347
- [9] Y. He, Z.S. Fishman, K.R. Yang, B. Ortiz, C. Liu, J. Goldsamt, V.S. Batista, L.D. Pfefferle, *J. Am. Chem. Soc.* 140 (2018) 1824–1833.
- [10] O.J. Silva Junior, A.F.F. Monteiro, J.B.L. Oliveira, A.M.U. Araújo, D.G. Silva, J. Kulesza, B.S. Barros, *Mater. Chem. Phys.* 235 (2019) 121737.
- [11] O. Gençyılmaz, T. Taşköprü, *J. Alloys Compd.* 695 (2017) 1205–1212.
- [12] A.Z. Liao, W.D. Zhu, J.B. Chen, X.Q. Zhang, C.W. Wang, *J. Alloys Compd.* 609 (2014) 253–261.
- [13] Y. Cudennec, A. Lecerf, *Solid State Sci.* 5 (2003) 1471–1474.
- [14] X. Wu, H. Bai, J. Zhang, F. Chen, G. Shi, *J. Phys. Chem. B.* 109 (2005) 22836–22842.
- [15] H. Nishinaka, Y. Kamada, N. Kameyama, S. Fujita, *Phys. Status Solidi Basic Res.* 247 (2010) 1460–1463.
- [16] S. Li, D. Chu, L. Wang, R. Rong, N. Zhang, *Phys. E Low-Dimensional Syst. Nanostructures.* 126 (2021) 114489.
- [17] M. Dahrul, H. Alatas, Irzaman, *Sci.* 33 (2016) 661–667.
- [18] S. Rehman, A. Mumtaz, S.K. Hasanain, *J. Nanoparticle Res.* 13 (2011) 2497–2507.
- [19] P. Mallick, S. Sahu, *Nanosci. Nanotechnol.* 2 (2012) 71–74.
- [20] R. Daira, A. Kabir, B. Boudjema, C. Sedrati, *Solid State Sci.* 104 (2020) 106254.

- [21] J. Yang, W. Yin, B. Zhou, A. Cui, L. Xu, D. Zhang, W. Li, Z. Hu, J. Chu, *J. Phys. Chem. C*. 123 (2019) 27165–27171.
- [22] Q. Zhang, K. Zhang, D. Xu, G. Yang, H. Huang, F. Nie, C. Liu, S. Yang, *Prog. Mater. Sci.* 60 (2014) 208–337.

Chapter 5 Conductive ZnO Films Fabricated by Spin-spray Method

5.1 Introduction

Zinc oxide (ZnO) receives significant attention for use in electronics due to several desirable properties, including a wide energy band gap (3.37 eV) and good optical transparency in the visible light.¹ ZnO films have been synthesized using many physical and chemical processes, such as radio frequency magnetron sputtering, pulsed laser deposition and chemical spray pyrolysis.²⁻⁷ However, these methods may require a complex system and high fabrication temperatures, leading to certain disadvantages, such as high environmental impacts or significant expense.

Previous studies reported the preparation of transparent ZnO films at 90 °C by the spin-spray method, a facile and low-environmental-load solution process.⁸ The resistivity of these films was over 10 $\Omega\cdot\text{cm}$ —too high for use as transparent electrodes. UV light irradiation to these films for one day at room temperature decreased the film resistivity drastically, four orders of magnitude or more, to 4.4×10^{-3} $\Omega\cdot\text{cm}$.⁹ Previous studies reported that citric acid was contained in the films; UV irradiation reduced the citric acid amount through the photocatalytic effect of ZnO. The improvement of conductivity was assumed to result from doping ZnO with the products of decomposition of citric acid, such as hydrogen and carbon, without clear evidence.¹⁰ The identification of donor species is important for further decreasing the resistivity and increasing applications of the films.

5.2 Experiments

5.2.1 Fabrication of ZnO films via spin-spray method

Aqueous solution of zinc nitrate hexahydrate (Wako Pure Chemical Industries, Ltd., Japan, 99.0%) and ammonia-water (Wako Pure Chemical Industries, Ltd., Japan, 28.0%) with trisodium citrate (Wako Pure Chemical Industries, Ltd., Japan, 97.0%) were used as the source and reaction solutions. Here, Millipore deionized water was used for preparing the solutions. The source solution was prepared by dissolving 10 mM of zinc nitrate in 1000 mL of deionized water. The reaction solution was prepared by dissolving 60 mL of ammonia-water and 4 mM of trisodium citrate in 940 mL of deionized water. The substrates, which consisted of borosilicate glass $40 \times 30 \times 0.17$ mm³ in size (mastunami glass industry, Ltd, Japan), were washed in an ultrasonic bath with Millipore deionized water and ethanol for 10 min each. The rinsed substrates were exposed to a glow discharge plasma for 10 min to obtain a hydrophilic surface. They were then mounted on a rotating table for spin-spray deposition; the temperature and rotation rate of the table were 90 °C and 150 rpm, respectively. The source solution and reaction solution were simultaneously sprayed onto the substrates through separate nozzles using diaphragm pumps. The supply rate of each solution was 3.0 L h⁻¹, and the deposition time was 10 min. After deposition, the ZnO films were subjected to UV irradiation using a black-light-blue lamp (FL8BLB, Toshiba Lighting & Technology Co., Japan, wavelength = 300-400 nm, intensity = 1 mW/cm²) for 1 h to obtain conductive films.

5.2.2 Characterization

The resistivity of the films was measured using the four-probe method with a resistivity meter (MCP-T610; Mitsubishi Chemical AnalyTech.). The crystallographic

properties were evaluated by x-ray diffraction analysis (XRD; Rint2000; Rigaku). The elemental depth profile in the films were measured by Time-Of-Flight Secondary Ion Mass Spectrometry (TOF-SIMS; ION-TOF). The transmittance of the films was confirmed with a UV–Vis spectrometer (Lambda 35 spectrometer; Perkin Elmer).

5.3 Results

5.3.1 Morphology and XRD Analysis of ZnO Film

A ZnO film was fabricated on a glass substrate by the spin-spray method as in the previous study.^{8,9} **Figure 5.1** shows the surface and cross-sectional SEM images of the ZnO films. No pores or cracks were observed in the SEM images (**Figure 5.1 (a)**). As shown in **Figure 5.1 (b)**, the film thickness was 1.0 μm . **Figure 5.2 (a)** shows the XRD patterns of the sample before and after UV treatment. The XRD peaks show good correspondence to the wurtzite phase of ZnO, according to the ICDD data (No. 36-1451), without the presence of an impurity peak from $\text{Zn}(\text{OH})_2$. The crystal structures of the ZnO films did not change greatly before and after UV irradiation, but the (002) peak slightly shifted to a lower 2θ value after UV treatment, indicating an increase in interplanar distance, d_{002} (**Figure 5.2 (b)**).¹⁰

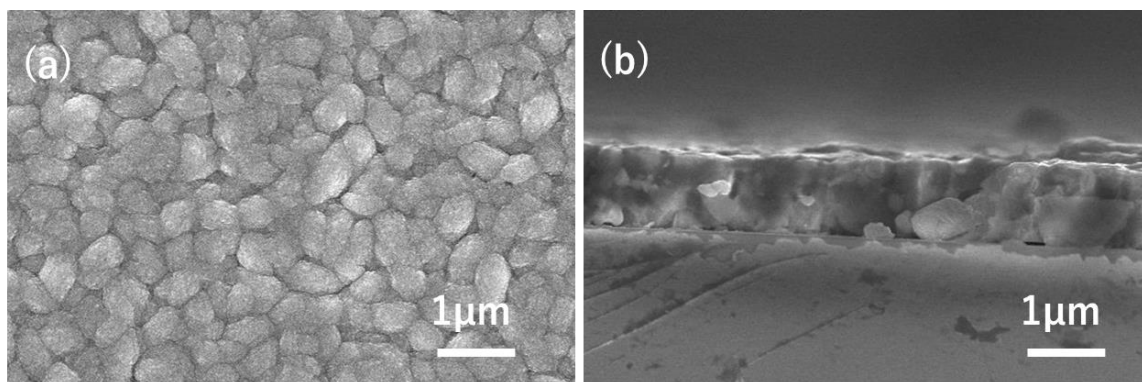


Figure 5.1 (a) Surface and **(b)** cross-sectional SEM images of the ZnO film.

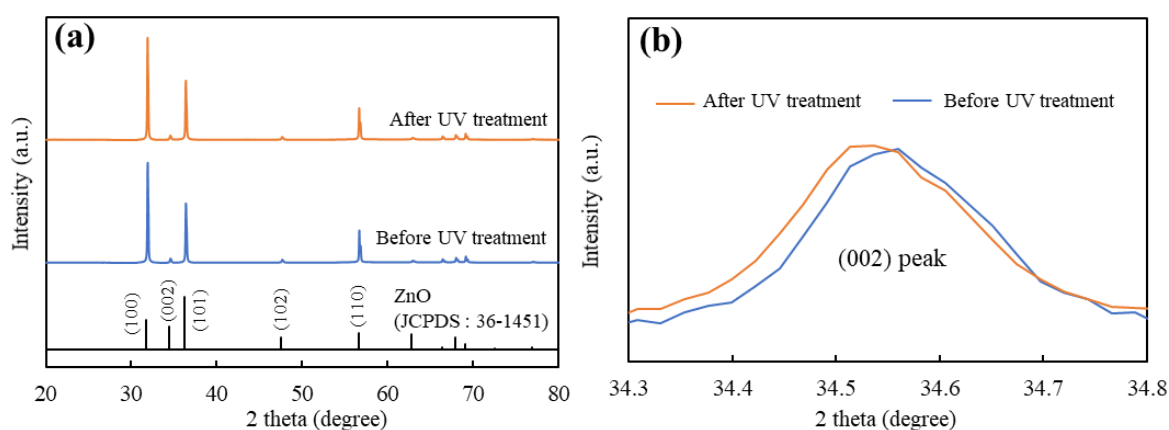


Figure 5.2 (a) The XRD patterns and (b) the peak shift of the (002) peak of the ZnO film before and after UV treatment.

5.3.2 Electrical and optical properties of ZnO Film

Figure 5.3 (a) demonstrates the decrease of the resistivity of the ZnO film by UV light irradiation for 60 min at room temperature and the electrical properties of the sample after UV treatment. The as-grown sample, in the absence of any dopant ions, showed a high resistivity of $55.3 \Omega \cdot \text{cm}$. However, the resistivity of the UV-treated sample was $4.43 \times 10^{-2} \Omega \cdot \text{cm}$, which was three orders of magnitude lower than that of the as-grown sample. The resistivity did not change even after subsequent dark storage for 3 days, indicating that the reduced resistivity was clearly maintained in the absence of UV light. The carrier concentration and the mobility of the sample after UV treatment for 60 min were $2.00 \times 10^{20} \text{ cm}^{-3}$ and $0.95 \text{ cm}^2/\text{V} \cdot \text{s}$, respectively (**Figure 5.3** (a)). The UV-treated sample had a lower carrier mobility, but a much higher carrier concentration compared with ZnO films doped with group 13 (IIIa) elements, such as Al, Ga and In, prepared by other methods.¹¹⁻¹³ **Figure 5.3** (b) shows the UV-vis spectra of the sample before and after UV treatment. Both samples had a transmittance of 75%–85 % and an absorption edge around 380 nm. In the near-infrared region, the as-grown sample had a high transmittance of more than 80%, while the UV-treated sample showed a low

transmittance. The optical band gap of the samples before and after UV treatment were 3.36 eV and 3.55 eV, respectively, as calculated from extrapolating the linear portion of the Tauc Plot ($(\alpha h\nu)^2$ vs. $h\nu$, where α is the absorption coefficient and $h\nu$ is the photon energy) to the energy axis (**Figure 5.3 (b)**).¹⁴

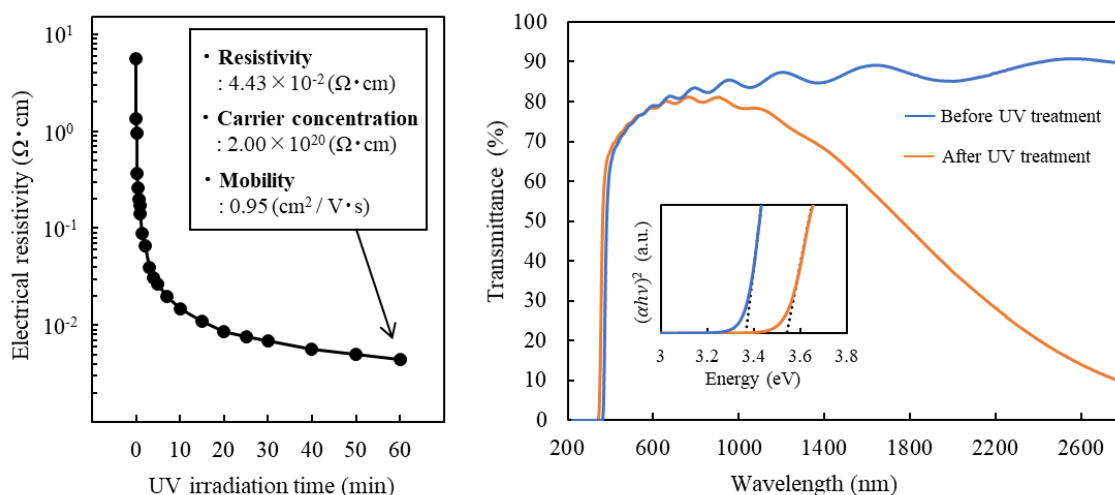


Figure 5.3 (a) The resistivity of the ZnO film with UV light irradiation times; the inset presents the electrical properties of the sample after UV treatment for 60 min. **(b)** The optical transmittance and of the ZnO film before and after UV treatment; the inset presents the optical band gap of the ZnO film before and after UV treatment.

5.3.3 Elemental analysis of ZnO Film

The elemental profile in the samples before and after UV treatment were measured by time-of-flight secondary ion mass spectrometry (TOF-SIMS; ION-TOF) and ^1H solid-state NMR spectroscopy as shown in **Figure 5.4**. Note that the sputtering rate of the UV-treated sample with high conductivity is slightly faster than that of the low-conductivity as-grown sample. The CH_3COO^- and ZnO^- signals in **Figure 5.4 (a)** were attributed to the citric acid and the ZnO film. In the spin-spray method, the ZnO film was prepared using the source solution containing citric acid. As shown in **Figure 5.4 (a)**, citric acid exists only around the film surface, and the amount of citric acid

drastically decreased after UV treatment. The OH^- signal in the ZnO film was higher than the ZnO^- signal as shown in **Figure 5.4 (a)**, implying a large amount of hydrogen in the ZnO film prepared by the spin-spray method.

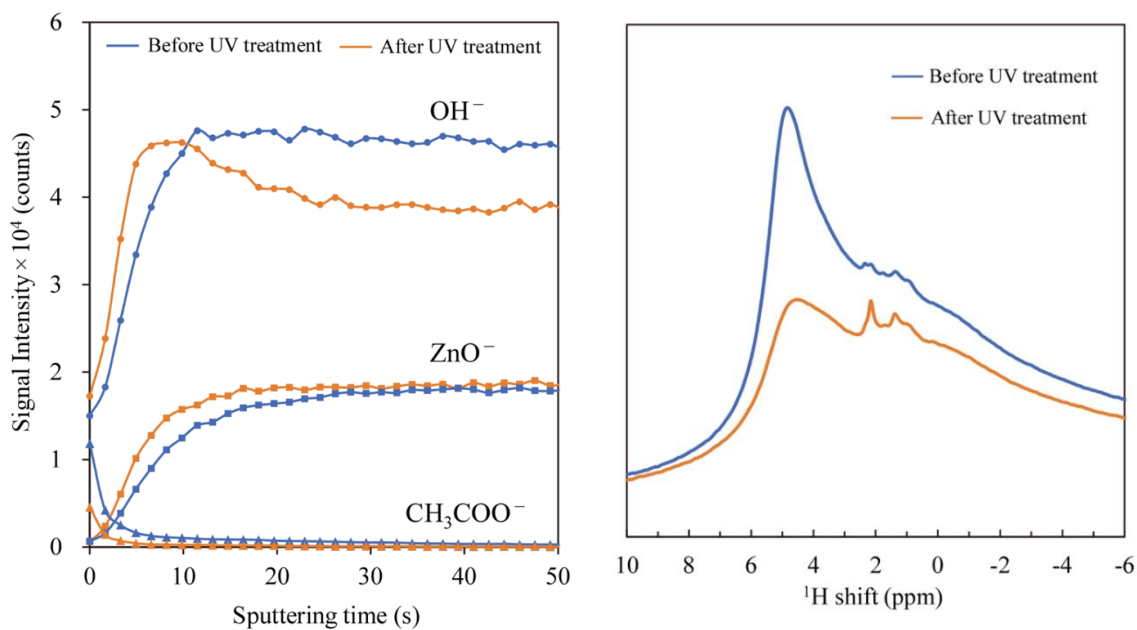


Figure 5.4 (a) TOF-SIMS depth profiles of the ZnO film before and after UV treatment. **(b)** ^1H solid-state NMR spectra of the ZnO film before and after UV treatment.

5.4 Discussion

5.4.1 Donor Formation in ZnO Film by UV Treatment

Figure 5.3 (a) showed that the high resistivity, $55.3 \Omega \text{ cm}$, of the as-deposited ZnO film by the spin-spray method was drastically decreased down to $4.43 \times 10^{-2} \Omega \text{ cm}$ after UV treatment for 60 min. In addition, the UV-treated sample had a much higher carrier concentration of $2.00 \times 10^{20} \text{ cm}^{-3}$. As shown in **Figure 5.3 (b)**, the shift of the band gap to a higher value after UV treatment can be ascribed to the Brustein–Moss effect arising from the increase in carrier concentration induced by UV irradiation.¹⁵ Besides, in the near-infrared region, the as-grown sample had a high transmittance of more than

80%, while the UV-treated sample showed a low transmittance (**Figure 5.3 (b)**). This result revealed that the UV-treated sample was degenerate; the fermi energy penetrates the conduction band because of its high electron carrier concentration, above 10^{20} cm^{-3} .¹⁶ In contrast, the high near-infrared transmittance of the as-grown sample demonstrated that it was not degenerate and had a lower carrier concentration than the UV-treated sample did. These results indicated the generation of new donors with high concentration in the ZnO film by UV treatment.

5.4.2 Identification of Donor Species by Elemental Analysis

To investigate the dopant ions in the ZnO film, the elemental profile in the samples before and after UV treatment were measured by TOF-SIMS; ION-TOF, XRD analysis and ^1H solid-state NMR spectroscopy. As shown in **Figure 5.4 (a)**, citric acid exists only around the film surface, and the amount of citric acid drastically decreased after UV treatment because of ZnO-photocatalyzed decomposition.¹⁷ Previous studies reported that the improvement of conductivity was assumed to result from doping ZnO with the products of decomposition of citric acid, such as hydrogen and carbon.¹⁸ However, citric acid exists only around the film surface, and therefore has little influence on the bulk resistivity of the as-grown sample. After UV treatment, the amount of citric acid drastically decreased because of ZnO-photocatalyzed decomposition of citric acid around the surface into H_2O and CO_2 , which were released into the atmosphere.¹⁷ Therefore, the decomposition of citric acid did not greatly affect the electrical properties of the UV-treated sample; that is, it is not a direct cause of the decrease in resistivity of the ZnO film by UV irradiation. Precious report that ZnO nanorod arrays were fabricated by using the reaction solution without citric acid via the spin-spray method.⁸ The high

resistivity, $1.84 \times 10^3 \Omega \text{ cm}$, of the as-deposited ZnO nanorod arrays was drastically decreased down to $7.31 \times 10^{-1} \Omega \text{ cm}$ with 4-point probe method after UV treatment for 60 min. This results also indicated that citric acids did not contribute to conductivity improvement. In chapter 6, flexible photodetector was fabricated by using the conductive ZnO nanorod arrays after UV treatment.

Incorporated hydrogen (H) in the form of interstitial hydrogen in bond-centered sites (H_i), substitutional hydrogen on the oxygen lattice site (H_O), and three O–H bonds in a zinc vacancy ($V_{Zn}-H_3$) exists as shallow donors which contribute to the n-type conductivity of ZnO^{19,20}. The conductivity of undoped ZnO has been believed to be caused by native defects, such as oxygen vacancies (V_O) and interstitial zinc (Zn_i). However, many studies have recently reported that the V_O exhibit deep energy levels in the ZnO gap and cannot act as shallow donors, indicating that V_O trap two electrons.²¹ Besides, Zn_i is expected to be present at a low concentration under the n-type condition due to its high formation energy.²² Therefore, unintentionally-incorporated H is considered to be a likely source of n-type conductivity with a high carrier concentration. H-related defects in ZnO have attracted great interest and have been extensively studied because of their profound effects on the electrical properties of ZnO. ¹H solid-state NMR spectroscopy represents a powerful and quantitative technique that can detect and distinguish hydrogen species in different local environments. **Figure 5.4 (b)** shows the ¹H NMR spectra of the samples before and after UV treatment. A high, broad peak at 4.9 ppm and a set of low peaks from 0 ppm to 2.5 ppm can be observed for the as-grown sample. The NMR spectrum of the UV-treated sample shows that the intensity of the relatively broad peak at 4.9 ppm significantly decreased, while that of the set of peaks at 0–2.5 ppm, assigned to H_O and $V_{Zn}-H_3$, increased after UV treatment for 60 min.^{23,24}

These results revealed that the improved conductivity of the sample film upon UV irradiation results from the generated H donors such as H_0 and $V_{Zn}-H_3$ in the ZnO film. The broad peak at 4.9 ppm can be attributed to water trapped in ZnO crystals.^{25,26} The H_i gives rise to a narrow peak at 4.1 ppm, but the trapped water peak intensity was too high to detect the H_i peak in **Figure 5.4 (b)**.

5.4.3 Hydrogen Donor Formation by UV Light Irradiation

In agreement with the interpretation of the NMR results, the OH^- signal in **Figure 5.4 (a)** can be attributed to trapped water, indicating that the ZnO film prepared by the spin-spray method contained a large amount of water in the ZnO crystals. In this method, the ZnO film was fabricated through the dehydration of $Zn(OH)_2$; water formed by dehydration remained in the film due to the low temperature of fabrication. As shown in **Figure 5.4 (a)**, the OH^- signal intensity of the UV-treated sample was lower than that of the as-grown sample in the film, indicating the decrease of trapped water from UV treatment. This result was in good agreement with the NMR results as shown in **Figure 5.4 (b)**. In contrast, the OH^- signal intensity around the film surface did not change before and after UV treatment. Therefore, the decrease of the trapped water in the ZnO film was not due to the release of species into the atmosphere. These results in **Figure 5.4 (a)** and **(b)**, suggested that the trapped water decomposed to form the H_0 and $V_{Zn}-H_3$ upon UV treatment via the mechanism proposed below, as shown in **Figure 5.5**.

- (1) Holes and electrons with strong oxidation and reduction powers were generated when the photocatalytic ZnO film was irradiated with UV light.
- (2) The generated holes decomposed the trapped water to form H^+ ions and OH radicals.

(3) The formed H^+ ions and the electrons associated with V_O and V_{Zn} to generate the H_O and $V_{Zn}-H_3$, respectively.^{19,20,24} Concurrently, the electrons associated with the V_O reduced OH radicals to form OH^- ions, which were then incorporated into the V_O , resulting in the formation of the thermodynamically stable H_i .¹⁹

As shown in **Figure 5.2 (b)**, the (002) peak slightly shifted to a lower 2θ value after UV treatment, indicating an increase in interplanar distance, d_{002} . The d_{002} spacing was reported to decrease with increasing oxygen vacancy in ZnO films.¹⁰ Therefore, this observed increase of d_{002} spacing in **Figure 5.2 (b)** suggests the incorporation of H donors such as H_i , H_O and $V_{Zn}-H_3$ into the ZnO lattice with a decrease in oxygen vacancies after UV irradiation.

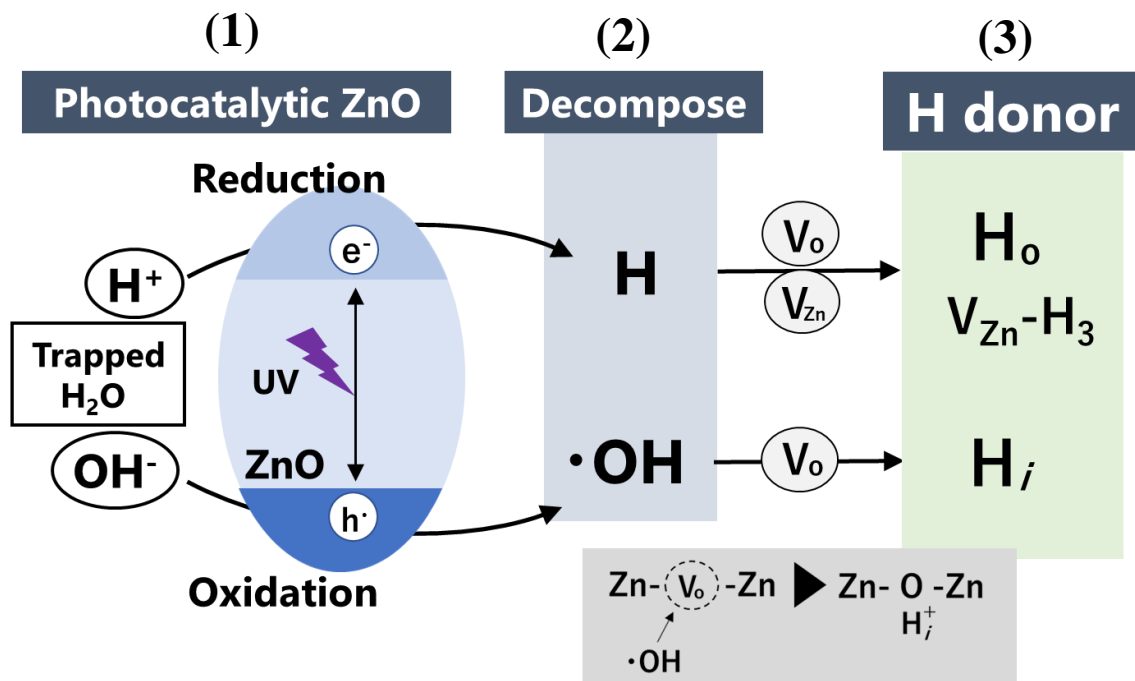


Figure 5.5 Schematic illustration of the hydrogen donor formation mechanism in the ZnO film by UV treatment.

Conclusion

The high resistivity, 55.3 Ω cm, of the as-deposited ZnO film by the spin-spray method was drastically decreased down to 4.43×10^{-2} Ω cm after UV treatment for 60 min. UV-vis analysis confirmed the increase of carrier concentration indicating the generation of new donors in the ZnO film by UV treatment. The TOF-SIMS depth profile and ^1H solid-state NMR spectroscopy analysis revealed a large amount of trapped water in the as-deposited ZnO film, while hydrogen donors, such as H_i , H_O and $\text{V}_{\text{Zn}}-\text{H}_3$, were formed in the UV-treated ZnO film. The trapped water was decomposed to form H^+ and OH^- ions by photocatalytic activity of UV- irradiated ZnO. These ions associated with the V_O and V_{Zn} resulted the generation of thermodynamically stable H donors.

References

- [1] A. Mallick, D. Basak, *Prog. Mater. Sci.* 96 (2018) 86–110.
- [2] J.S. Jang, J. Kim, U. Ghorpade, H.H. Shin, M.G. Gang, S.D. Park, H.J. Kim, D.S. Lee, J.H. Kim, *J. Alloys Compd.* 793 (2019) 499–504.
- [3] D.B. Potter, M.J. Powell, I.P. Parkin, C.J. Carmalt, *J. Mater. Chem. C.* 6 (2018) 588–597.
- [4] T. Coman, D. Timpu, V. Nica, C. Vitelaru, A.P. Rambu, G. Stoian, M. Olaru, C. Ursu, *Appl. Surf. Sci.* 418 (2017) 456–462.
- [5] Y. Cai, X. Li, P. Sun, B. Wang, F. Liu, P. Cheng, S. Du, G. Lu, *Mater. Lett.* 112 (2013) 36–38.
- [6] W. Wu, G. Hu, S. Cui, Y. Zhou, H. Wu, *Cryst. Growth Des.* 8 (2008) 4014–4020.
- [7] V. Khranovskyy, R. Yakimova, F. Karlsson, A.S. Syed, P.O. Holtz, Z. Nigussa Urgessa, O. Samuel Oluwafemi, J. Reinhardt Botha, *Phys. B Condens. Matter.* 407 (2012) 1538–1542.
- [8] H. Wagata, N. Ohashi, T. Taniguchi, K.I. Katsumata, K. Okada, N. Matsushita, *Cryst. Growth Des.* 10 (2010) 4968–4975.
- [9] H. Wagata, N. Ohashi, K.I. Katsumata, H. Segawa, Y. Wada, H. Yoshikawa, S. Ueda, K. Okada, N. Matsushita, *J. Mater. Chem.* 22 (2012) 20706–20712.
- [10] X. Li, Y. Wang, W. Liu, G. Jiang, C. Zhu, *Mater. Lett.* 85 (2012) 25–28.
- [11] A. Nakrela, N. Benramdane, A. Bouzidi, Z. Kebbab, M. Medles, C. Mathieu, *Results Phys.* 6 (2016) 133–138.
- [12] S. Pati, P. Banerji, S.B. Majumder, *RSC Adv.* 5 (2015) 61230–61238.
- [13] C. Lung, M. Toma, M. Pop, D. Marconi, A. Pop, *J. Alloys Compd.* 725 (2017) 1238–1243.
- [14] V. Kumar, N. Singh, R.M. Mehra, A. Kapoor, L.P. Purohit, H.C. Swart, *Thin Solid Films.* 539 (2013) 161–165.
- [15] K.G. Saw, N.M. Aznan, F.K. Yam, S.S. Ng, S.Y. Pung, *PLoS One.* 10 (2015) 1–17.
- [16] L. Peng, L. Fang, Y. Zhao, W. Wu, H. Ruan, C. Kong, *J. Wuhan Univ. Technol. Mater. Sci. Ed.* 32 (2017) 866–870.
- [17] J.S. Jang, J. Kim, U. Ghorpade, H.H. Shin, M.G. Gang, S.D. Park, H.J. Kim, D.S. Lee, J.H. Kim, *J. Alloys Compd.* 793 (2019) 499–504.
- [18] H.E. Lin, J.S. Hong, R. Nitta, Y. Kubota, Y. Katayanagi, H. Wagata, T. Kishi, T. Yano, N. Matsushita, *Appl. Surf. Sci.* 489 (2019) 135–141.
- [19] A. Janotti, C.G. Van De Walle, *Reports Prog. Phys.* 72 (2009).

- [20] J. Villafuerte, F. Donatini, J. Kioseoglou, E. Sarigiannidou, O. Chaix-Pluchery, J. Pernot, V. Consonni, *J. Phys. Chem. C*. 124 (2020) 16652–16662.
- [21] A. Janotti, C.G. Van De Walle, *Appl. Phys. Lett.* 87 (2005) 1–3.
- [22] D.C. Look, J.W. Hemsky, J.R. Sizelove, *Phys. Rev. Lett.* 82 (1999) 2552–2555.
- [23] M. Wang, G. Yu, W. Ji, L. Li, W. Ding, *Chem. Phys. Lett.* 627 (2015) 7–12.
- [24] L.Q. Wang, G.J. Exarhos, C.F. Windisch, C. Yao, L.R. Pederson, X.D. Zhou, *Appl. Phys. Lett.* 90 (2007).
- [25] T. Li, M. Wang, X. Liu, M. Jin, F. Huang, *J. Phys. Chem. Lett.* 11 (2020) 2402–2407.
- [26] J.K. Park, H.J. Kwon, C.E. Lee, *Sci. Rep.* 6 (2016) 1–8.

Chapter 6 Flexible Applications of Metal Oxide Films Fabricated by Controlling Spin Spray Reaction

6.1 Introduction

Recently, flexible bending sensors have attracted considerable attention owing to the widespread use of wearable and healthcare device.^{1,2} Typically, they are composed of a flexible polymer substrate and sensing materials. Various types of sensing materials, including metal materials, conductive polymers, and functional metal oxide, have been used to fabricate flexible sensors.³⁻⁵ Generally, metal materials and conductive polymers are expensive, have low long-term stability, and require the complex and high-cost fabrication methods. On the other hands, the advantages of metal oxides, including their non-toxicity, low cost, and long-term durability, are of great significance in the development of flexible sensors for wearable electronics.⁶ However, it is difficult to fabricate metal oxide films on flexible polymer substrates with low heat and chemical durability due to their high fabrication temperature and complex processes. Therefore, there were few reports on flexible bending sensors based on metal oxides.

Spin-spray method and mist spin spray method enable to the low temperature fabrication of metal oxide films at low temperature below 100°C with high deposition rate through the effective utilization of “spin spray reactions”. In chapter 2,3,4, various metal oxide films including ZnO, Cu₂O and CuO films were fabricated below 90°C in 10 min by the spin-spray method. Besides, chapter 5 reported the fabrication of CuO thin film at 90°C in 30 min using the mist spin spray method. All of these processes using utilizing spin spray reaction do not deteriorate the substrate duet to their low fabrication temperature and short deposition time. In this chapter, various types of flexible sensors

applications fabricated on PET substrates were investigated using Cu₂O, CuO and ZnO films fabricated on by the spin-spray method and MSS method.

6.2 Flexible Bending Sensor based on Cu₂O Films

6.2.1 Experiment

6.2.1.1 Fabrication and Performance of Cu₂O Bending Sensor

According to **Chapter 2**, the spin-spray method enabled the one-step fabrication of a Cu₂O film at the low temperature of 70°C. A Cu₂O film was fabricated on PET substrates (40 × 40 × 0.125 mm) via the spin-spray method. Chapter 2 provides more detail on the fabrication process of a Cu₂O film via the spin-spray method. The source solution and the reaction solution were prepared by using the mixed CuSO₄·5H₂O (0.04 M) and C₆H₈O₆ (0.04 M) solution and by dissolving NaOH (0.4 M) in NH₃ aq. (1.2 M) solution, respectively.

The bending deformation of the sensor was performed by changing the distance between both of its ends. The bending characteristic was evaluated using the curvature measured from the shape profile of the sensor captured by a charge-coupled device (CCD) camera. The electrical signals of the bending deformation were recorded at the same time using a Keithley 2400 digital meter at a constant voltage of 5 V. The mechanical fatigue of the sensor was investigated using bending–release cycles (Tension-Free U-shape Folding Test Jig DLDM111LH and Desktop model bending endurance tester TCDM111LH, Yuasa System Co., Ltd., Japan).

6.2.1.2 Characterization of Cu₂O Bending Sensor

The crystallinity and microstructure of the samples were analyzed using X-ray diffraction (XRD; Rint2000; Rigaku). The surface morphologies of the samples were

examined using field-emission scanning electron microscopy (FESEM, HITACHI, Japan, S-4700). X-ray photoelectron spectroscopy (XPS; Physical Electronics, Inc., USA, PHI 5000) was used to investigate the chemical states. All the XPS spectra were fitted using a numerical simulation program (XPSPEAK 41) with a Shirley background and a Lorentzian/Gaussian line shape. The presence of impurities in the samples was confirmed using attenuated total reflection Fourier-transform infrared (ATR-FTIR) spectroscopy (FT-IR IRPrestige-21, Shimadzu Corp., Japan).

6.2.2 Result and Discussion

6.2.2.1 Characterization of the Cu₂O Film on the PET Substrate

According to **Chapter 2**, the spin-spray method enabled the one-step fabrication of a Cu₂O film at the low temperature of 70°C with a high deposition rate of >0.35 μm/min. Because this method results in low heat damage of the substrate during fabrication, fabrication could be achieved even on the PET substrate with a low thermal durability. **Figure 6.2.1 (a)** shows the uniformly deposited, orange sample on the substrate. The film exhibited strong adhesion to the substrate without peeling off, even after ultrasonication at 45 kHz of 200 W in deionized water for 10 min. It is important for the fabrication of metal oxide films by the spin-spray method to increase the hydrophilicity of the substrate surface by the plasma treatment before the film fabrication. There were a large number of polar functional groups such as carbonyl, hydroxyl and aldehyde/ketone (-COOH, -OH and -CO), on the surface of the PET substrate due to the hydrophilicity caused by plasma treatment.⁷ The formed crystal nuclei of Cu₂O due to heterogeneous nucleation were chemically bonded to the functional groups on the substrate surface and grew to form a Cu₂O film, as indicated in eq. (3). Therefore, the film fabricated by the spin-spray method exhibited strong adhesion to the substrate.

Figure 6.2.1 (b) presents the surface and cross-sectional SEM images of the sample. The 3.56- μm -thick film was uniform with a relatively flat surface and composed of submicron-sized grains, as shown in **Figure 6.2.1 (b)**. The spin-spray method enabled the fabrication of a Cu_2O film with a larger particle size at a higher deposition rate than the Cu_2O films fabricated by other methods. This morphology was very similar to that of $\text{S}_{0.4}\text{-A}_{0.8}$, as shown in **Figure 2.3 (e)** and **6.2.1 (b)**

The structural properties of the sample on the PET substrate were characterized by XRD, and the obtained patterns are presented in **Figure 6.2.1 (c)**. The XRD peaks corresponded to the cubic phase of Cu_2O with good accordance to the ICDD data (No. 77-0199) in addition to PET peaks without the presence of impurity peaks from $\text{Cu}(\text{OH})_2$ or CuO . The presence of impurities in the sample was further analyzed using XPS and ATR-FTIR. **Figure 6.2.1 (d)** presents the XPS spectra of the $\text{Cu}2\text{p}$ region for the sample. The peaks at 932.4 and 952.2 eV correspond to $\text{Cu}2\text{p}_{3/2}$ and $\text{Cu}2\text{p}_{1/2}$, respectively, indicating the presence of Cu^+ .⁸ As shown in Figure 2e, the $\text{Cu}2\text{p}_{3/2}$ peak could be fitted to a single peak with a binding energy of 932.4 eV. These XPS results indicate the pure phase formation of Cu_2O without impurities such as metal Cu, CuO , and $\text{Cu}(\text{OH})_2$. **Figure 6.2.1 (f)** presents the ATR-FTIR spectra of the sample. The band at approximately 600 cm^{-1} is attributed to the vibrational mode of Cu-O in Cu_2O .⁹ No band was present between 3000 and 3500 cm^{-1} , which corresponds to the region of O-H and N-H stretching, and no ascorbic acid-related bands were detected.^{10,11} The ATR-FTIR results indicate that the sample film did not contain any impurities, such as water, amines, or ascorbic acid. These results were very similar to those of $\text{S}_{0.4}\text{-A}_{1.2}$, as shown in **Figure 6.2.1 (b)** and **2.4 (e)-(f)**.

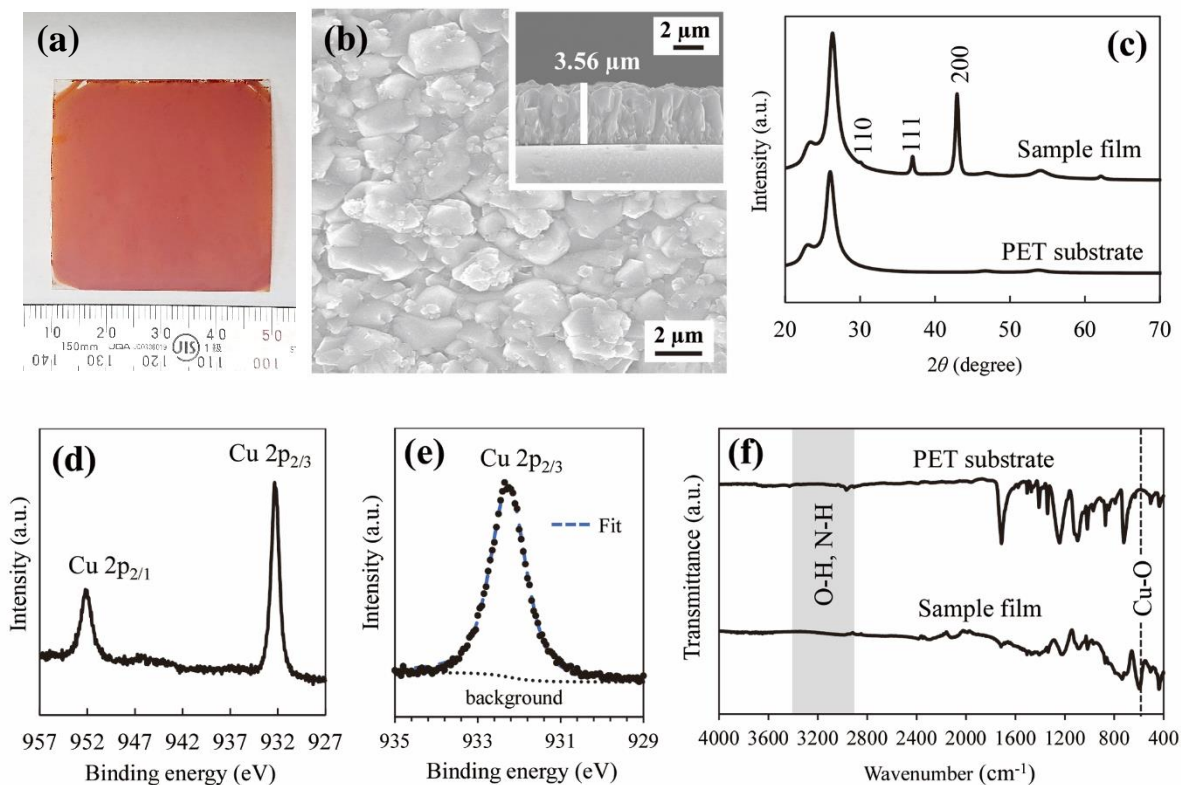


Figure 6.2.1 (a) Photograph of fabricated Cu_2O film, (b) surface and cross-sectional FESEM image of sample film, (c) XRD patterns of sample film and PET substrate, (d) XPS Cu 2p spectra of sample film, (e) XPS curve fitting of $\text{Cu}2p_{3/2}$ peak, and (f) ATR-FTIR spectra of sample film.

6.2.2.2 Fabrication of the Anisotropic Cu_2O Bending Sensor

To fabricate a flexible bending sensor by using the fabricated Cu_2O film, silver (Ag) paste was printed on top of the film sample at the two counter ends using the squeegee method as the contact electrodes ($40 \text{ mm} \times 10 \text{ mm}$), to which Cu wires were attached for the film resistance measurement. **Figure 6.2.2 (a)** presents photographs of the bending sensor based on the Cu_2O film fabricated by the spin-spray method. The sensor was sufficiently flexible to be used in bent conditions, as shown in **Figure 6.2.2 (b)**. Curvature (κ) was the most appropriate criterion to evaluate the bending characteristics, and thus, in the present study, the bending performance was evaluated by

measuring the electrical resistance between the electrodes under various curvatures.¹² To investigate the anisotropic bending performance of the sensor, the resistance change was measured under various curvature when bending in parallel and perpendicular to the direction of current flow. As illustrated in **Figure 6.2.2 (c) and (d)**, we study the Cu₂O bending sensor in two bending modes; parallel bending and perpendicular bending.

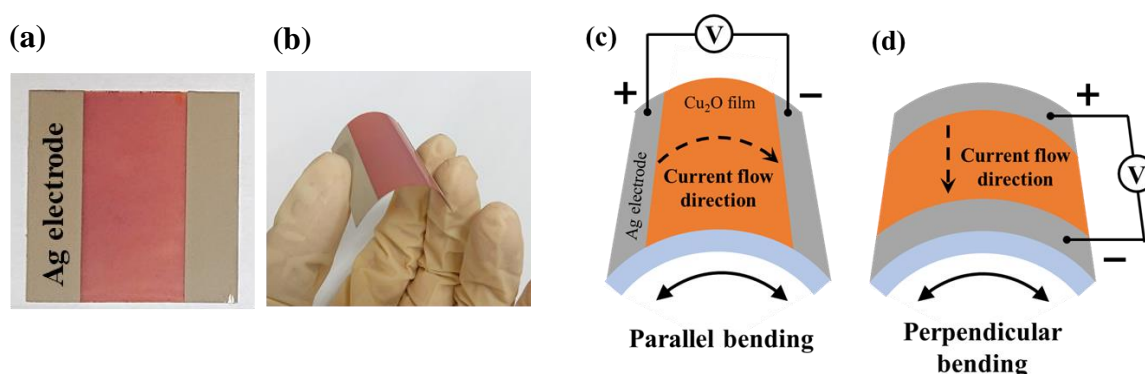


Figure 6.2.2 (a) Photograph of the Cu₂O bending sensor and **(b)** the sensor in a bent state and schematic illustration of the bending **(c)** parallel and **(d)** perpendicular to the current flow direction.

6.2.2.3 Performance of the Anisotropic Cu₂O Bending Sensor

Figure 6.2.3 (a) presents the I–V curves of the sensor in the parallel and perpendicular bending with various curvatures such as 0, 0.10, 0.15, and 0.20 mm⁻¹. An excellent linear relationship between the voltages and currents is observed in all the I–V curves, indicating the ohmic behavior and constant resistance of the sensor in the static state. The slope of the I–V curves, which is negatively correlated to the resistance, decreased significantly as the curvature in the parallel bending increased, demonstrating the excellent electromechanical performance. On the other hands, the slope of the I–V curves changed little in the perpendicular bending. **Figure 6.2.3 (b)** shows the relative resistance variation ($\Delta R/R_0$, where ΔR is the relative change in resistance and R_0 is the resistance of the Cu₂O bending sensor under the flat state) under various curvature in the

parallel and perpendicular bending. While the parallel bending led to the high resistance change of the sensor, the resistance variation changed little in the perpendicular bending. The sensor responded to a wide range of the parallel bending with curvatures between 0 and 0.21 mm^{-1} . Besides, it is clear from **Figure 6.2.3 (b)** that the Cu_2O bending sensor showed the excellent anisotropic bending performance. The electrical bending performance in the parallel bending was further investigated by evaluating the sensor sensitivity with the gauge factor (GF), which is defined as $\text{GF} = (\Delta R/R_0)/\varepsilon$, where ε is the applied strain. The applied strain can be calculated from the formula $\varepsilon = (d \times \kappa)/2$, where d is the thickness of the PET substrate and κ is the applied curvature.¹³ In the present study, d is 0.125 mm. As shown in **Figure 6.2.3 (b)**, the curve of the resistance variation in the parallel bending versus curvature can be divided into two linear parts, which are region I ($0 < \kappa < 0.05 \text{ mm}^{-1}$) and II ($0.05 < \kappa < 0.2 \text{ mm}^{-1}$) with the regression coefficient (R^2) of 0.993 and 0.995, respectively. The high linearity in each of the two regions shows that the Cu_2O sensor possesses excellent sensing properties. In addition, the GFs in the two regions were 5.31 and 21.8, respectively, indicating the good bending sensitivities.

In region I ($0 < \kappa < 0.05 \text{ mm}^{-1}$), the linear response of the Cu_2O -based sensor is due to the piezoresistive effect in the Cu_2O film, which is a p-type semiconductor. In semiconductors, the changes in resistivity are related to the change in mobility induced by the lattice deformation.¹⁴ In general, the resistivity of p-type semiconductors increases linearly with respect to the strain due to the increase of the hole population with decreased mobility by the deformation.¹⁵ This characterization of the piezoresistive effect is consistent with the result in region I of **Figure 6.2.3 (b)**, showing the sensing performance with high linearity. However, the bending sensing performance in region II ($0.05 < \kappa < 0.20 \text{ mm}^{-1}$) is due not only to the piezoresistive effect but also to the “grain-boundary

resistance effect". As shown in **Figure 6.2.1 (b)**, there are many grain boundaries in the polycrystalline Cu₂O film composed of submicron-sized grains. The bending would lead to the expansion of the distance between the grains along the bending direction, resulting in the increase of grain-boundary resistance.¹⁶ Because the distance between the grains expands in proportion to the applied strain (ϵ), the resistance variation in the bending changes linearly with the curvature (κ) calculated from the formula $\kappa = (2/d) \times \epsilon$.¹⁷ The combined effect of this grain-boundary resistance and the piezoresistive effect led to the high linear response of the Cu₂O bending sensor shown in region II. On the other hands, the perpendicular bending applies no stress in the direction of current flow, indicating that both of lattice deformation and the distance between the grains in the direction changes little. Therefore, the resistance in the direction perpendicular to the bending direction hardly changes due to the small inhibition of the conductive pathways, resulting in the anisotropic bending performance of the Cu₂O sensor.

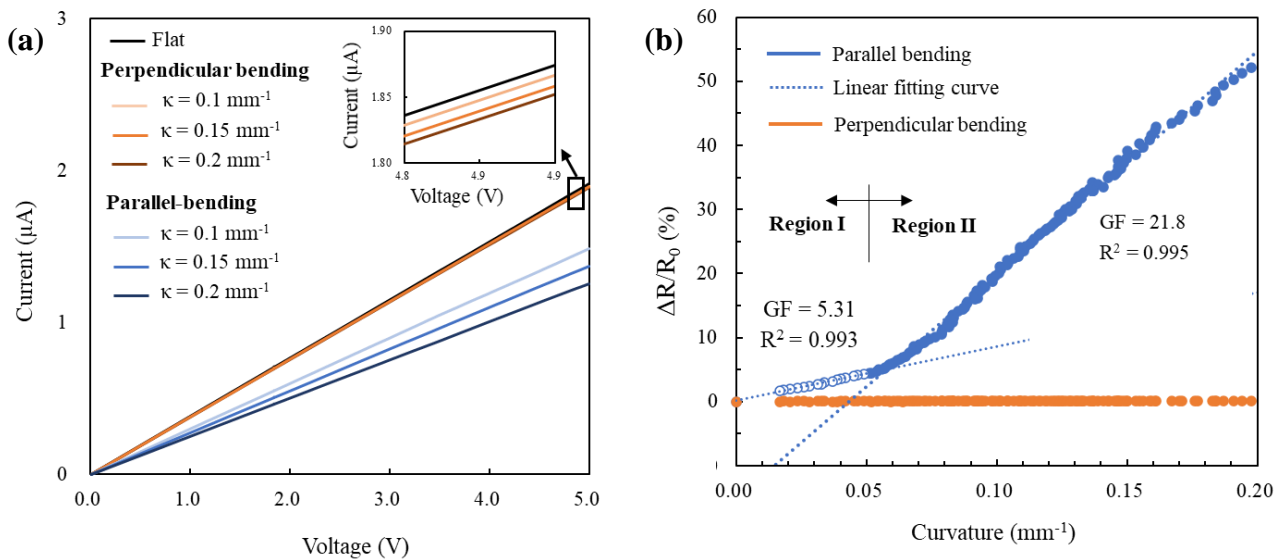


Figure 6.2.3 (a) I–V curves of bending sensor in the parallel and perpendicular bending with curvatures of 0, 0.10, 0.15, and 0.20 mm⁻¹ and **(b)** resistance variation of bending sensor under a wide range of the bending with curvatures between 0 and 0.21 mm⁻¹.

The resolution, repeatability and mechanical fatigue durability are important characteristics of the sensor devices from the perspective of practical applications. To evaluate the resolution of the Cu₂O bending sensor, the sensing response to minute changes in curvature when bending in parallel to the current flow direction was investigated. **Figure 6.2.4 (a)** shows the resistance variation of the sensor held at various curvatures (0.164, 0.167, 0.170, 0.172, and 0.175 mm⁻¹) for 5 s. The sensor responded to very small curvature changes ($\Delta\kappa = \sim 0.03 \text{ mm}^{-1}$, i.e., $\Delta\varepsilon = \sim 1.88 \times 10^{-3}$), demonstrating the high-resolution performance. In addition, the sensor had a short response time (~ 163 ms) between curvatures of 0.164 and 0.167 mm⁻¹, as shown in **Figure 6.2.4 (a)**. **Figure 6.2.4 (b)** shows the repeatability of the sensor investigated by exercising the bending–release cycle between curvatures of 0 and $\sim 0.16 \text{ mm}^{-1}$. The result of **Figure 6.2.4 (b)** demonstrated that the resistance variation of the sensor showed almost no frequency dependence in certain bending. Such reliable response is essential for practical applications of bending sensors such as motion monitoring.

Figure 6.2.4 (c) shows the fatigue testing of the sensor for 1,000 bending–release cycles at 1.0 Hz between curvatures of 0 and $\sim 0.16 \text{ mm}^{-1}$. The sensor resistance at the flat state increased slightly from 0 to 1,000 bending–release cycles. The change in the resistance before and after the fatigue testing was approximately 20%. The sensor displayed good repeatability and reversibility even after approximately 1,000 bending–release cycles, indicating the sufficient durability and stability of the sensor for practical applications. The thickness of the Cu₂O film was 3.56 μm as shown in **Figure 6.2.1 (b)**, which was small compared to the thickness of the PET substrate (0.125 mm). The applied strain of the film at bending state can be approximated to the surface strain of the PET substrate. Therefore, the strain of the Cu₂O film when bending between the curvatures of

0 and 0.16 mm^{-1} was very small (0.01), indicating that the film was not deformed significantly.

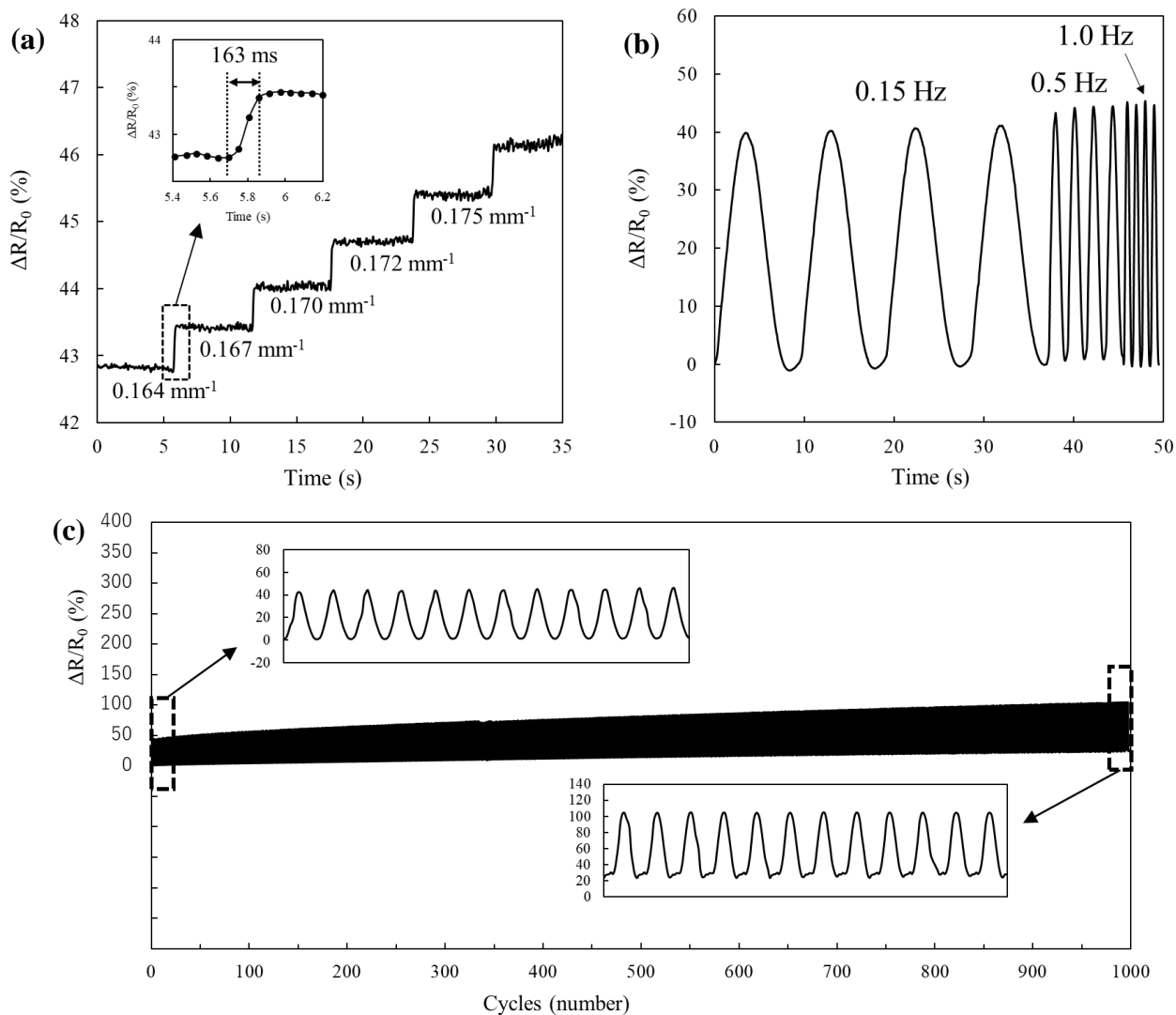


Figure 6.2.4 Resistance variation of the bending sensor held (a) at curvatures of 0.164, 0.167, 0.170, 0.172 and 0.175 mm^{-1} for 5 s, (b) under bending–release cycle between curvatures of 0 and 0.16 mm^{-1} at a frequency of 0.15, 0.5, and 1.0 Hz, and (c) Resistance variation of the bending sensor held for 1000 bending–release cycles between curvatures of 0 and 0.16 mm^{-1} at a frequency of 1.0 Hz.

6.2.3 Applications of Cu₂O Bending Sensor

Given its excellent bending stability and sensitivity, the Cu₂O bending sensor can be used for wearable devices to detect human motions. The sensor, which is thin, flexible, and non-toxic, can be easily attached to the human body. In addition, this sensor can be easily cut with scissors to fit the size of the detection points on the human body. To demonstrate the feasibility of the Cu₂O bending sensor, a real-time detection example is presented in **Figure 6.2.5**. First, the sensor was cut and attached to the index finger to monitor the finger motion, as shown in **Figure 6.2.5 (a)**. **Figure 6.2.5 (a)** and **(b)** show the real-time sensing curves toward the finger bending and stretching at various motion angles and speeds, respectively. In addition, the sensor was attached to the wrist to monitor specific wrist motions, as shown in **Figure 6.2.5 (c)** and **(d)**. These results demonstrate the excellent stability and repeatability of the sensor over a wide range of motion angles and speeds. In addition, the sensor was cut and adhered directly to the throat to monitor neck, chin, and larynx motions, as shown in the **Figure 6.2.5 (e)**. **Figure 6.2.5 (e)** shows the real-time response patterns for nodding, mouth opening/closing, and swallowing motions, which were caused by neck, chin, and larynx movement, respectively. The sensor can monitor not only large-scale human activity such as nodding but also small-scale human motion such as mouth opening/closing and swallowing. All these results demonstrate the potential application of the Cu₂O bending sensor for high-performance wearable electronic devices for health-care monitoring.

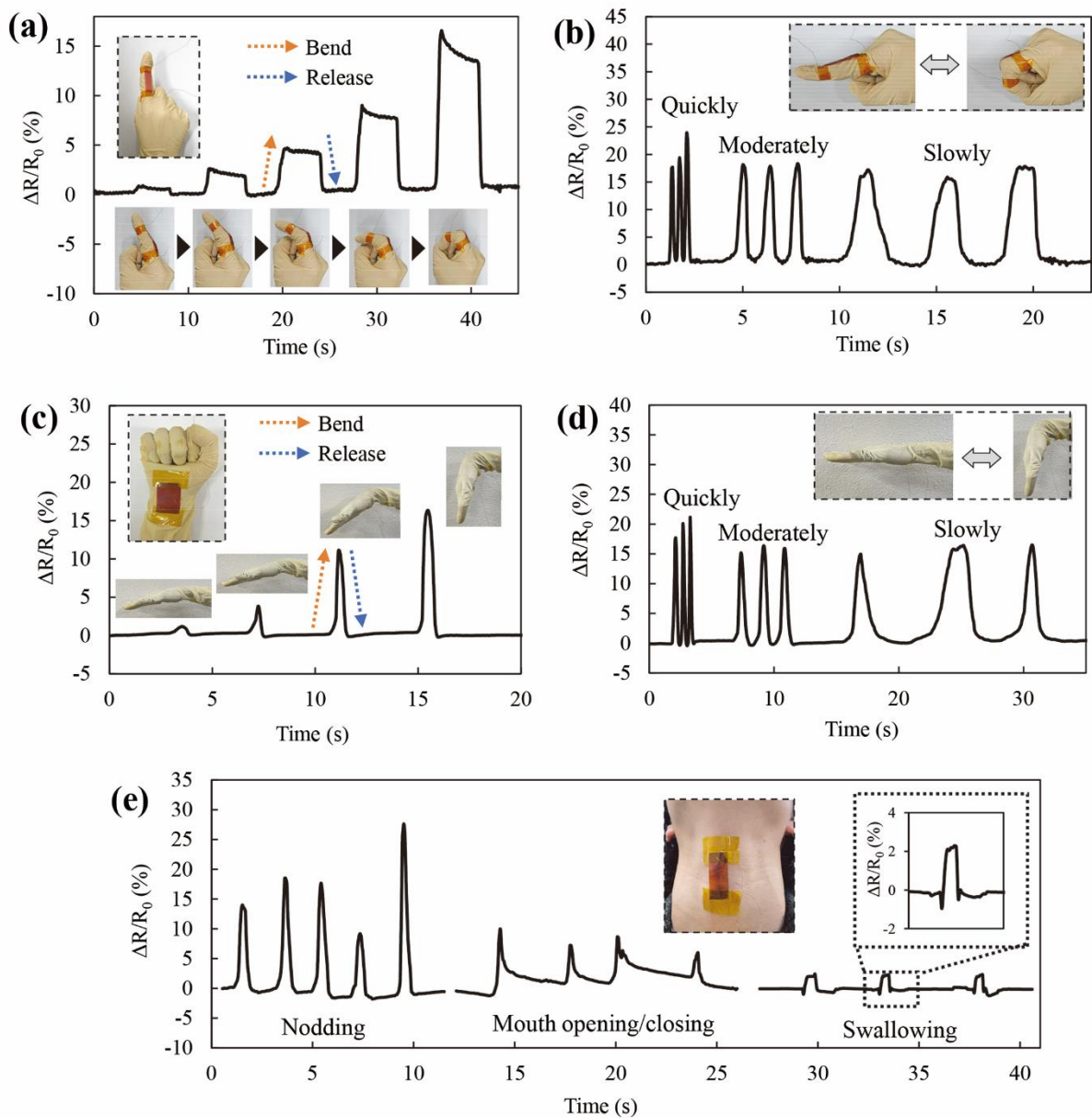


Figure 6.2.5. Real-time monitoring of human motions by the bending sensor. Sensing curves of the bending sensor attached on an index finger under different (a) motion angles and (b) motion speeds; the inset presents photographs of the finger bending to the corresponding positions. Sensing curves of the bending sensor attached on a wrist under different (c) motion angles and (d) motion speeds; the inset presents photographs of the wrist bending to the corresponding positions. (e) Nodding, mouth opening/closing, and swallowing sensing by attaching the bending sensor to the throat; the inset presents photographs of the bending sensor attached to the throat.

The high anisotropic response in various direction endows the Cu₂O bending sensor the potential ability to monitor not only simple motions such as the bending and stretching, but also complicated human body motions. We prepared two anisotropic bending sensors (sensor A and B) and sandwiched the insulating PET sheet between the sensors to fabricate the integrated sensor with a three-layer structure, as shown in **Figure 6.2.6 (a)**. Note that the sensor A and B attached to each other perpendicular to the electrode direction as shown in **Figure 6.2.6 (b)**. The angle illustrated in **Figure 6.2.6 (c)** rotated from the x-axis (parallel to the electrode direction of sensor A) to the bending direction line is defined as θ , which is referred to as a bending direction angle in the present study. To evaluate the bending performance of the integrated sensor, the resistance of the sensor A and B were measured, respectively. **Figure 6.2.6 (d)** shows the resistance variations of the integrated sensor at the bending direction angle of 0°, 45° and 90°. At the bending direction angle of 0°, the sensor A showed the high bending response, while the sensor B showed almost no response. On the contrary, the bending at 90° led to the high bending response of sensor B but little change in the resistance variation of the sensor A. Both of the sensor A and B responded slightly to the bending at 45°. The integrated sensor was attached on the wrist surface as shown in **Figure 6.2.6 (e)**. **Figure 6.2.6 (e)** shows the resistance variation of the sensor during bending and stretching motions of the wrist at various angles. The sensor A responded rapidly and repeatedly against the wrist motions at various angles, while the sensor B showed little bending response against the motions. In addition, the integrated sensor was attached the palm of the hand to monitor the hand gesture, such as “zero”, “one”, “two” and “three”, as shown in **Figure 6.2.7 (a)-(d)**. In comparison with the bending responses of the sensor A and B, the integrated sensor was able to monitor the complicated hand motions such as the

gesture “zero”, “one”, “two” and “three” which caused the sensor to bend at the bending direction angle of approximately 0° , 10° , 45° and 90° , respectively, as shown in **Figure 6.2.7 (e)**. All these indicated that the Cu_2O bending sensor possesses a great potential for monitoring the detailed and complicated human motion.

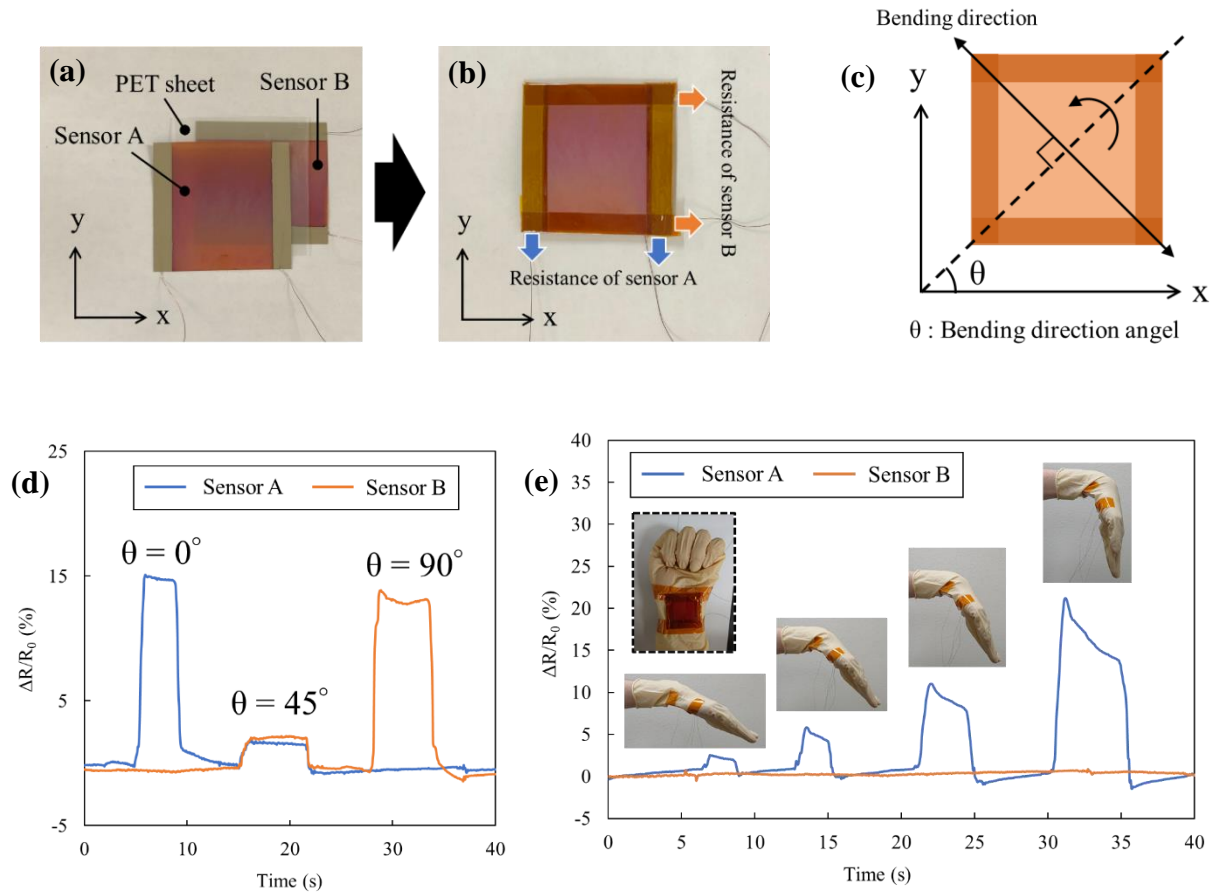


Figure 6.2.6. (a)-(b) Photograph of the integrated bending sensor, (c) schematic illustration of the bending direction angle and sensing curves of the integrated bending sensor (d) under various bending direction angles and (e) attached on a wrist under different motion angles; the inset presents photographs of the wrist bending to the corresponding positions.

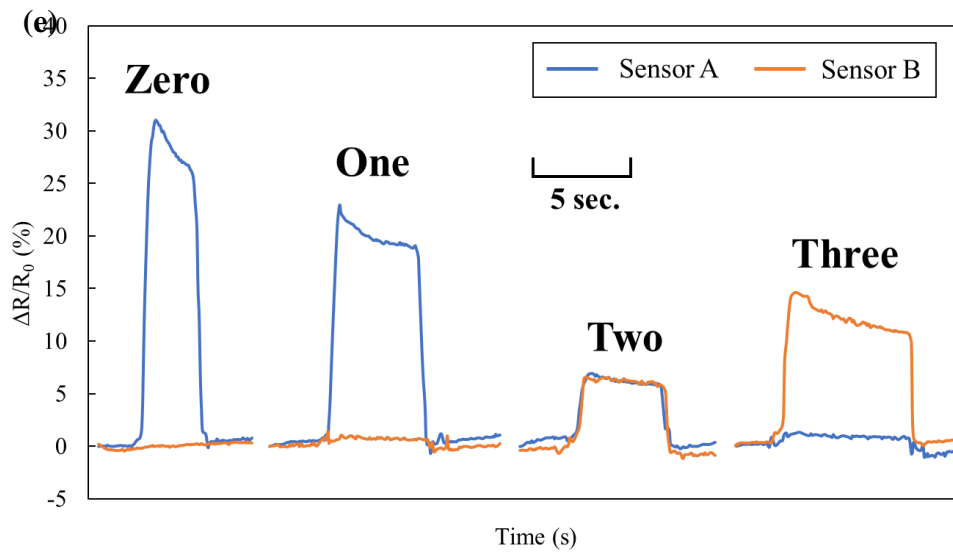
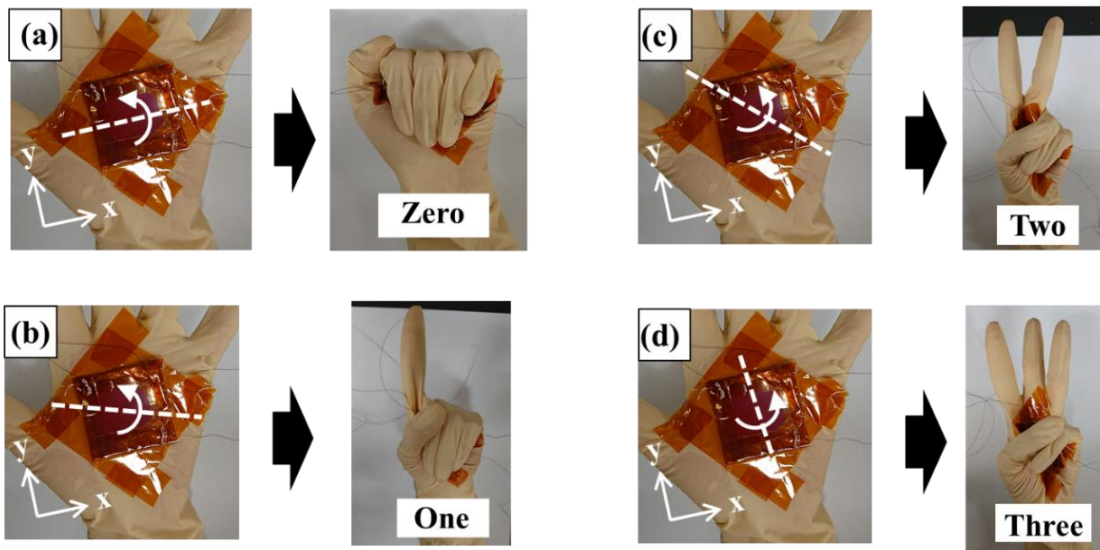


Figure 6.2.7. (a)-(d) Photograph of the integrated bending sensor attached on the palm of the hand and various hand gestures and (e) sensing curves of the integrated bending sensor under various hand gestures.

6.3 Flexible Photodetector based on Cu₂O/ZnO Films

6.3.1 Experiment

6.3.1.1 Fabrication of Flexible Cu₂O/ZnO Photodetector

A ZnO film was fabricated on a ITO coated PET substrate (40 mm × 30 mm × 0.125 mm) via the spin-spray method. Then, a Cu₂O film was fabricated on the ZnO/ITO/PET substrate by the spin-spray method. Chapter 2 and 5 provides more detail on the fabrication process of Cu₂O and ZnO films via the spin-spray method, respectively. The source solution and the reaction solution were prepared by using the mixed CuSO₄·5H₂O (0.04 M) and C₆H₈O₆ (0.04 M) solution and by dissolving NaOH (0.4 M) in NH₃ aq. (1.2 M) solution, respectively.

6.3.1.2 Performance and Characterization of Cu₂O/ZnO Photodetector

The Cu₂O/ZnO heterojunction film were tested as photodetector by tracking the current density voltage (J-V) curves and the time dependent self-powered photo-response at 1 V applied bias, under Xe light irradiation (1000 W) in air and at room temperature. The light illuminated the sample from the bottom, passing through the ITO/PET substrate. Electrical measurements were carried out by using a Keithley 2400 digital meter with the working electrode in contact with the top oxide layer. The crystallinity and microstructure of the samples were analyzed using XRD (Rint2000; Rigaku). The surface morphologies of the samples were examined using FESEM (HITACHI, Japan, S-4700).

6.3.2 Results and Discussion

6.3.2.1 Characterization of Flexible Cu₂O/ZnO Photodetector

From the I–V curves of tIn **Chapter 2** and **5**, Cu₂O and ZnO films were fabricated on glass substrate at low temperature below 90°C by the spin-spray method. Therefore, this method does not adversely affect the substrate, indicating that the flexible PET with low thermal durability can be utilized as substrates to fabricate flexible sensors. In this section, Cu₂O and ZnO films were fabricated on a ITO coated PET substrate by the spin-spray method for flexible photodetectors. **Figure 6.3.1 (a)** schematically depicts the structure of the fabricated Cu₂O/ZnO photodetector. A ZnO film fabricated on a flexible ITO/PET substrate by the spin-spray method. The fabricated ZnO film was subjected to UV irradiation for 60 min to improve the film resistivity. Then, a Cu₂O film was fabricated on the ZnO/ITO/PET by the spin-spray method. **Figure 6.3.1 (b)** and **(c)** showed the surface FESEM images of the ZnO/ITO/PET and the Cu₂O/ZnO/ITO/PET, respectively. As shown in **Figure 6.3.1 (b)**, ZnO nanorod (NR) array was fabricated on the ITO/PET substrate. Previous studies reported that ZnO films with and without citric acid in source solution during the spin-spray process possessed the dense film and NR array structure, respectively. To fabricate the ZnO film, citric acid was not used during the spin-spray process, and therefore, the sample structure was NR arrays, as shown in **Figure 6.8 (b)**. **Figure 6.8 (c)** showed that Cu₂O particles were evenly distributed on the surface of ZnO NRs and wrapped around the top of the nanorods. In general, it is difficult to coat complex structures such as NR array by conventional dry processes. In the spin-spray method, the liquid film was formed on the reaction field and the substrate was immersed into the liquid film. Therefore, Cu⁺ and OH⁻ ions can efficiently be attached to

the surface of NRs, resulting in the fabrication of the Cu₂O nanoparticle-wrapped ZnO NR array, as shown in **Figure 6.3.1 (c)**.

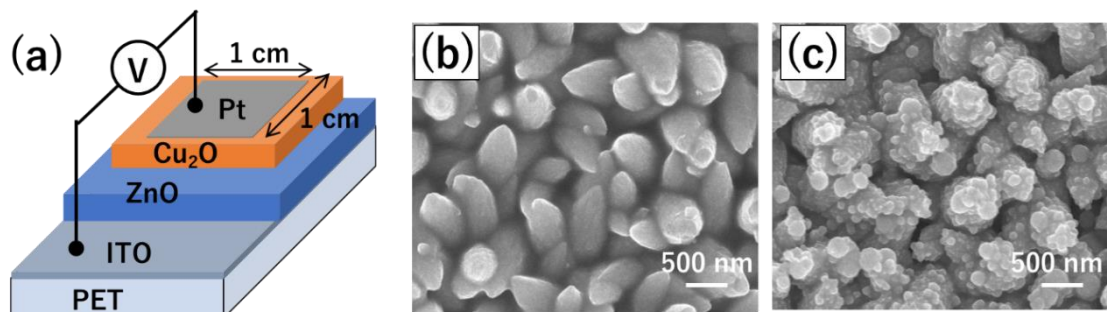


Figure 6.3.1 (a) Schematic illustration of the Cu₂O/ZnO heterojunction. (b) FESEM images of (b) the ZnO/ITO/PET and (c) the Cu₂O/ZnO/ITO/PET.

6.3.2.2 Performance as Flexible Cu₂O/ZnO Photodetector

From the I–V curves of the Cu₂O/ZnO/ITO/PET in the dark (**Figure 6.3.2 (a)**), it is clear that the as-fabricated Cu₂O/ZnO/ITO/PET shows typical rectification behavior, indicating the formation of p-type Cu₂O/n-type ZnO heterojunctions.¹⁸ The rising voltage of the Cu₂O/ZnO/ITO/PET was 0.7 V as shown in **Figure 6.3.2 (b)**. However, a high leakage current was measured due to the thin-thickness of the Cu₂O film. **Figure 6.3.2 (c) and (d)** showed the time dependent photo-response of the ZnO/ITO/PET and Cu₂O/ZnO/ITO/PET at 1 V, respectively. Apparently, the Cu₂O/ZnO/ITO/PET exhibited optimal performance, with photocurrents enhanced over a single ZnO. As shown **Figure 6.3.2 (c)**, the response and recovery times for the ZnO/ITO/PET are very slow, more than 10 s and more than 20 s, respectively. On the other hand, the Cu₂O/ZnO/ITO/PET showed enhanced response and recovery times below 4.7 s and 6.7 s, respectively (**Figure 6.3.2 (d)**). The underlying photo-response mechanism investigated in this work is depicted in **Figure 6.3.2 (e)**, showing the electronic band bending and the space-charge region, which provide the driving force to separate the excitons generated under illumination. The

energy gap and the band alignment play a crucial role in the photo-response mechanism.

I propose in **Figure 6.3.2 (e)** the $\text{Cu}_2\text{O}/\text{ZnO}$ junction scheme for conduction and valence band, in agreement with the present literature in the field.

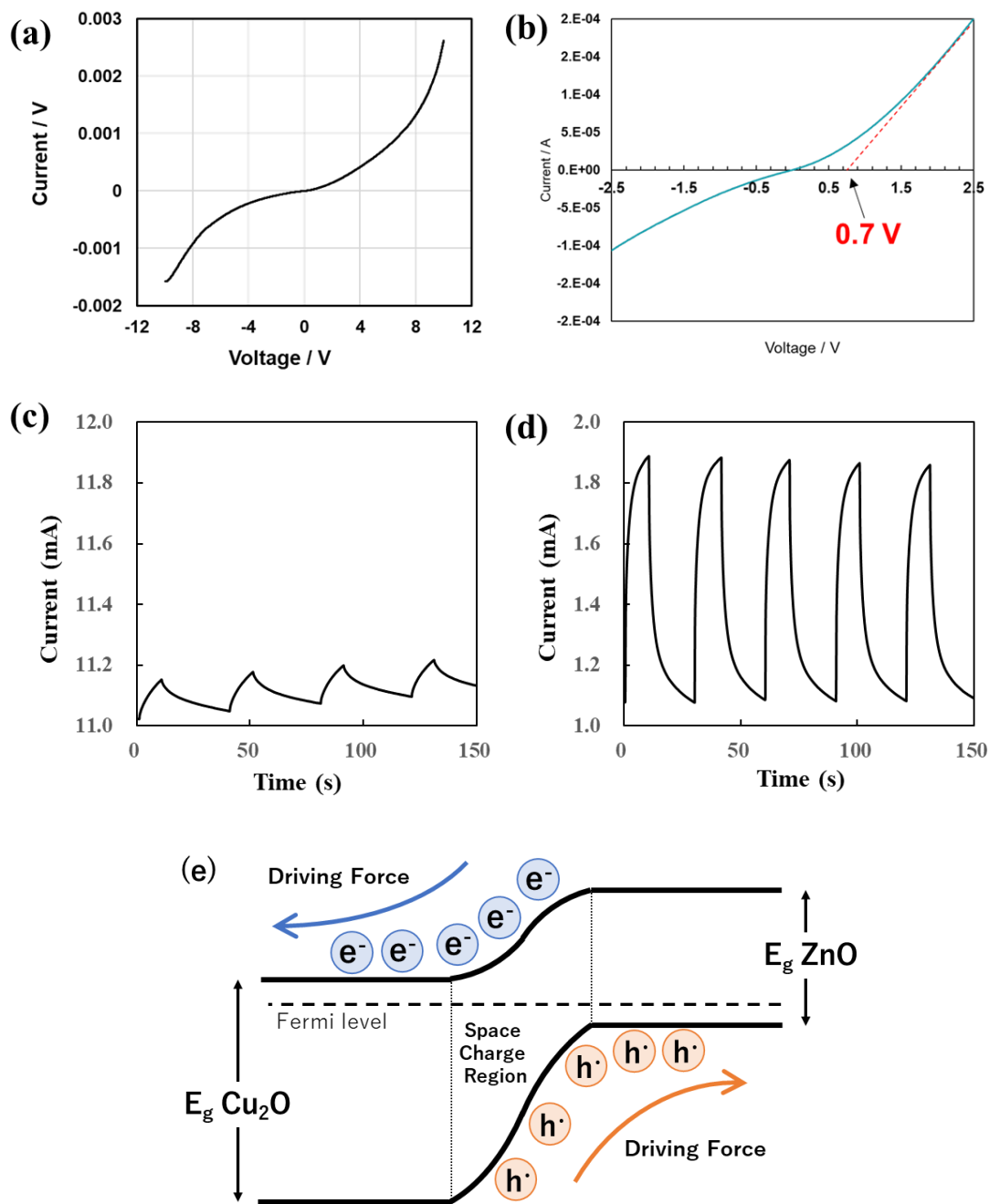


Figure 6.3.2 (a) the I–V curve and (b) the rising voltage of the $\text{Cu}_2\text{O}/\text{ZnO}/\text{ITO}/\text{PET}$ in the dark. The time dependent photo-response of (c) the $\text{ZnO}/\text{ITO}/\text{PET}$ and (d) the $\text{Cu}_2\text{O}/\text{ZnO}/\text{ITO}/\text{PET}$ at 1 V.

6.4 Flexible humidity sensor based on CuO nanostructures

6.4.1 Experiment

6.4.1.1 Fabrication of Flexible CuO Humidity Sensor

CuO films were fabricated on PET substrates ($30 \times 30 \times 0.17$ mm) via the spin-spray method. Chapter 4 provides more detail on the fabrication process of CuO films via the spin-spray method. The reaction solution was prepared using NaOH solution at pH 13. Two source solutions were prepared by dissolving 0.06 M $C_2H_8N_2$ or 0.06 M $C_6H_5Na_3O_7$ in 0.04 M $CuSO_4 \cdot 5H_2O$ solution. Samples fabricated on PET substrate using $C_2H_8N_2$ (EDA) and $C_6H_5Na_3O_7$ (Cit) are referred to as CuO-PET-EDA and CuO-PET-Cit, respectively. After fabrication, all samples were ultrasonically cleaned in deionized water to remove any surface contaminants. To fabricate the humidity sensors, two $2 \text{ mm} \times 2 \text{ mm}$ Au films separated by a distance of 10 mm were sputter coated on top of the samples to serve as contact electrodes, as shown in **Figure 6.4.1 (a)**.

6.4.1.2 Performance of Flexible CuO Humidity Sensor

The humidity-sensing performance of the samples was evaluated by measuring the electrical resistance with 5 V applied bias under various relative humidity (RH) conditions at room temperature (20 ± 1 °C). **Figure 6.4.1 (b)** shows the humidity measuring system which was developed to measure the humidity-sensing performance. The system consisted of a mass flow controller, chamber, hygrometer and the fabricated humidity sensor. The RH in the chamber was controlled by changing the ratio of dry and wet N_2 gases, as shown in **Figure 6.4.1 (b)**. The fabricated sensor was placed in the chamber and the resistance was recorded using an electrical source meter. The humidity response was defined as $\Delta R/R_0$ (%) = $(R_0 - R) / R_0 \times 100$, in which R and R_0 are the resistance under humid and ambient dry conditions at room temperature, respectively.

The response time and recovery time were defined as the times required to reach 90% of the final resistance value for water adsorption and desorption, respectively. The reliability of the sensing performance of CuO-PET-EDA against mechanical bending was evaluated by measuring the resistance with the various bending angle. The bending angle was defined as the angle between the straight line connecting the two ends of the sensor and the tangent line extending from the edge of the sensor.

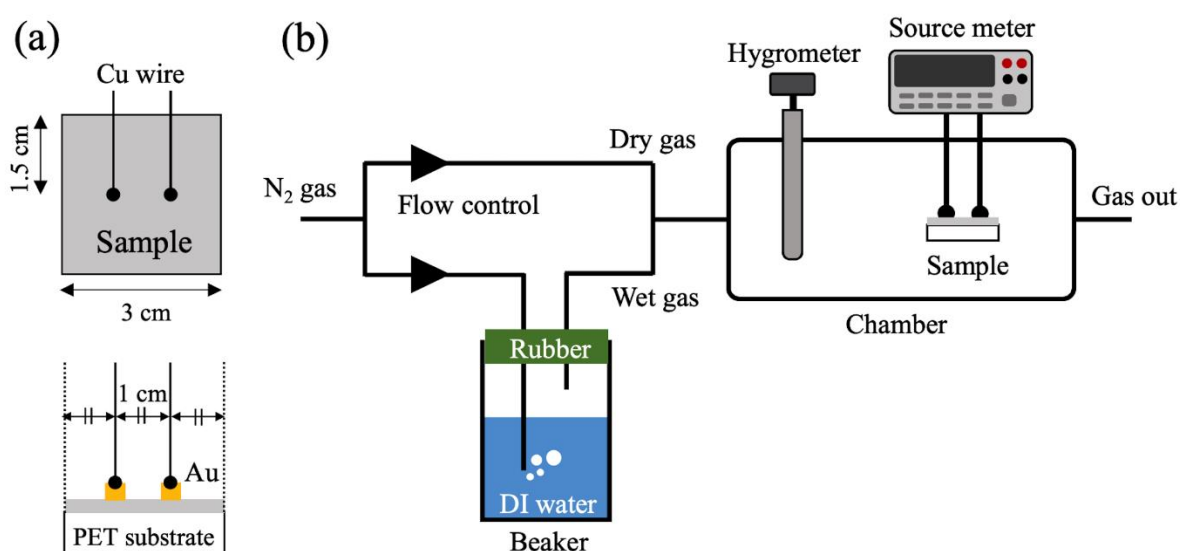


Figure 6.4.1 Schematic illustration of the (a) fabricated CuO humidity sensor and (b) humidity measuring system

6.4.1.3 Performance of Flexible CuO Humidity Sensor

The crystallinity and microstructure of the samples were analyzed using XRD (BRUKER Co., USA, D8 FOCUS/TXS). The surface morphologies of the samples were examined using FESEM (HITACHI, Japan, S-4700). XPS (Physical Electronics, Inc., USA, PHI 5000) was used to investigate the chemical states. The presence of impurities in the samples was confirmed using attenuated total reflection Fourier-transform infrared (ATR-FTIR) spectroscopy (FT-IR IRPrestige-21, Shimadzu Corp., Japan).

6.4.2 Results and Discussion

6.4.2.1 Characterization of Flexible CuO Humidity Sensor

In Chapter 3, CuO nanostructures of various shapes including carpet-like and grass-like arranged CuO nanosheets were fabricated on glass substrates at low temperature of 90°C by the spin-spray method using different complexing agents. In this section, nanostructured CuO films were fabricated on PET substrates by the spin-spray method for applications as flexible humidity sensors. Because this method does not adversely affect the substrate because of the low fabrication temperature (90°C) and a short deposition time (10 min), the fabrication could be achieved even on the flexible PET substrate with low thermal durability. The two samples via the spin-spray method using $C_2H_8N_2$ (EDA) and $C_6H_5Na_3O_7$ (Cit) on the PET substrates were referred as CuO-PET-EDA and CuO-PET-Cit, respectively.

Figure 6.4.2 (a) and (b) shows that CuO-PET-EDA and CuO-PET-Cit were deposited uniformly on the PET substrate and appeared dark gray and black, respectively. The resulting films exhibited strong adhesion to the substrate without peeling off, even after ultrasonication at 45 kHz of 200 W in deionized water for 10 min. It is important for the fabrication of metal oxide films by the spin-spray method to increase the hydrophilicity of the substrate surface by the plasma treatment before the film fabrication. There were a large number of polar functional groups such as carbonyl, hydroxyl, and aldehyde/ketone ($-COOH$, $-OH$, and $-CO$), on the surface of the PET substrate due to the hydrophilicity caused by plasma treatment.⁷ The formed crystal nuclei of CuO due to heterogeneous nucleation were chemically bonded to the functional groups on the substrate surface and grew to form a CuO film, as indicated in equations (6)-(8). Therefore, the film fabricated by the spin-spray method exhibited strong adhesion to the

substrate. **Figure 6.4.2 (c)** shows that the film was sufficiently flexible to be used in bent conditions. Flexible humidity sensors were fabricated by using the samples as shown in **Figure 6.4.2 (d)**. XRD patterns of CuO-PET-Cit and CuO-PET-EDA showed peaks characteristic of the monoclinic phase of CuO with good accordance to the ICDD data (JCPDS 48-1548), as shown in **Figure 6.4.2 (e)**. No impurity peaks from Cu(OH)₂ Cu₂O, ethylenediamine or trisodium citrate were observed. These results of CuO-PET-EDA and CuO-PET-Cit were similar to those of CuO-Glass-EDA and CuO-Glass-Cit prepared in chapter 3.

The performance of gas sensors such as humidity sensors is significantly influenced by the surface characteristics of the sensing materials. To clarify the chemical state of the sample surface, the XPS were carried out and the results were shown in **Figure 6.4.2 (f)**. **Figure 6.4.2 (f)** shows XPS spectra of the Cu2p region for CuO-PET-Cit and CuO-PET-EDA. The peaks at 933.4 eV and 953.2 eV were attributed to Cu2p_{3/2} and Cu2p_{1/2}, respectively, indicating the presence of Cu²⁺.¹⁹ Satellite peaks were observed at 940–945 eV and 961.8 eV, further confirming that the samples were CuO.²⁰ These results were in good agreement with the XRD patterns in **Figure 6.4.2 (e)** showing CuO as the sole phase. **Figure 6.4.2 (g)** shows XPS spectra of the O1s region for CuO-Cit and CuO-EDA. The O1s spectrum of CuO-EDA could be fitted to two peaks with binding energies at 529.7 eV and 531.1 eV, which were attributed to oxygen in CuO and Cu(OH)₂, respectively.²¹ The O1s spectrum of CuO-Cit could be fitted to three peaks at 529.7 eV, 531.3 eV and 532.7 eV, with the latter corresponding to O in water molecules confirming that CuO-Cit was in hydrated form.²²⁻²⁵ Water molecules were strongly adsorbed on the CuO-Cit surface, despite the sample having been dried at 60 °C for 12 h before XPS measurement.

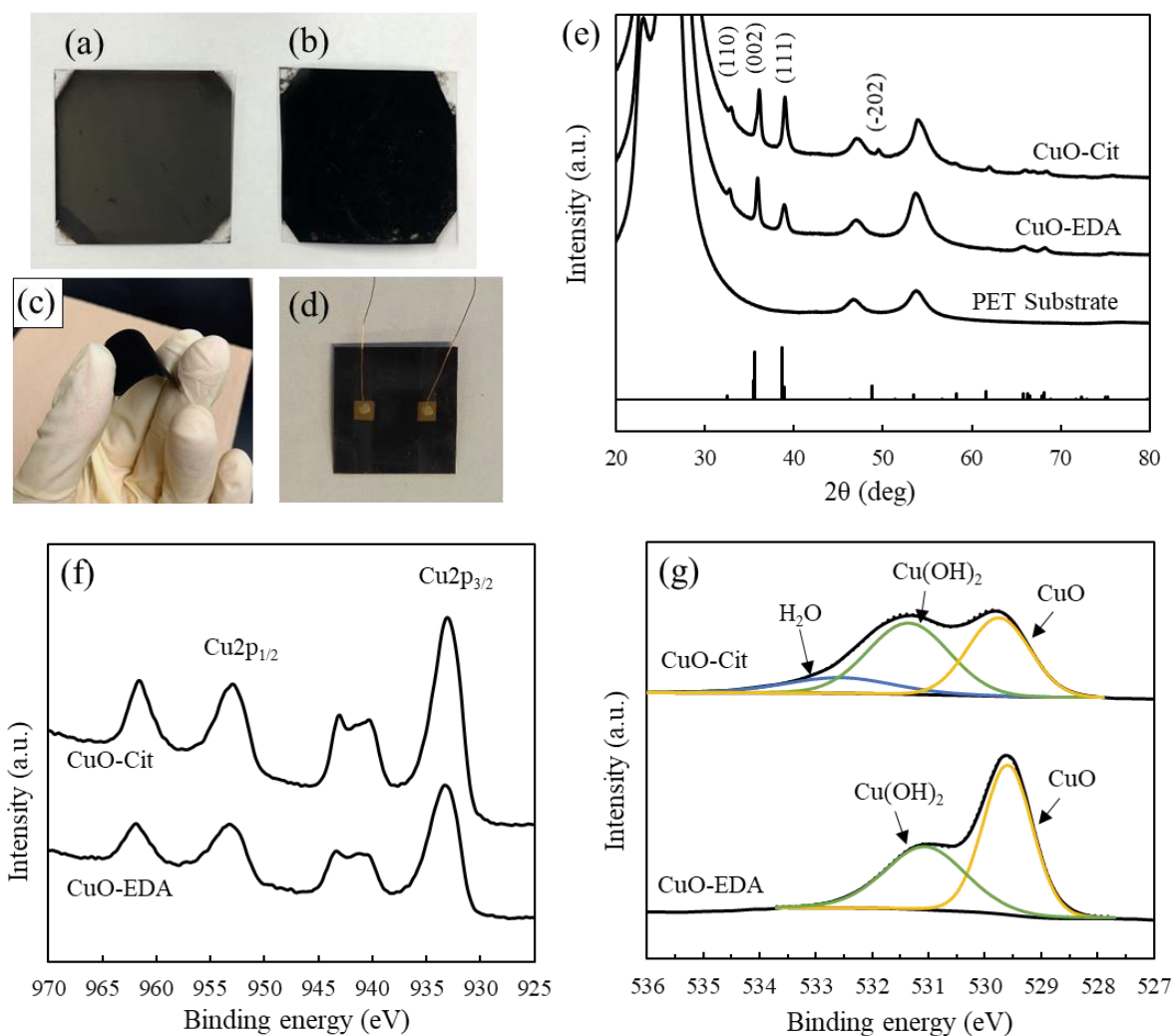


Figure 6.4.2 Digital photos of (a) CuO-PET-Cit, (b) CuO-PET-EDA, (c) CuO-PET-EDA in a bent state and (d) the humidity sensor based on CuO-PET-EDA. (e) XRD patterns of CuO-PET-Cit, CuO-PET-EDA and the PET substrate. XPS spectra of the (f) Cu 2p and (g) O 1s regions for CuO-PET-Cit and CuO-PET-EDA.

6.4.2.2 Morphological Characterization of Flexible Humidity Sensors

Figure 6.4.3 shows surface and cross-sectional FESEM images of CuO-PET-Cit and CuO-PET-EDA. CuO-PET-Cit was composed of nanosheet clusters and the substrate surface was fully covered with these clusters to forming a carpet-like morphology, as shown in **Figure 6.4.3 (a)**. The magnified image in **Figure 6.4.3 (b)** shows that tiny

multilayered nanosheets, 170 nm in lateral direction and 35 nm in thickness, accumulated with their sheet surfaces orientated parallel to the substrate. These nanosheet clusters aggregated to each other to form a dense film structure in the thickness direction, as shown in **Figure 6.4.3 (c)**. **Figure 6.4.3 (d)** and **(e)** show that the surface of CuO-PET-EDA was composed of nanosheets having a high aspect ratio, i.e. 2 μm in the lateral direction and 20 nm in thickness. These nanosheets, not aggregated but sparsely located, grew vertically on the substrate forming a grass-like nanosheet array, as shown in **Figure 6.4.3 (f)**. As shown in **Figure 6.4.3** and **6.4.3**, the morphologies of the CuO-PET-Cit and CuO-PET-EDA were very similar to those of CuO-Glass-Cit and CuO-Glass-EDA. Therefore, their formation mechanism can be explained according to chapter 3.

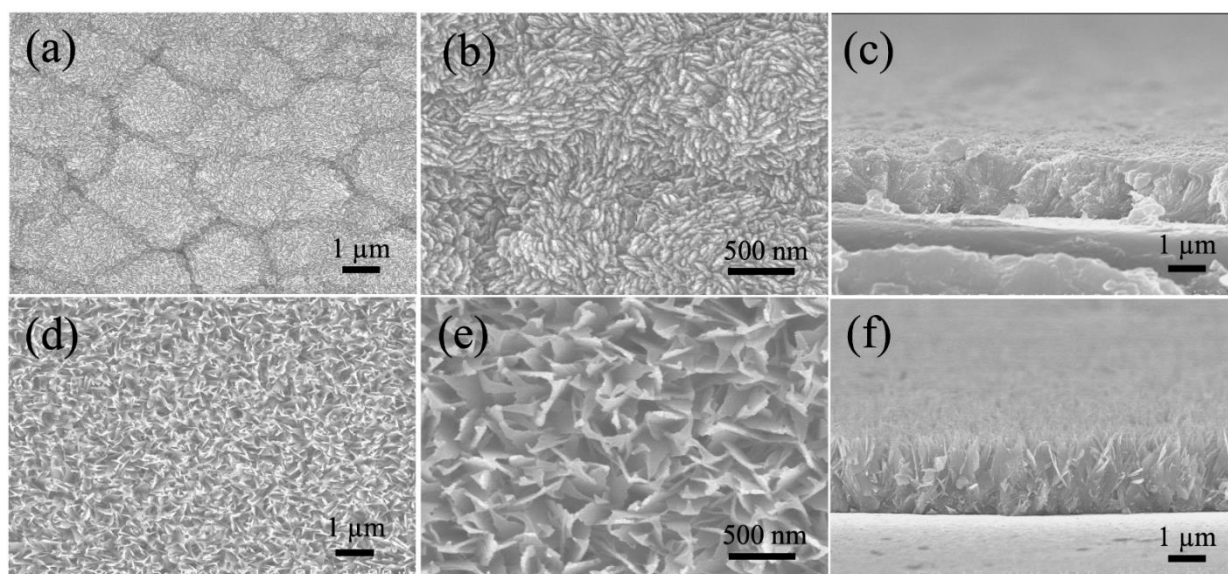


Figure 6.4.3 Surface and cross-sectional FESEM images of (a)–(c) CuO-PET-Cit and (d)–(f) CuO-PET-EDA.

6.4.2.3 Performance as Flexible Humidity Sensors

Figure 6.4.4 (a) shows the humidity response ($\Delta R/R_0$) of CuO-Cit and CuO-EDA at 20–90% RH at room temperature. The operating temperature was set below 100°C due to PET substrate with low thermal durability. R_0 of CuO-PET-Cit and CuO-PET-EDA were 423 M Ω and 58.2 M Ω , respectively. The response of CuO-PET-Cit changed little with RH, indicating that CuO-PET-Cit did not act as a humidity sensor. CuO-PET-EDA showed a high response of about 170% to the change in RH, even though the response was evaluated by the resistance change between two contact electrodes. These results indicated the selective sensing of humidity by adjusting the morphology of CuO nanostructures. The sensing test for five samples was carried out and all of them showed similar sensor characteristics, indicating the good reproducibility for all samples. The humidity response of CuO-PET-EDA with RH was fitted as a linear function, as shown in **Figure 6.4.4 (a)**. These results demonstrated that CuO-EDA showed a linear increment upon changing the RH. The linear function was modeled as: $\Delta R/R_0 (\%) = 5.318 + 1.951RH$ and the regression coefficient (R^2) was 0.9812, indicating that the good linear response in the entire RH range. The hysteresis characteristic is an important parameter for evaluating the accuracy and efficiency of the sensor. **Figure 6.4.4 (b)** shows the hysteresis characteristic curve of CuO-EDA. It is found that the humidity hysteresis curve exhibits a very narrow hysteresis loop. The maximal humidity hysteresis is calculated to be about 4 % RH at 70% RH, indicating a good reliability of the humidity sensor. **Figure 6.4.4 (c)** shows the repeatability of CuO-EDA between 20 and 70% RH over three cycles, which indicated that CuO-EDA possessed good repeatability and stability for RH monitoring. **Figure 6.4.4 (d)** shows the time-dependent adsorption response curve (from 20 to 70% RH) and desorption recovery curve (from 70 to 20% RH) of CuO-EDA. The

response and recovery times were 2.1 s and 2.8 s, respectively. CuO-EDA possessed faster response and recovery times than various reported humidity sensor.²⁶⁻³⁰

The humidity-sensing mechanism of p-type semiconductors such as CuO can be explained by the adsorption and desorption of oxygen molecules.³¹ Under dry conditions at room temperature, oxygen molecules adsorbed on the CuO surface trap electrons, which leads to an increase in the hole density of CuO. This decreases the resistance of CuO. As the RH increases, adsorbed oxygen molecules are substituted by water molecules on the CuO surface. Trapped electrons are released back into CuO, so the resistance increases. This mechanism well matches the repeatable response profile in **Figure 6.4.4 (a)**. CuO-Cit did not show any humidity response, as shown in **Figure 6.4.4 (a)**. This was attributed to a difference in the degree of water adsorption. A large number of (111) were exposed on the CuO-Cit surface, as described in section 3.2. Yu et al. reported that water molecules adsorbed on the CuO (111) dissociated into H and OH species and that the surface was covered with OH groups.³² Water molecules were chemisorbed by OH groups on the CuO (111), and could not desorb even at high temperature under vacuum conditions. **Figure 6.4.4 (f)** shows that water molecules remained on the surface of CuO-PET-Cit even under a vacuum condition during the XPS measurement. These results suggested that water molecules absorbed on the surface in wet condition did not readily desorb from the surface even under dry conditions, indicating that the amount of absorbed water molecules was little changed between dry and wet conditions. Therefore, CuO-PET-Cit did not respond to a change in RH. CuO-PET-EDA contained non-aggregated CuO nanosheets orientated perpendicular to the substrate and separated by several hundreds of nm or more, so had a very large surface

area. Nanosheets were approximately 20 nm in thickness and the surface-to-volume ratio was high, which promoted the humidity sensor performance.

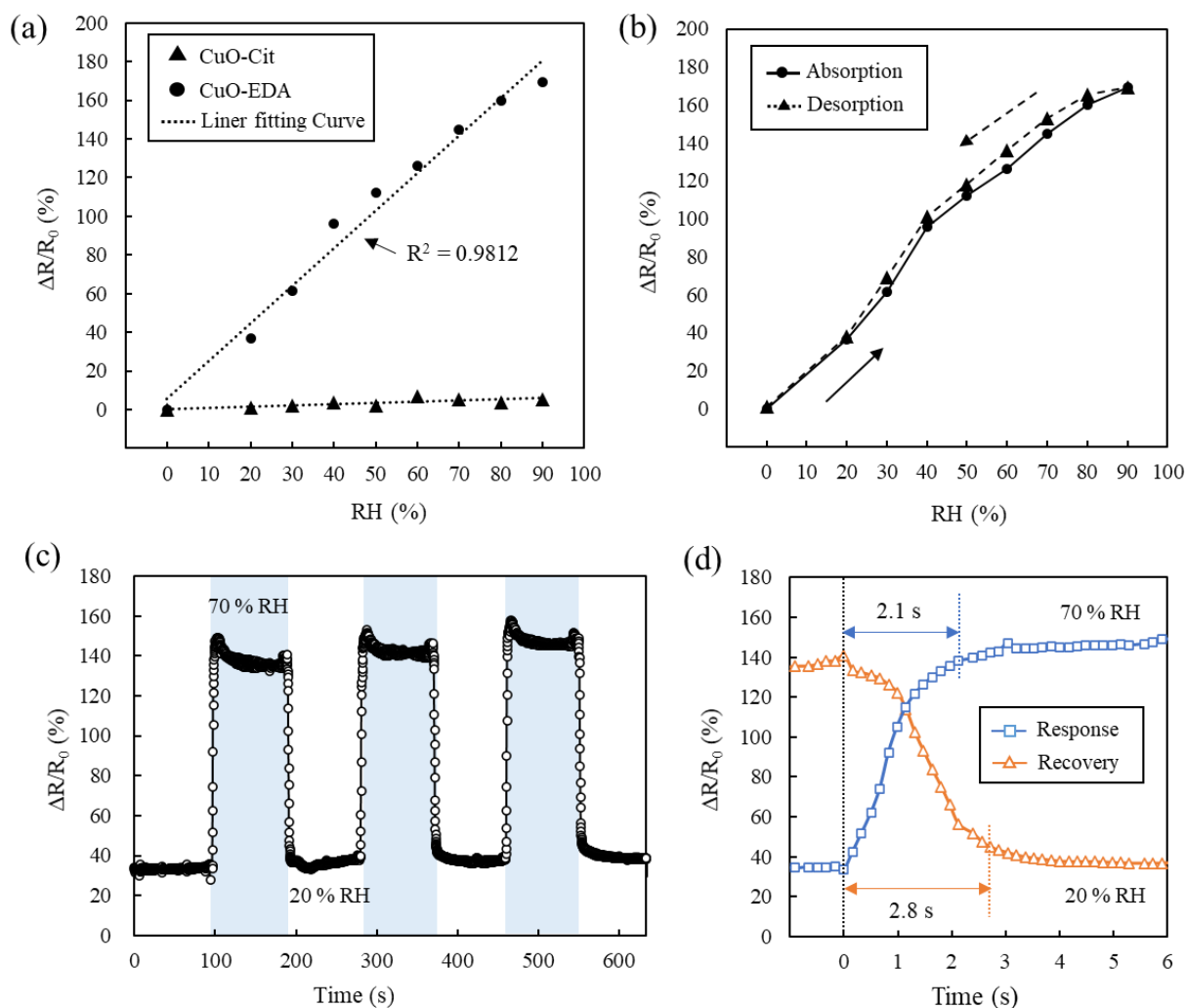


Figure 6.4.4 (a) Humidity responses of CuO-PET-Cit and CuO-PET-EDA as a function of RH. (b) Hysteresis characteristic curve of CuO-PET-EDA. (c) Repeatability and (d) response and recovery times of CuO-PET-EDA between 20% and 70% RH.

CuO-PET-EDA exhibited high sensitivity even in a bent state. The reliability of the sensing performance of CuO-PET-EDA against mechanical bending was evaluated by measuring the resistance with the bending angle (θ) fixed at 60° and 90° , as shown in **Figure 6.4.5 (a)**. **Figure 6.4.5 (c)** shows time-dependent response and recovery curves

for CuO-PET-EDA fixed at various bending angles. The sensitivities of the sample fixed at 60° and 90° were almost the same as that when flat. This demonstrated that the performance of the CuO-EDA sensor was stable against mechanical bending. To further investigate the capability of the CuO-PET-EDA sensor against mechanical fatigue, CuO-PET-EDA was repeatedly bent and relaxed. **Figure 6.4.5 (b)** shows a schematic of the bending-relaxation process. The flat sample was bent until the bending angle reached 90° and then returned to the flat state. This process was defined as one cycle. **Figure 6.4.5 (d)** shows time-dependent response and recovery curves after 0 (without bending), 500 and 1000 cycles. Even after 1000 cycles, there was almost no difference in humidity sensitivity performance.

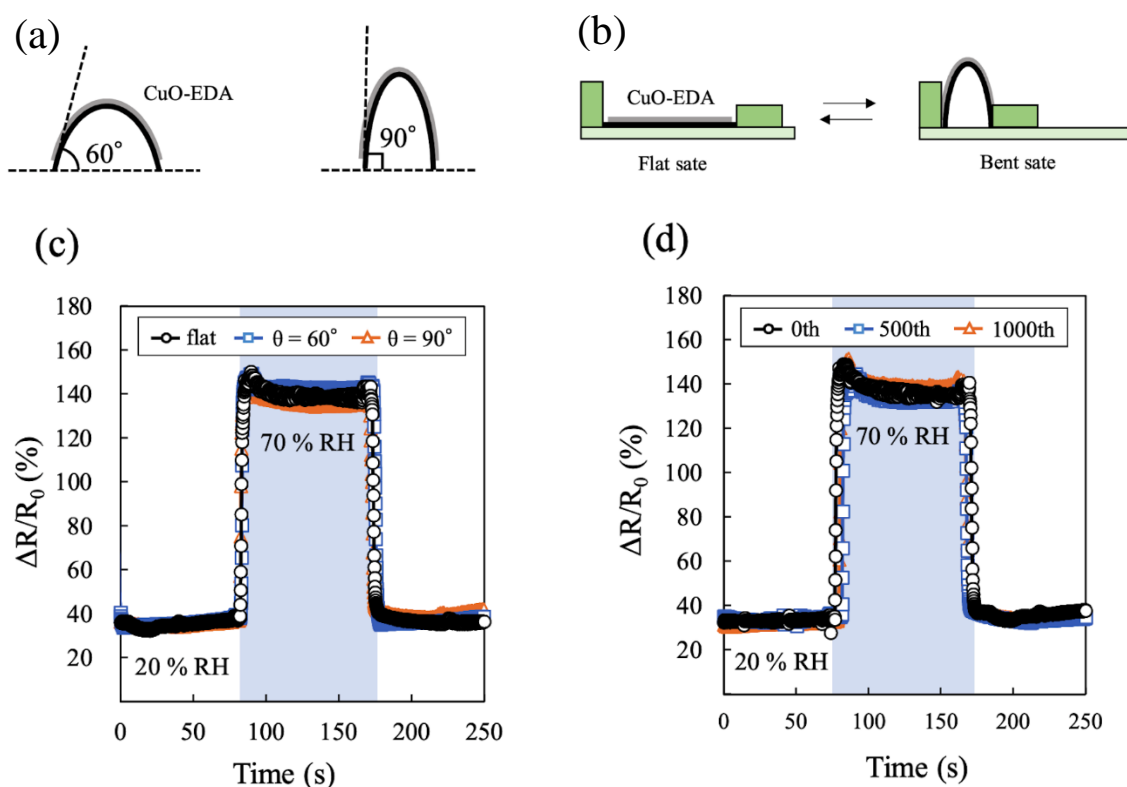


Figure 6.4.5 (a) Schematic illustration of CuO-PET-EDA with the bending angle fixed at 60° and 90° . **(b)** Schematic illustration of the bending-relaxation process and time-dependent response and recovery curves of CuO-PET-EDA between 20% and 70% RH for **(c)** different bending angles and **(d)** multiple bending-relaxing cycles.

Figure 6.4.6 shows surface FESEM images of CuO-PET-EDA and CuO-PET-Cit after 1000 cycles. Propagating cracks were observed on the CuO-PET-Cit surface, as shown in **Figure 6.4.6 (a)** and **(b)**. Generally, SMOs such as CuO-PET-Cit have low durability against bending due to their hard nature. On the other hands, no cracks were observed on the CuO-PET-EDA surface in which CuO nanosheets grew sparsely and vertically on the substrate, as shown in **Figure 6.4.6 (c)**. Besides, no cracks were also observed on each nanosheet, as shown in **Figure 6.4.6 (d)**. Cracks did not readily propagate in CuO-PET-EDA because the nanosheets were not aggregated but sparsely located on the substrate. CuO nanosheet arrays orientated perpendicular to the substrate such as in CuO-PET-EDA are therefore promising materials for flexible humidity sensors, because of their high sensitivity, rapid response and robust durability.

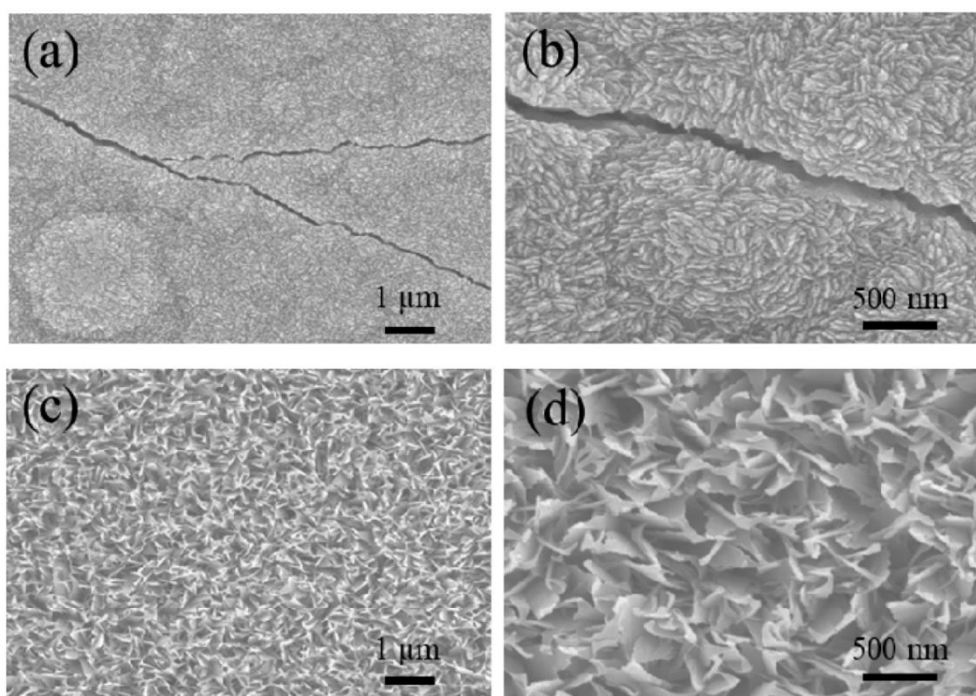


Figure 6.4.6 Surface FESEM images of **(a, b)** CuO-PET-Cit and **(c, d)** CuO-PET-EDA after 1000 bending-relaxation cycles.

6.5 Flexible glucose sensor based on CuO Thin Film

6.5.1 Experiment

6.5.1.1 Fabrication, Performance and Characterization of Flexible CuO Glucose Sensor

A CuO thin film was fabricated on ITO/PET substrates (40 mm × 30 mm × 0.125 mm) via the MSS method. Chapter 5 provides more detail on the fabrication process of CuO films via the spin-spray method. The source solution and the reaction solution were prepared by using the mixed $\text{CuSO}_4 \cdot 5\text{H}_2\text{O}$ (0.04 M) and NH_3 aq. (1.5 M) solution and the NaOH (0.1 M) solution, respectively. Electrochemical measurements were carried out in the electrode setup using CuO/ITO/PET samples as the working electrodes, with platinum as a counter electrode, and a saturated Ag/AgCl electrode as the reference electrode. A 0.1 M NaOH solution was used as the electrolyte for electrochemical measurements with a cyclic voltammetry (CV) and the linear sweep voltammetry (LSV) recorded using an electrochemical workstation (Hokuto Denko Co., HZ-7000). The crystallinity and microstructure of the samples were analyzed using XRD (Rint2000; Rigaku). The surface morphologies of the samples were examined using FESEM (HITACHI, Japan, S-4700).

6.5.2 Results and Discussion

6.5.2.1 Characterization of Flexible CuO Glucose Sensor

A CuO thin film was fabricated on In chapter 4, CuO thin films were fabricated on glass substrates at low temperature of 90°C by the mis spin spray (MSS) method. In this section, a CuO thin film was fabricated on the ITO/PET substrate by the MSS method for a flexible glucose sensor. The sensor was sufficiently flexible to be used in bent conditions, as shown in **Figure 6.5.1 (a)**. **Figure 6.5.1 (b)** shows the FESEM image of the sensor. The outer surface of the sensor was found to be uniform and it was evident

that the CuO thin film fully covered the ITO/PET substrate. As shown in **Figure 6.5.1 (c)**, the XRD peaks corresponded to the cubic phase of CuO with good accordance to the ICDD data (JCPDS 48-1548) in addition to ITO and PET peaks without the presence of impurity peaks from Cu(OH)₂ or Cu₂O.

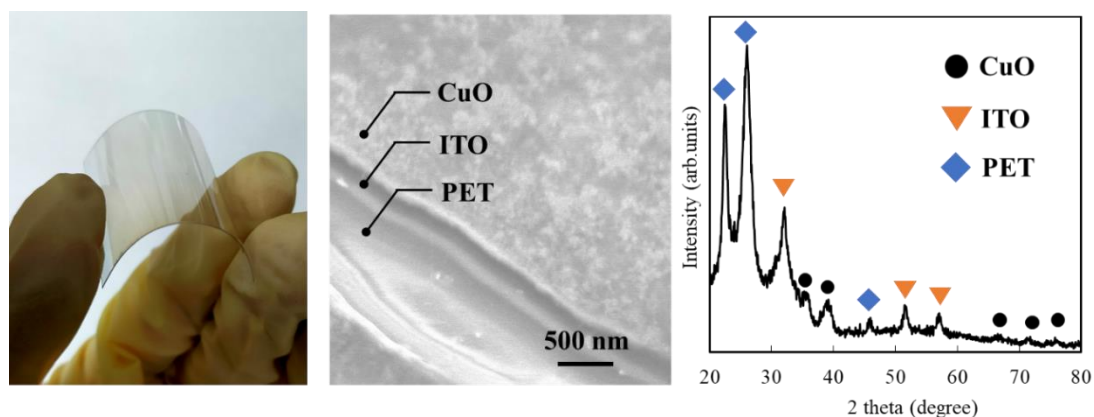
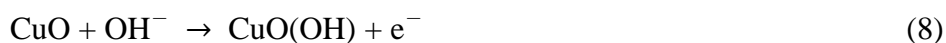


Figure 6.5.1 (a) Photograph, (b) FESME image (c) XRD pattern of the CuO glucose sensor.

6.5.2.2 Characterization of Flexible CuO Humidity Sensor

The CV technique was used to assess the behavior of the CuO/ITO/PET electrode for electrocatalytic oxidation of glucose. As shown in **Figure 6.5.2 (a)**, the bare ITO/PET electrode does not show any oxidation or reduction current in the absence of glucose in the limited potential window. Besides, its electrochemical response to glucose is low as shown in **Figure 6.5.2 (b)**. For the CuO/ITO/PET electrode, however, a single broad reduction peak with a peak potential of about +0.56 V can be observed in the absence of glucose, which should correspond to a Cu(II)/Cu(III) redox couple.³³ The chemical reaction taking place in the absent of glucose can be described in eq. 8.³⁴



With the addition of 5.0 mM glucose, a greatly enhanced catalytic oxidation current is observed in the range of +0.25 V to +0.70 V on the CuO/ITO/PET electrode. Copper (III)

has been proposed to have the tendency to facilitate the transfer of electron during the oxidation process of glucose to gluconolactone, as seen in eq. 9.²⁴



The result in **Figure 6.5.2 (a)** showed that the CuO/ITO/PET electrode display enhanced electrocatalytic activity toward glucose oxidation, compared to the bare ITO/PET electrode.

Figure 6.5.3 (a) shows the amperometric response of the CuO/ITO/PET electrode to successive addition of glucose at applied potential of +0.5 V. The CuO/ITO/PET electrode responded rapidly to the changes in glucose concentration. As shown in **Figure 6.5.3 (b)**, the current response curve of the CuO/ITO/PET electrode with the glucose concentration (C) can be divided into two linear parts, which are region I ($0 < C < 0.3 \text{ mM}$) and II ($0.3 < C < 1.3 \text{ mM}$) with the regression coefficient (R^2) of 0.9934 and 0.9748, respectively. The high linearity shows that the CuO glucose sensor possesses excellent sensing properties. All these indicated that the proposed electrode fabrication process is appropriate and satisfactory for non-enzymatic glucose sensing application.

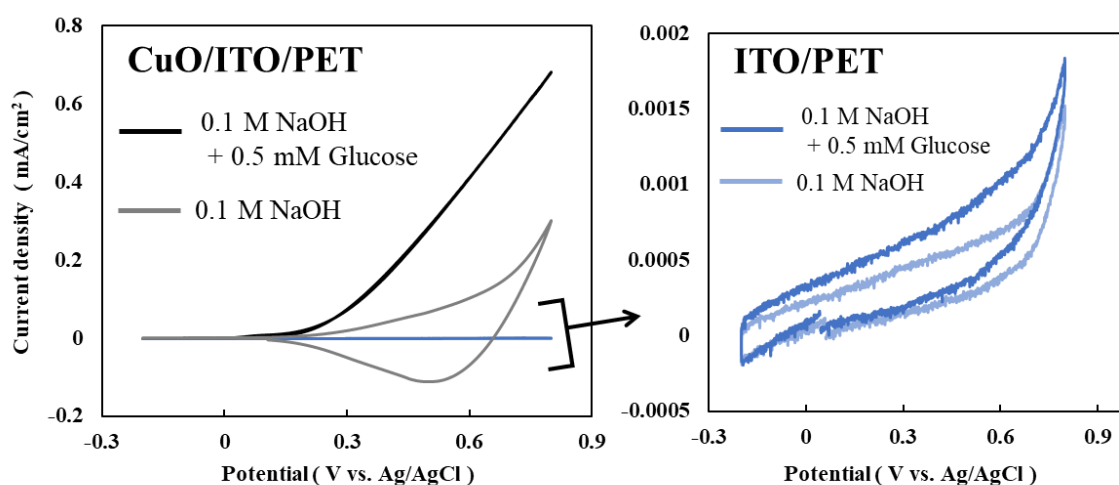


Figure 6.5.2 CV curves of (a) CuO/ITO/PET electrode and (b) ITO/PET electrode in 0.1 M NaOH without and with 5 mM Glucose at 100 mVs^{-1} .

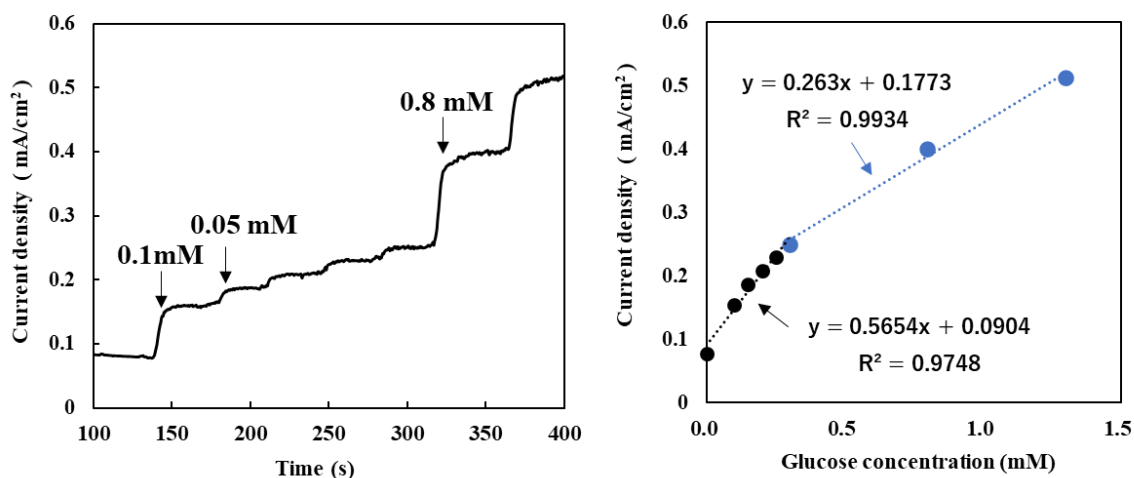


Figure 6.5.3 (a) Amperometric current response and **(b)** the dependence of the current response vs. glucose concentration of the CuO/ITO/PET electrode.

6.6 Conclusion

Cu₂O, CuO and ZnO films were fabricated on PET substrates for flexible sensors by the spin-spray method and MSS method. The performance of the flexible sensors based on these metal oxide films is as follows.

The Cu₂O film fabricated on the PET substrate was employed as a flexible bending sensor, and its bending performance was evaluated by measuring the electrical resistance between the electrodes under various curvatures. The Cu₂O bending sensor showed high sensitivity and high resolution not only over a wide range of curvatures ($0 < \kappa < 0.21 \text{ mm}^{-1}$) but also for very small curvature changes ($\Delta\kappa = \sim 0.03 \text{ mm}^{-1}$) when bending parallel to the direction of the current flow. In addition, the sensor possessed high linearity with a high GF (21.8) and mechanical fatigue durability (1000 bending–release cycles). On the other hands, the resistance variation changed little in the perpendicular bending, indicating that the Cu₂O bending sensor showed the excellent anisotropic bending performance All of these excellent sensing characteristics indicate the

applicability of the sensor for detailed monitoring of large- and small-scale human motions, such as finger bending, wrist bending, nodding, mouth opening/closing, and swallowing. Besides, the anisotropic bending performance endows the Cu₂O bending sensor the potential ability to monitor not only simple motions such as the bending and stretching, but also complicated human body motions, such as various hand gestures. Given its numerous advantages, the Cu₂O bending sensor has broad application prospects for future wearable electronics.

A Cu₂O/ZnO heterojunction was fabricated on a ITO coated PET substrate by the spin-spray method for a flexible photodetector. The Cu₂O/ZnO showed rectification behavior, indicating the formation of p-type Cu₂O/n-type ZnO heterojunctions. The flexible Cu₂O/ZnO junction photodetector showed the typical photoelectric performance, and the response and recovery times below 4.7 s and 6.7 s, respectively.

Grass-like arrays and dense carpet-like films of CuO nanosheets were fabricated on PET substrates via the spin-spray method using different complexing agents. The resulting films on the PET substrates were applied as flexible humidity sensors. The humidity-sensing properties were investigated by measuring the electrical resistance from 20 to 90% RH at room temperature. The sensor based on the dense carpet-like CuO film did not exhibit any humidity response, indicating that it had high stability against humidity changes. The grass-like CuO nanosheet array possessed excellent humidity-sensing performance, including high sensitivity, good repeatability and fast response/recovery characteristics, because of its high surface area and surface-to-volume ratio. The sensor based on the CuO nanosheet array showed reliability and durability against mechanical bending because the nanosheets were not aggregated but instead

located sparsely on the substrate. The CuO nanosheet array therefore has potential as a sensing material for high-performance flexible humidity sensors.

The CuO thin film was fabricated on the ITO/PET substrate for a flexible glucose sensor by the MSS method. The sensor shows the high linearity over a wide detection range to glucose. Moreover, the proposed as-developed solution-based approach utilized in this work could be used for sizeable and efficient wide-range electrode production.

In conclusion, the spin-spray method and MSS method can be applied to fabricate metal oxide films on PET substrates with low thermal durability for flexible sensor applications due to their low fabrication temperature below 100°C and high deposition rate which allows a short deposition time. In addition, the metal oxide films fabricated by these methods exhibited good adhesion to PET substrates, and therefore, they were sufficiently flexible to be used in bent conditions. Metal oxide film-based flexible sensors with high sensing performance and mechanical fatigue durability were fabricated by optimizing the particle size, film thickness, and film morphology through controlling the spin spray reaction.

References

- [1] Y. Wei, S. Chen, F. Li, Y. Lin, Y. Zhang, L. Liu, *ACS Appl. Mater. Interfaces*. 7 (2015) 14182–14191.
- [2] S. Kim, M. Amjadi, T.-I. Lee, Y. Jeong, D. Kwon, M.S. Kim, K. Kim, T.-S. Kim, Y.S. Oh, I. Park, *ACS Appl. Mater. Interfaces*. 11 (2019) 55.
- [3] B. Sun, Y.Z. Long, S.L. Liu, Y.Y. Huang, J. Ma, H. Di Zhang, G. Shen, S. Xu, *Nanoscale*. 5 (2013) 7041–7045.
- [4] V.K. Samoei, A.H. Jayatissa, *Sensors Actuators, A Phys.* 303 (2020) 111816.
- [5] C. Dong, Y. Fu, W. Zang, H. He, L. Xing, X. Xue, *Appl. Surf. Sci.* 416 (2017) 424–431.
- [6] W. Deng, T. Yang, L. Jin, C. Yan, H. Huang, X. Chu, Z. Wang, D. Xiong, G. Tian, Y. Gao, H. Zhang, W. Yang, *Nano Energy*. 55 (2019) 516–525.
- [7] A. Vesel, I. Junkar, U. Cvelbar, J. Kovac, M. Mozetic, *Surf. Interface Anal.* 40 (2008)
- [8] S. Poulston, P.M. Parlett, P. Stone, M. Bowker, *Surface and Interface Analysis*. 24 (1996) 811.
- [9] R.K. Swarnkar, S.C. Singh, R. Gopal, *Bull. Mater. Sci.* 34 (2011) 1363–1369.
- [10] J.Y. Chen, P.J. Zhou, J.L. Li, S.Q. Li, *Carbohydr. Polym.* 67 (2007) 623–629.
- [11] A.H.B. Dourado, A.G.M. da Silva, F.A.C. Pastrían, R.L. Munhos, A.P. de Lima Batista, A.G.S. de Oliveira-Filho, J. Quiroz, D.C. de Oliveira, P.H.C. Camargo, S.I. Córdoba de Torresi, *J. Catal.* 375 (2019) 95–103.
- [11] K. Kuwahara, R. Taguchi, M. Kishino, N. Akamatsu, K. Tokumitsu, A. Shishido, *Appl. Phys. Express*. 13 (2020).
- [12] M. Emadi, M. A. Zare, O. Moradlou, M. Iranpour, *J. Phys. Chem. Electrochem.* 22 (2014) 87–92.
- [13] R. Taguchi, N. Akamatsu, K. Kuwahara, K. Tokumitsu, Y. Kobayashi, M. Kishino, K. Yaegashi, J. Takeya, A. Shishido, (2021).
- [14] Y. Sun, S.E. Thompson, T. Nishida, *J. Appl. Phys.* 101 (2007).
- [15] A.S. Fiorillo, C.D. Critello, A.S. Pullano, *A Phys.* 281 (2018) 156–175.
- [16] P. Kleimann, B. Semmache, M. Le Berre, D. Barbier, *Phys. Rev. B - Condens. Matter Mater. Phys.* 57 (1998) 8966–8971.
- [17] R. Taguchi, K. Kuwahara, N. Akamatsu, A. Shishido, *Soft Matter*. 17 (2021) 4040–4046.
- [18] S. Zhong, D. Xiong, B. Zhang, X. Yang, T. Yang, G. Tian, H. Zhang, W. Yang, W. Deng, (2022).

- [19] M.A. Dar, Q. Ahsanulhaq, Y.S. Kim, J.M. Sohn, W.B. Kim, H.S. Shin, *Appl. Surf. Sci.* 225 (2009) 6279-6284.
- [20] Z. Hong, Y. Cao, J. Deng, *Mater. Lett.* 52 (2002) 34-38.
- [21] O. Akhavan, R. Azimirad, S. Safa, E. Hasani, *J. Mater. Chem.* 21 (2011) 9634-9640.
- [22] X. Han, F. Liao, Y. Zhang, C. Xu, H. Chen, *Mater. Lett.* 214 (2018) 138-141.
- [23] Y. Hsu, Y. Chen, Y. Lin, *J. Electroanal. Chem.* 673 (2012) 43-47.
- [24] D.C. Look, J.W. Hemsky, J.R. Sizelove, *Phys. Rev. Lett.* 82 (1999) 2552-2555.
- [25] D.P. Dubal, G.S. Gund, R. Holze, C.D. Lokhande, *J. Power Sources.* 242 (2013) 687-698.
- [26] Z. Duan, Y. Jiang, M. Yan, S. Wang, Z. Yuan, Q. Zhao, P. Sun, G. Xie, X. Du, H. Tai, *ACS Appl. Mater. Interfaces.* 11 (2019) 21840-21849.
- [27] Z. Duan, Y. Jiang, Q. Huang, S. Wang, Y. Wang, H. Pan, Q. Zhao, G. Xie, X. Du, H. Tai, *Smart Mater. Struct.* 30 (2021).
- [28] S. Ashokana, P. Jayamuruganb, V. Ponnuswamy, *Polymer Science, Series B* 61 (2019) 86-07.
- [29] S. Zhong, D. Xiong, B. Zhang, X. Yang, T. Yang, G. Tian, H. Zhang, W. Yang, W. Deng, (2022).
- [30] Z. Wang, Y. Xiao, X. Cui, P. Cheng, B. Wang, Y. Gao, X. Li, T. Yang, T. Zhang, G. Lu, *ACS Appl. Mater. Interfaces* 6 (2014) 3888-3895.
- [31] K. Kuwahara, R. Taguchi, M. Kishino, N. Akamatsu, K. Tokumitsu, A. Shishido, *Appl. Phys. Express.* 13 (2020).
- [32] X. Yu, X. Zhang, H. Wang, G. Feng, *Appl. Surf. Sci.* 425 (2017) 803-810.
- [33] X. Wang, C. Hu, H. Liu, G. Du, X. He, Y. Xi, *Sensors Actuators, B Chem.* 144 (2010) 220-225.
- [34] X. Zhang, S. Sun, J. Lv, L. Tang, C. Kong, X. Song, Z. Yang, *J. Mater. Chem. A.* 2 (2014) 10073-10080.

Chapter 7 General Conclusions

In this thesis, Cu₂O, CuO and ZnO films were fabricated by novel solution process, named as spin-spray method and mist spin spray method. These methods are characterized by its low deposition temperature (< 100 °C), simple equipment, high deposition rate and low cost. Importantly, they do not adversely affect the substrate because of the low fabrication temperature and high deposition rate, which allows a short deposition time. Therefore, they enabled to the fabrication of Cu₂O, CuO and ZnO films on flexible polymer substrates with low thermal durability. The fabricated films were applied as flexible sensors for wearable electronics.

In *Chapter 2*, phase-pure Cu₂O films were fabricated on the seed-free glass substrates at low temperature of 70 °C with a high deposition rate of 0.3 μm/min by the spin-spray method. It was possible to control the grain size, the crystalline orientation of the films, the surface morphology, and the optical band gap by adjusting the concentrations of NH₃ and NaOH in the reaction solution. The films fabricated with a low NH₃ aq. concentration were composed of nanosized grains and highly [111] oriented. On the other hand, films fabricated with a high NH₃ aq. concentration were composed of submicron grains and highly [100] oriented.

In *Chapter 3*, the spin-spray method enabled to the fabrication phase-pure CuO nanostructures at a low temperature of 90 °C for a short time of 10 min. Grass-like array and carpet-like dense films of CuO nanosheets were fabricated on glass substrates via the method using different complexing agents. The CuO nanosheet had nanosheets having a high aspect ratio, i.e. 2 μm in the lateral direction and 20 nm in thickness. The CuO nanostructures strongly adhered to the substrate.

In *Chapter 4*, a novel solution-based process, termed the mist spin spray method, was developed to fabricate nanostructured CuO thin films on seed-free glass substrates. These mists are subsequently sprayed onto a substrate heated to 90 °C and fixed on a rotating platform to grow crystalline CuO thin films at atmospheric pressure. This one-step method enables the generation of phase-pure, dense and crack-free CuO thin films below 100 °C.

In *Chapter 5*, a transparent ZnO film was fabricated by the spin-spray method at a low temperature of 90°C. The high resistivity, 55.3 Ω cm, of the as-deposited ZnO film by the spin-spray method was drastically decreased down to 4.43×10^{-2} Ω cm after UV treatment for 60 min due to the generation of hydrogen donors in the ZnO film. The as-deposited ZnO film contained a large amount of trapped water. The trapped water was decomposed to form H⁺ and OH⁻ ions by photocatalytic activity of UV- irradiated ZnO. These ions associated with the V_O and V_{Zn} resulted the generation of thermodynamically stable hydrogen donors.

In *Chapter 6*, the spin-spray method and mist spin spray method are applied to fabricate Cu₂O, CuO and ZnO films on PET substrates for various flexible sensor applications. The performance of the fabricated flexible sensors based on these metal oxide films is as follows.

The fabricated Cu₂O film on the PET substrate was employed as a flexible bending sensor, and its bending performance was evaluated by measuring the electrical resistance between the electrodes under various curvatures. The Cu₂O bending sensor possessed excellent stability and repeatability over a wide curvature range. Moreover, the sensor demonstrated a high sensitivity and a short response time with a high resolution for very small curvature changes. The sensor possessed good repeatability as well as long-

term and mechanical fatigue durability over 30 days and 1,000 bending–release cycles, respectively. All of these excellent sensing characteristics indicate the applicability of the sensor for detailed monitoring of large- and small-scale human motions. Excellent stability and repeatability of the monitoring response over a wide range of motion angles and speeds was demonstrated.

The Cu₂O/ZnO heterojunction films were fabricated on ITO coated PET substrates by the spin-spray method for flexible photodetectors. The Cu₂O/ZnO showed rectification behavior, indicating the formation of p-type Cu₂O/n-type ZnO heterojunctions. The flexible Cu₂O/ZnO junction photodetector showed the typical photoelectric performance, and the response and recovery times below 4.7 s and 6.7 s, respectively.

The fabricated CuO nanostructured films on the PET substrate were applied as flexible humidity sensors. The CuO nanosheet array structures possessed excellent humidity-sensing performance, including high sensitivity, good repeatability and fast response/recovery characteristics, because of its high surface area and surface-to-volume ratio. The sensor based on the CuO nanosheet array showed reliability and durability against mechanical bending because the nanosheets were not aggregated but instead located sparsely on the substrate. The CuO nanosheet array therefore has potential as a sensing material for high-performance flexible humidity sensors.

The fabricated CuO thin film was fabricated on the ITO/PET substrate for a flexible glucose sensor by the mist spin spray method. This sensor showed high-transparency in the visible light region of the spectrum. The sensor shows the high linearity over a wide detection range to glucose.

In conclusion, the developed solution-based processes can fabricate functional metal oxide films at a low process temperature below 100 °C with a high deposition rate. Therefore, these solution-based processes enabled to the fabrication of functional metal oxide films on flexible polymer substrates with low thermal durability. In addition, the metal oxide films fabricated by these methods exhibited good adhesion to PET substrates, and therefore, they were sufficiently flexible to be used in bent conditions. Metal oxide film-based flexible sensors with high sensing performance and mechanical fatigue durability were fabricated by optimizing the particle size, film thickness, and film morphology through controlling the spin spray reaction. The metal oxide-based flexible sensors fabricated by these solution-based processes have broad application prospects for future wearable electronics.

Acknowledgments

It is my pleasure to acknowledge the assistance of many who have helped me to bring this study to its final form.

Words fail to express deep gratitude. I owe to *Prof. Nobuhiro Matsushita*, Tokyo Institute of Technology, Japan, for their stimulating discussion, insightful comments and suggestions, inspiring guidance and constant encouragement during the course of the present investigation.

I would like to offer my special thanks to Prof. Akira Nakajima, Prof. Masahiro Miyauchi Prof. Toshiyuki Ikoma and Prof. Tetsuji Yano for being my examiners along with Prof. Nobuhiro Matsushita.

I would also like to express gratitude to Asst. Prof. Yuta Kubota (Tokyo Institute of Technology) and Asst. Prof. Tetsuo Kishi (Tokyo Institute of Technology). Their valuable feedbacks helped me to improve my research. I would like to deeply thank to Prof. Atsushi Shishido to permit to use bending machine, and to give practical advice.

My earnest gratitude to the Yano laboratory secretary Ms. Tomoko Shizume and former Yano and Matsushita laboratory secretary Ms. Mariko Kurihara. Also, I express my heartfelt thanks to the former Matsushita laboratory secretary Ms. Junko Ito and Ms. Hiroko Yoshioka. Furthermore, I would like to appreciate to Ms. Yoshiko Ogiso and Ms. Yu Murakami. All of them helped me in official works.

I would like to heartfelt thanks to graduated and recent members of our laboratory; Mr. Hidemi Yoshikawa, Dr. Lin Hwai En, Dr. Rent Miraanti, Mr. Ricky Dwi Septianto, Ms. Kana Tomita, Mr. Masaki Hayashi, Mr. Tetsuya Furukawa, Mr. Kazuya Shimada, Mr. Riku Shinjo, Mr. Michihiko Uemura, Mr. Syun Nagai, Mr. Yusuke Fujii, Mr. Saito Kensuke, Ms. Ayaka Endo, Mr.

Junnosuke Nishimoto, Mr. Lo Tuan Son, Mr. Shungo Aoki, Mr. Yutaka Fujita, Mr. Keita Wasaki and Mr. Kazuhiro Usui.

My sincere thanks to all my friends, near and dear ones in Tokyo Institute of Technology for their kind help throughout my stay in Ookayama campus and Suzukake-dai campus.

My sincere acknowledgements to my father Koh-Hei Nitta, mother Yuka Nitta, younger brother Hiroyuki Nitta, and all other family member for their help.

Finally, I wish to appreciate all invisible support given by persons around me.

***- Ryosuke Nitta
Tokyo Institute of Technology, Japan***

List of Publications and Presentations

Publications

- 1 **R. Nitta**, Y. Kubota, T. Kishi, T. Yano, N. Matsushita, One-step direct fabrication of phase-pure Cu₂O films via the spin-spray technique using a mixed alkaline solution, *Mater. Chem. Phys.* 243 (2020) 122442.
- 2 **R. Nitta**, H. Lin, Y. Kubota, T. Kishi, T. Yano, N. Matsushita, CuO nanostructure-based flexible humidity sensors fabricated on PET substrates by spin-spray method, *Appl. Surf. Sci.* 572 (2022) 151352.
- 3 **R Nitta**, R Taguchi, Y Kubota, T Kishi, A Shishido, N Matsushita, “Novel Bending Sensor Based on Solution-Processed Cu₂O Film with High Resolution Covering a Wide Curvature Range”, *ACS Omega*, Accepted in October 2021
- 4 H. Lin, J. Hong, **R. Nitta**, Y. Kubota, Y. Katayanagi, Effects of UV irradiation on the electrical and optical properties of solution- processed transparent ZnO films, *Appl. Surf. Sci.* 489 (2019) 135–141.

Presentations Related to the Thesis at International Conference

1. (Oral) **NITTA Ryosuke**, KUBOTA Yuta, MATSUSHITA Nobuhiro. Nanosheets accumulated CuO films fabricated by one-step solution process at high speed, PACRIM13, Oct. 2019.
2. (Poster) **Ryosuke Nitta**, Yuta Kubota, Nobuhiro Matsushita. Novel Bending Sensor Based on Solution-Processed Cu₂O Film for Healthcare Monitoring Application, STAC12, July 2021.
3. (Poster) **Ryosuke Nitta**, Hwai En Lin, Tetsuo Kishi, Tetsuji Yano, Yuta Kubota, Nobuhiro Matsushita. A High Transparency and Excellent Conductivity of Spin-sprayed ZnO Films Fabricated at 90°C, 1st Tokyo Tech-NCTU Joint Symposium on Advanced Materials, Sept. 2019.
4. (Poster) Yutaka Fujita, **Ryosuke Nitta**, Yuta Kubota, Nobuhiro Matsushita. Flexible Glucose Sensor Based on CuO Film Fabricated by Spin Mist Spray method, STAC12, July 2021.

Presentations Related to the Thesis at Domestic Conference

1. (口頭) 新田 亮介, 久保田 雄太, 松下 伸広. フレキシブル湿度センサ応用へ向けたPET基板状へのCuOナノ構造体の作製, 第30回日本MRS年次大会, Dec. 2020.
2. (口頭) 遠藤 綾華, 新田 亮介, 久保田 雄太, 松下 伸広. 低環境負荷溶液プロセスによるレアアースフリー透明導電性ZnO膜の作製, 第10回JACI/GSCシンポジウム, June 2021.
3. (口頭) 遠藤 綾華, 新田 亮介, 久保田 雄太, 松下 伸広. 紫外線照射が溶液作製ZnO膜の導電性を向上させるメカニズムの解明, 日本セラミックス協会2021年年会, Mar. 2021.
4. (口頭) 遠藤 綾華, 新田 亮介, 久保田 雄太, 松下 伸広. 溶液作製ZnO膜への紫外線照射による導電性向上のメカニズム解明, 第30回日本MRS年次大会, Dec. 2020.
5. (口頭) 松下伸広, 新田亮介, 久保田雄太. 酸化銅ナノ構造の溶液作製とセンサ応用, 粉体粉末冶金協会2020年度秋季大会(第126回講演大会), Oct. 2020.
6. (口頭) 新田亮介, 久保田雄太, 松下伸広. スピンスプレー法によるスーパーキャパシタ電極用CuOナノシートアレイの直接堆積, 日本セラミックス協会第35回関東支部研究発表会, Sept. 2019.
7. (口頭) 新田 亮介, 岸 哲生, 矢野 哲司, 松下 伸広. 溶液法による高結晶性亜酸化銅膜の高速堆積, 日本セラミックス協会2019年年会, 日本セラミックス協会2019年年会講演予稿集, 2D02, Mar. 2019.
8. (口頭) 新田亮介, Lin Hwai-En, 久保田雄太, 岸哲生, 矢野哲司, 松下伸広. スピンスプレー法による高結晶性Cu₂O膜の高速堆積, 日本セラミックス協会第34回関東支部研究発表会, 1C09, Sept. 2018.
9. (ポスター) 新田亮介, 久保田雄太, 松下伸広. 溶液作製ZnO透明膜への紫外線照射による導電性発現のメカニズム解明, 第18回無機材料合同研究会, 山梨大学 (2019年9月)
10. (ポスター) 新田亮介, 岸哲生, 矢野哲司 松下伸広. スピンスプレー法による高結晶性Cu₂O膜の高速堆積, 第17回無機材料合同研究会, 東京工業大学 (2018年9月)(優秀賞)
11. (ポスター) 新田亮介, 岸哲生, 矢野哲司 松下伸広. 溶液作製ZnO透明膜への紫外線照射によるメカニズム解明, 第16回無機材料合同研究会, 東京理科大学 (2017年9月)